ON FRESNELETS, INTERFERENCE FRINGES, AND DIGITAL HOLOGRAPHY

THÈSE N^O 2977 (2004)

PRÉSENTÉE À LA FACULTÉ SCIENCES ET TECHNIQUES DE L'INGÉNIEUR

Institut d'imagerie et optique appliquée

SECTION DE MICROTECHNIQUE

ÉCOLE POLYTECHNIQUE FÉDÉRALE DE LAUSANNE

POUR L'OBTENTION DU GRADE DE DOCTEUR ÈS SCIENCES

PAR

Michael LIEBLING

ingénieur physicien diplômé EPF
de nationalité suisse et originaire de Greifensee (ZH)

acceptée sur proposition du jury:

Prof. M. Unser, directeur de thèse
Prof. R. Dändliker, rapporteur
Dr C. Depeursinge, rapporteur
Prof. T. Fournel, rapporteur
Prof. M. Vetterli, rapporteur

Lausanne, EPFL
2004

Thèse présentée à la Faculté des Sciences et Techniques de l'Ingénieur, Section de Microtechnique, École Polytechnique Fédérale de Lausanne, pour l'obtention du grade de Docteur ès Sciences.

Composition du jury
Prof. René-Paul Salathé, *président*
Prof. Michael Unser, *directeur de thèse*
Prof. René Dändliker, *rapporteur*
Dr Christian Depeursinge, *rapporteur*
Prof. Thierry Fournel, *rapporteur*
Prof. Martin Vetterli, *rapporteur*

Adresse du candidat
Michael Liebling
EPFL-LIB, Bât. BM 4.141
CH-1015 Lausanne
`michael.liebling@a3.epfl.ch`
`http://bigwww.epfl.ch/liebling/`

Lausanne, le 21 avril 2004

Abstract

In this thesis, we describe new approaches and methods for reconstructing complex-valued wave fields from digital holograms. We focus on Fresnel holograms recorded in an off-axis geometry, for which operational real-time acquisition setups readily exist.

The three main research directions presented are the following. First, we derive the necessary tools to port methods and concepts of wavelet-based approaches to the field of digital holography. This is motivated by the flexibility, the robustness, and the unifying view that such multiresolution procedures have brought to many applications in image processing. In particular, we put emphasis on space-frequency processing and sparse signal representations. Second, we propose to decouple the demodulation from the propagation problem, which are both inherent to digital Fresnel holography. To this end, we derive a method for retrieving the amplitude and phase of the object wave through a local analysis of the hologram's interference fringes. Third, since digital holography reconstruction algorithms involve a number of parametric models, we propose automatic adjustment methods of the corresponding parameters.

We start by investigating the Fresnel transform, which plays a central role in both the modeling of the acquisition procedure and the reconstruction of complex wave fields. The study of the properties that are central to wavelet and multiresolution analysis leads us to derive Fresnelets, a new family of waveletlike bases. Fresnelets permit the analysis of holograms with a good localization in space and frequency, in a way similar to wavelets for images. Since the relevant information in a Fresnel off-axis hologram may be separated both in space and frequency, we propose an approach for selectively retrieving the information in the Fresnelet domain. We show that in certain situations, this approach is superior to others that exclusively rely on the separation in space or frequency.

We then derive a least-squares method for the estimation of the object wave's amplitude and phase. The approach, which is reminiscent of phase-shifting techniques, is sufficiently general to be applied in a wide variety of situations, including those dictated by the use of microscopy objectives.

Since it is difficult to determine the reconstruction distance manually, we propose an automatic procedure. We take advantage of our separate treatment of the phase retrieval and propagation problems to come up with an algorithm that maximizes a sharpness metric related to the sparsity of the signal's expansion in distance-dependent Fresnelet bases.

Based on a simulation study, we suggest a number of guidelines for deciding which algorithm to apply to a given problem. We com-

pare existing and the newly proposed solutions in a wide variety of situations. Our final conclusion is that the proposed methods result in flexible algorithms that are competitive with preexisting ones and superior to them in many cases. Overall, they may be applied in a wide range of experimental situations at a low computational cost.

Version Abrégée

Fresnelettes, franges d'interférences et holographie digitale

Dans cette thèse, nous proposons de nouvelles approches et méthodes pour la reconstruction de champs d'ondes à valeurs complexes à partir d'hologrammes digitaux. Nous nous concentrons sur des hologrammes de type Fresnel, enregistrés dans une géométrie hors axe, pour laquelle des systèmes d'acquisition en temps réel existent actuellement.

La recherche présentée est articulée selon trois axes principaux. Premièrement, nous dérivons les outils nécessaires pour transférer des méthodes et concepts de l'approche multirésolution au domaine de l'holographie digitale. Cette démarche est motivée par la flexibilité, la robustesse et la vision unificatrice que les ondelettes ont apportées à de nombreuses applications en traitement d'images. Nous nous intéressons en particulier au traitement espace-fréquence et aux représentations concises de signaux. Deuxièmement, nous proposons de découpler les deux problèmes inhérents à l'holographie digitale de Fresnel, à savoir ceux liés à la démodulation et à la propagation. À cette fin, nous dérivons une méthode d'estimation de l'amplitude et de la phase de l'onde objet à l'aide d'une analyse locale des franges d'interférence de l'hologramme. Troisièmement, les algorithmes de reconstruction en holographie digitale étant basés sur plusieurs modèles paramétriques, nous proposons des méthodes automatiques d'ajustement des paramètres impliqués.

Nous commençons par étudier la transformée de Fresnel qui joue un rôle majeur tant dans la modélisation de la procédure d'acquisition que dans la reconstruction de champs d'ondes à valeurs complexes. L'étude des propriétés centrales à la théorie des ondelettes et de l'analyse multirésolution nous conduit à dériver les Fresnelettes, une nouvelle famille de bases de type ondelette. Les Fresnelettes permettent l'analyse des hologrammes avec une bonne localisation dans l'espace et les fréquences, comme les ondelettes pour le traitement d'images. Comme l'information encodée dans un hologramme hors axe de type Fresnel peut être séparée à la fois dans l'espace et les fréquences, nous proposons une approche pour la récupérer de manière sélective dans le domaine des Fresnelettes. Comparée à d'autres méthodes basées exclusivement sur la séparation dans l'espace ou dans le domaine des fréquences, cette approche conduit à une qualité de reconstruction supérieure dans de nombreuses situations.

Nous dérivons ensuite une méthode d'estimation par moindres carrés de l'amplitude et de la phase de l'onde objet. Cette approche, qui rappelle certaines techniques de décalage de phase, est suffisamment générale pour être appliquée dans une grande variété d'arrange-

ments expérimentaux, y compris ceux avec un objectif de microscope.

Comme il est difficile de déterminer la distance de reconstruction manuellement, nous proposons une procédure automatique. Notre traitement séparé des problèmes d'estimation de phase et de propagation nous permet de proposer un algorithme qui maximise une métrique de netteté apparentée à la capacité de représenter le signal de manière concise dans des bases de Fresnelettes dépendantes de la distance.

Enfin, nous donnons des directives pour guider le choix de l'algorithme en fonction d'un problème donné. À cet effet, nous effectuons une étude de simulation et comparons des méthodes existantes à celles nouvellement proposées dans une large palette de situations. Nous concluons que ces dernières résultent en des algorithmes à la fois flexibles et dont la qualité de reconstruction est compétitive voire en de nombreux cas supérieure à celle d'autres approches. De manière générale, ils peuvent être appliqués dans une gamme élargie de situations expérimentales tout en limitant les coûts de calcul.

Zusammenfassung

Über Fresnelets, Interferenzmuster und digitale Holographie

Vorliegende Dissertation befasst sich mit neuen Konzepten und Methoden für die Rekonstruktion komplexer Wellenfelder, ausgehend von digitalen Hologrammen. Wir beschränken uns auf Fresnelhologramme, die in einer *off-axis* Anordnung aufgenommen wurden und wofür Echtzeit Datenerfassungssysteme bereits bestehen.

Die hier vorgestellte Forschungsarbeit hat drei Hauptschwerpunkte. Erstens leiten wir die notwendigen Hilfsmittel her, um Methoden und Konzepte der Multiresolutionsanalyse auf das Gebiet der digitalen Holographie zu übertragen. Dieses Vorgehen wird durch die Flexibilität, Robustheit, sowie die vereinheitlichende Darstellungsweise motiviert, welche den Wavelets bereits zu zahlreichen Anwendungen in der Bildverarbeitung verholfen haben. Insbesondere interessieren wir uns für die Verarbeitung im Raum- und Frequenzbereich und für sparsame Signaldarstellungen. Zweitens schlagen wir vor, die beiden Probleme der digitalen Fresnel Holographie, nämlich das Demodulationsproblem und das Propagationsproblem, zu entkoppeln. Zu diesem Zweck leiten wir eine Methode zur Näherung der Amplitude und der Phase der Objektwelle mittels einer lokalen Analyse der Interferenzstreifen des Hologramms her. Drittens konzentrieren wir uns auf automatische Justierungsmethoden der auftretenden Parameter, zumal Holographie Rekonstruktionsalgorithmen auf mehreren parametrischen Modellen basieren.

Wir beginnen mit der Betrachtung der Fresnel Transformation, die sowohl beim Modellieren des Akquisitionsverfahrens, als auch bei der Rekonstruktion komplexer Wellenfelder eine zentrale Rolle spielt. Die Untersuchung der Eigenschaften, die für die Wavelet- und Multiresolutionsanalyse von Bedeutung sind, führt uns auf die Herleitung einer neuen Familie von Wavelet-artigen Basen: der Fresnelets. In ähnlichem Masse wie Wavelets für Bilder, ermöglichen Fresnelets die Analyse von Hologrammen mit guter Lokalisierung in Raum- und Frequenzbereich. Da die relevanten Informationen in einem Fresnel *off-axis* Hologramm sowohl im Raum-, wie auch im Frequenzbereich getrennt werden können, schlagen wir eine Methode vor, um die Information im Fresnelet Bereich selektiv wiederzugewinnen. In zahlreichen Situationen weisen wir die Überlegenheit dieses Verfahrens gegenüber anderen nach, die ausschliesslich auf der Trennung im Raum- oder Frequenzbereich beruhen.

Wir entwickeln danach eine Methode zur Schätzung der Amplitude und der Phase der Objektwelle im Sinne der kleinsten Quadrate. Das Konzept, das an gewisse Phasenverschiebungstechniken gemahnt, ist hinreichend allgemein, um in einer grossen Vielfalt von Situationen anwendbar zu sein, einschliesslich solcher, welche die An-

wesenheit von Mikroskop Objektiven umfassen.

Da es schwierig ist die Rekonstruktionsdistanz manuell zu ermitteln, schlagen wir hierfür ein automatisches Verfahren vor. Dabei gereicht es uns zum Vorteil, dass wir die Probleme der Phasen Rekonstruktion und der Propagation separat behandeln. Dies is nämlich Voraussetzung eines neuen Algorithmus zur Maximierung einer Schärfemetrik, die verbunden ist mit der Eigenschaft der distanzabhängigen Fresnelet Basen, ein Signal mit möglichst wenig Koeffizienten darzustellen.

Schliesslich schlagen wir Richtlinien vor, zur Auswahl angemessener Algorithmen für jeweils gegebene Probleme. Dazu vergleichen wir in einer Simulationsstudie, das Verhalten von herkömmlichen und den neu vorgeschlagenen Methoden in einer Vielfalt von Situationen. Wir halten fest, dass die vorgeschlagenen Methoden zu flexiblen und rechensparsamen Algorithmen führen. Sie können in einer breiten Palette von experimentellen Situationen angewandt werden und erweisen sich in vielen Fällen den herkömmlichen überlegen.

Contents

0000001010

List of Figures

List of Tables

List of Notations

Roman Letters

a	Real number, amplitude of complex number
A	Lower Riesz bound constant
$A(\mathbf{x})$	Reference wave amplitude
b	Real number, Amplitude of complex number
B	Upper Riesz bound constant
$c_\mathbf{k}$	Expansion coefficient
$c_{\mathbf{p_k}}$	Parent of expansion coefficient
$C(x), S(x)$	Fresnel integrals
$\mathbb{C}$	Complex numbers
d	Reconstruction distance
d_k	Wavelet coefficient
d_O	Object-lens distance
d_I	Lens-image distance
D, D_x, D_y	Curvature of quadratic complex mask
e	2.71828...
$f(x), g(x)$	(Complex-valued) functions of one variable
$f(\mathbf{x}), g(\mathbf{x})$	(Complex-valued) functions of two variables
f	Focal length
$g(k)$	Discrete filter
$h(k)$	Discrete filter
$\Im$	Imaginary part
i	$\sqrt{-1}$
$I(\mathbf{x})$	Hologram
j	Scale parameter
J	Maximal scale parameter
k	Integer shift
$\mathbf{k}$	Wavelet coefficient index
$k_\tau(x)$	Fresnel transform kernel (1D)
$K_\tau(\mathbf{x})$	Fresnel transform kernel (2D)
$\mathbf{k}_\lambda = (k_x, k_y, k_z)$	Wave vector
$k_\lambda = 2\pi/\lambda = \|\mathbf{k}_\lambda\|$	Wavenumber
$\mathbf{K} = (K_x, K_y)$	Fringe vector
$K(x, y)$	Fringe vector norm
l	General discrete index
L_2	Hilbert space of finite energy functions (continuous)
ℓ_2	Hilbert space of finite energy sequences (discrete)

0000001111

L_p	Banach space (continuous)
ℓ_p	Banach space (discrete)
L	Total number of pixels ($N_x \times N_y$)
L_x, L_y	CCD dimensions
L_W	Side width of sliding window
$\underline{L}_W$	Minimal side width of sliding window
$\overline{L}_W$	Maximal side width of sliding window
L_{tube}	Normalized microscope tube length
m	Scale factor
$\mathbf{m}$	Integer shift (2D)
M	Number of samples in window
$\tilde{M}$	Average number of samples in window
$\mathcal{M}$	Magnification
n	Degree or general discrete index
N	Integer, number of retrieved phase points
N_x, N_y	Image dimension, number of pixels
N_F	Fresnel number
$\mathcal{O}$	Order (complexity)
$O(\mathbf{x})$	Object wave
$\mathbf{p_k}$	Parent index of wavelet coefficient index $\mathbf{k}$
$\mathcal{R}_{(d)}$	Free-space propagation operator
$R(\mathbf{x})$	Reference wave
$\mathbb{R}$	Real numbers
$\Re$	Real part
$S, \tilde{S}$	Families of functions
t	Temporal variable
t_j	Threshold at scale j
T, T', T_x, T_y	Sampling steps
$U(x, y)$	Complex wave
$U_d(x, y)$	Complex wave at distance d
U	Auxiliary real variable, hologram's zero-order term
$\mathcal{U}$	Unitary operator
$\tilde{u}_l, \tilde{v}_l$	Transformed vectors
u_l, v_l	Element of a Riesz basis and its dual.
$u_{n,\tau}(x)$	Fresnelet building block
$V_j, \tilde{V}_{j,\tau}$	Subspaces of L_2
V_m	Normalized reference wave
w_m	Weights
$W_j, \tilde{W}_{j,\tau}$	Complement subspaces of L_2
$\mathbf{x} = (x, y)$	2D vector
x	Continuous spatial variable
y	Continuous spatial variable
z	Propagation direction
Z	Complex number
$\mathbb{Z}$	Integer numbers

Greek Letters

α	Complex variable
β	Complex variable
$\beta^n(x)$	Basic Spline (B-Spline) of degree n
$\tilde{\beta}^n(x)$	Fresnelet Spline (F-Spline) of degree n
γ	Camera gamma factor
$\delta(x)$	Dirac delta
Δ^n	nth iteration of the finite difference operator
η	Real variable
$\theta, \theta_{\max}$	(Maximal) Angle between the reference and object waves
$\theta(\mathbf{x})$	Phase of the reference wave
λ	Wavelength
$\Lambda = 2\pi / \|\mathbf{K}\|$	Fringe spacing
μ_f	Mean of function f
ν	Frequency variable ($\nu = \omega/(2\pi)$)
ξ	Real variable
π	3.14159…
ρ	Chirp parameter, curvature
σ_f^2	Variance of function $f(x)$
τ	Fresnel transform parameter
ϕ	Phase of complex number
$\phi(t)$	Mother Wavelet, scaling function
$\psi(t)$	Father Wavelet, wavelet
$\psi(\mathbf{x})$	Complex object wave in object vicinity
$\Psi(\mathbf{x})$	Complex object wave in CCD plane
ω_0	Gaussian parameter
Ω	Domain, $\mathbb{R}$ or $\mathbb{R}^2$

Other notations

FFT	Fast Fourier Transform
IFFT	Inverse Fast Fourier Transform
PSNR	Peak Signal to Noise Ratio
$\text{rect}(x)$	Rectangle function
$\text{sinc}(x) = \frac{\sin(\pi x)}{\pi x}$	Sinc function
SNR	Signal to Noise Ratio
USAF 1951	United States Air Force 1951 resolution target
Z^*	Complex conjugate
$*$	Convolution
$(x)_+^n$	One-sided power function.
$\tilde{f}_\tau, \tilde{g}_\tau$	Fresnel transforms with parameter τ
$\hat{f}(\nu), \hat{g}(\nu)$	Fourier Transform
$\overline{V}$	Closure of V

Chapter 1

Introduction

1.1   Digital Off-Axis Holography

Whenever an object is illuminated with a coherent light source, the transmitted or reflected wave carries information on the sample's optical and physical properties. In the close vicinity of the object, the light intensity is related to its reflectance or attenuation while the phase is related to its topography or thickness. Light sensors, such as photographic film or digital cameras, may be used to measure the intensity of the incoming light, but they fail to capture its phase. This crucial information is therefore lost. From a mathematical point of view, this type of measurement is equivalent to evaluating the squared modulus of a complex number, an operation which clearly discards the phase.

When Gabor proposed "a new two-step method of optical imagery" [63] more than fifty years ago, his aim was to improve the resolution of electronic microscopes, which suffer from limiting aberrations, notably because of the lack of concave electron lenses [205, p. 133]. In the sequel, holography has become a major pillar of modern optics and imaging. The two steps that form the essence of holography are:

- The recording of information about a wave field, the object wave, in a form and on a medium suitable for later reconstruction.

- The reconstruction or retrieval of the original object wave from the information stored during the first step, and some a priori knowledge on the recording conditions.

The wave field's phase, polarization, coherence, etc., are characteristics that may typically be stored in a hologram. The fact that these quantities cannot be measured directly with conventional detectors, which are only sensitive to the wave field's intensity, makes holographic techniques particularly attractive. The acquisition process consists in recording (for example on a photographic plate) the interference between the object wave and a reference wave. This requires the two
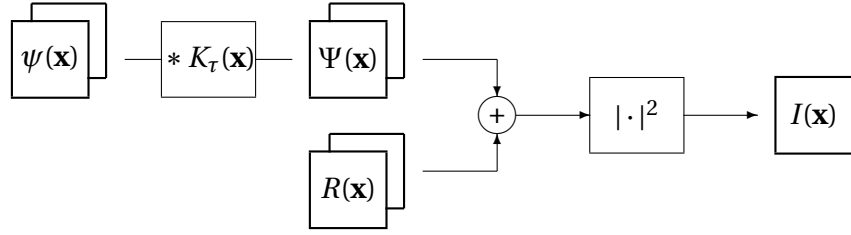
Fig. 1.1. Digital holography in a nutshell. We are interested in retrieving the complex-valued wave front $\psi(\mathbf{x})$ in the vicinity of the object from the real-valued measurements of the intensity $I(\mathbf{x}) = |\Psi(\mathbf{x}) + R(\mathbf{x})|^2$ (the hologram), where $\Psi(\mathbf{x})$ is the propagated object wave (propagation is modeled by the Fresnel transform), and $R(\mathbf{x}) = A(\mathbf{x}) \exp[i(k_x x + k_y y)]$ the reference wave, both evaluated in the CCD plane.

waves to be coherent.[1] The reconstruction may be achieved optically, by illuminating the (chemically processed) hologram with a replica of the reference wave.[2]

This thesis investigates several aspects of one particular instance of holography, namely digital holography. The interference pattern—the hologram—is recorded by a digital camera (CCD) and the retrieval of the object wave is done numerically. We focus on new approaches and methods to perform the second, reconstruction step.

As a prerequisite, we need a model that faithfully describes the acquisition process. Leith and Upatnieks [123] showed that "[the] construction of the hologram constitutes a sequence of three well-known operations: a modulation, a frequency dispersion, and a square-law detection" (see Fig. 1.1). In light of this analysis, they have proposed an acquisition procedure, which allows for an unperturbed reconstruction by illuminating the hologram with the reference wave: In the so-called off-axis geometry, the object and reference wave travel in different directions. The object wave is thus separated from the reference wave. In image processing terms, this geometry implies the presence of interference fringes in the recorded hologram or, equivalently in signal processing terms, the presence of a carrier frequency or modulation. We will consider off-axis geometries throughout this thesis. One arrangement that is often used is to record the distribution of intensity in the hologram plane at the output of a Michelson interferometer where one of the mirrors is slightly tilted (for a sneak preview, see Fig. 2.6, p. 47). The digital reconstruction of the complex wave (amplitude and phase) near the object is based on the Fresnel transform, an approximation of the diffraction integral [72].

---

[1]The lack of powerful coherent sources until the availability of the first lasers [138] explains why holographic techniques have only truly taken off in the Sixties.

[2]The reconstructing wave need not be the same as the reference (it need not even necessarily be of high coherence). However, there needs to be a special acquisition setup for recording holograms that are to be reconstructed with white light [10].

1.2   Motivations and Contributions

Digital holography brings along many advantages. There is no chemical film processing. Acquisition can be performed in real-time, including during the alignment and adjustment procedure of the optical elements. Digital reconstructions offer quantitative access to the physical quantities of interest. The processing possibilities (aberration compensation, etc.) are almost limitless.

Although the Greek etymology of the word hologram seems to presuppose a system capable of recording the entire (*holos*) message (*gramma*) carried by the wave, the amount of information that may actually be accessed is limited. Compared to photographic film which may be used for recording very fine fringes (∼ 5000 lines/mm), currently available CCDs offer poor performances (∼ 500 lines/mm for a CCD with pixel size ∼ 10 μm). The recording medium is of lower dimensionality than the information to be stored on it: it corresponds to a 2D array of positive real numbers, whereas the wave field is complex valued, 3D, and possibly vectorial if polarization is taken into account. A large sampling step therefore implies that it is only partially possible to compensate for this mismatch. Additional digital holography constraints are:

- Digital cameras offer limited resolution (discussed above).
- The support size of currently available cameras is small.
- A computer is used for reconstruction and storage; speed and storage capacity therefore play an important role.
- All optical elements and phenomena (including propagation, the presence of lenses or imperfect optics) need to be modeled accurately; this is not required when the reconstruction is done optically, since an aberration may be compensated by an optical element.
- Noise may corrupt the result and the algorithms may become unstable.

These constraints, which are specific to digital holography, are common to many image processing problems. The design of effective reconstruction algorithms should therefore take advantage of recent developments in this field; the methods we present in the subsequent chapters aim at pushing back the above constraints.

Wavelets and, more generally, multiresolution approaches have contributed recently to dramatic advances in several areas of image processing. These range from image compression standards[3] to ro-

---

[3]The recently adopted JPEG 2000 image compression standard [90] recommends to code wavelet coefficients rather than discrete cosine transform coefficients, as in the old standard.

bust, elegant, and flexible multiresolution algorithms that lead to inverse problem solutions for applications such as computerized tomography [12, 19, 85], image registration [203], denoising [45, 221], etc. This has motivated our efforts to adapt some of these techniques to digital holography. In order to derive the necessary tools for achieving this, we need to analyze one of the two ingredients of digital Fresnel holography: the Fresnel transform.

Most digital hologram reconstruction algorithms mimic the physical reconstruction procedure and suffer from a number of artifacts that need to be treated separately. Our approach follows the flow graph of the acquisition model (see Fig. 1.1), but in reverse order. First, we solve the square-law detection and demodulation problem and, in a second step, the propagation problem. This decoupling is made possible thanks to a new algorithm that can retrieve the amplitude and phase in several non-standard situations (e.g. including the presence of a microscope objective). Since the procedure relies on a parametric acquisition model, we can term it parametric fringe analysis.

A convenient by-product of the decoupling approach is that it provides us with a procedure for the simulation of the forward model, which allows us to try out a wide range of experimental situations and compare reconstruction algorithms on a quantitative basis.

Digital holography reconstruction algorithms rely on parametric models. Once the model is set, the parameters involved need to be tuned, which might be tedious if done manually. We therefore concentrate on methods for their automatic adjustment.

1.3 Related Work

To give a general picture of available digital holography reconstruction methods, we review the main developments carried out since their conception. Because wavelets play a central role in our formulation, we also give an overview of wavelet applications and theory in optics, especially in the restricted context of propagation, demodulation, and fringe analysis. We refer to further literature in later chapters whenever appropriate.

1.3.1 Reconstructing Digital Holograms: an Overview

The reconstruction of holograms by computer goes back to the late Sixties, some twenty years after the publication of Gabor's landmark papers [62–64]. Methods were first proposed by Goodman and Lawrence [73], Kronrod *et al.* [109] and Yaroslavsky and Merzlyakov [225].

Important steps in the evolution of the technique and algorithms

have been: the use of a CCD camera to acquire the hologram [185], acquisition through endoscopic devices [34], the reconstruction of the phase in addition to the amplitude [36, 37, 39], the measurement of polarization states [32], and stress analysis [170]. The use of digital holography at high wavelength has been demonstrated recently [2]. Other developments include phase imaging without 2π ambiguity by multi-wavelength digital holography [68]. Several aberration compensation techniques [37, 41, 52, 53, 89, 122, 168, 198] have been described. Digital holography has also been used extensively for determining particle location in 3D [152, 156, 163, 167].

A recent evolution of digital holography is its application to microscopy, which allows for truly noninvasive examination of biological samples. The power of digital holography techniques for biomedical applications has been recognized early on [11, 22, 121]. Tomographic reconstruction using a wavelength scanning technique have also been reported [100].

Highly promising results have been obtained by Cuche, Marquet and co-workers who were able to monitor changes in the morphology of living organisms in real time using digital holographic microscopy [31, 37]. The technique has been further refined to allow the vision in turbid media by use of low coherence sources [143]. Its performances are close to confocal and electron microscopy but it has numerous advantages:

- It is noninvasive (low intensity, safe radiation).
- It allows for 3D measurements.
- It offers high resolution (subwavelength in the axial direction).
- Since no scanning is involved, it is faster than most other microscopy techniques and may operate in real time.
- No vacuum is required.
- It works in the presence of ambient light.

From the algorithmic point of view, much effort has been put into algorithms that aim at removing the zero and minus 1 order terms from the reconstructions [38, 106, 133] or at avoiding their presence [43]. These terms still remain a determining factor that limits the quality of the reconstructions. Sampling is a central issue in digital algorithms, and it has been studied extensively [3, 4, 49, 93, 107, 108, 116, 118, 161]. Methods that solve specific problems include a Gerchberg-Saxton-like iterative algorithm to improve the reconstructions [77] or specific implementations of the Fresnel transform [226, 227]. Finally, a general methodology for reconstructing digital holograms that inherently takes into account the statistical nature of the measured data [197] has also been proposed recently.

It is interesting to note that parallel developments have been carried through within several research communities, which consider different radiations. Although the algorithms are often similar, the literature is distinct. For instance, X-Ray holography requires algorithms that perform mainly in in-line geometries [28, 102] because of the lack and expense of efficient mirrors and are sometimes reminiscent of crystallographic techniques [145]. Aside from X-rays, algorithms have been developed for acoustical holography [84, 228, 230], but the techniques most similar to optical digital holography can be found in electron microscopy [205]. Techniques have been developed for both in-line [131] and off-axis holography [120, 151]. Commercial software packages are available for the latter [217, 218]. Beside the more conventional Fourier techniques [214], there are approaches based on neural networks [149], genetic algorithms [119] or linear programming [80]. The ability of (digital) holography to correct for aberration has also been exploited [119, 134]. Investigations to determine the optimal sampling conditions [91, 92, 99], including simulations [154], have been carried out as well.

As the range of applications gets broader, demands toward better image quality increases. Suppression of noise, higher resolution of the reconstructed images, precise parameter adjustment and faster, more robust algorithms are the essential issues.

1.3.2 Wavelet Applications and Theory in Optics

The use of wavelets in the field of optics dates back to the early years of wavelet theory. We do not cover all applications of wavelets in optics[4] but concentrate on those relevant to digital holography, propagation, fringe analysis, and demodulation.

In optics, wavelets usually appear either under the form of optical implementations of the wavelet transform, or in connection to propagation theory or image processing. Optical implementation of the (continuous) wavelet transform have been proposed at an early stage of wavelet development [59, 191]. Lebrun *et al.* [117] proposed a hologram reconstruction technique based on an optical implementation of the continuous wavelet transform. Hologram reconstruction by use of a digital CWT implementation had been proposed previously by Onural and Kocatepe [162]. An interesting result that comes out of their analysis is that the 3D structure can be completely recovered if one gets access to measurements in several successive planes. Onural and Özgen used a related transform, the Wigner transform, for similar purposes [163]. The wavelet transform was also applied to hologram analysis, again for determining the 3D location of particles [24].

---

[4]A more detailed picture of the development until 1996 is available in the review article by Li *et al.* [125].

0000011000
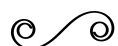
Theoretical developments have been reported mainly in the domain of wave propagation. Kaiser [97] proposed solutions to the Maxwell equations in terms of a superposition of spherical wavelets instead of the more conventional plane waves. Onural [160], Onural and Kocatepe [162] proposed a formulation of the Fresnel diffraction formula that makes it isomorphic to the continuous wavelet transform, provided the commonly-used admissibility condition is appropriately extended. Sheng *et al.* [190] showed that the wavelets proposed by Kaiser reduce to *Huygens wavelets*, thus making a formal link between the Huygens principle and the continuous wavelet theory some 300 years after Huygens' *Traité de la lumière* appeared.[5] Under the Fresnel approximation, these wavelets then become those proposed by Onural [160], and Onural and Kocatepe [162]. Battle [9] designed spherically harmonic Huygen[s] wavelets that form an or-

---

[5]A common misbelief is that the term 'wavelet' was introduced by Huygens in 1678. This is probably due to the fact that the term 'Huygens wavelet' is widely used in most optics books (including the classical text by Born and Wolf [20], who use the term 'wavelet' since their first edition in 1959 to describe the Huygens principle). It is unlikely, however, that Huygens introduced this term, since it is absent from the original manuscript, which he wrote in French. There, he uses the term *ondes élémentaires* [87, p. 18] (elementary waves). Fresnel, who completed Huygens' principle by combining it with that of interferences, was neither using the word wavelet (nor *ondelette*). Probably because his reasoning (like Huygens') was based on vibrating ether particles, he used the term *vibrations élémentaires* [58, p.209] (elementary vibrations). In 1869, É. Verdet, who published and commented Fresnel's work [58] calls the principle "*principe des ondes enveloppes* [215]" and uses the term *ondes élémentaires* (elementary waves) rather than *ondelettes* which seems not to have been used at that time. Rayleigh [200] (1887) speaks of 'secondary waves'. Poincaré [172, p. 79] (1889) uses the term *ondes élémentaires*. Kirchhoff [101, p. 22] (1891), who put the diffraction theory on a sound basis and proposed a reasoning mainly based on differential equations, banishes the idea of elementary waves altogether. At the beginning of the Twentieth Century, textbooks in French were not using the term *ondelette* neither: Wallon [219, p. 6] speaks of *centres d'ébranlement secondaires*. The term wavelet is present in Ch. F. Meyer's book [148, p. 266] (1934) as well as in L. De Broglie's [40, p.180]. The latter speaks of *ondelettes cohérentes* (coherent wavelets) that emanate from secondary sources located on the wave front's surface. But the use of the term wavelet seems not to be universal yet. Sommerfeld, who authored a mathematical theory on diffraction in 1896 [194], introduces the Huygens principle in these terms (1967) [195, p 195], '[...] Each point of this surface emits a *spherical wave* and by constructing the *envelope* of all these spherical waves [...]' (1967). Sabra [182, p. 212] speaks of "Huygens' waves", and the 'concept of secondary waves'. It seems therefore that the term wavelet must have been associated to Huygens sometime in the beginning of the Twentieth Century.

The Oxford English Dictionary [164] points to a poem by Shelley [189] as one of the first instances of the word wavelet (about 1813). The diminutive -let is a construction borrowed from French [164]. The French word *ondelette* probably originates, in turn, from the Latin diminutive *undula* [65], that Roman philosopher Boethius (c.480-c.525 CE) used in his *De musica* [16, p. 200] to describe the propagation of sound. It translates to German with *Wellchen* [17, p. 18], while the English translation [15, p. 21] calls it a *weaker impulse*. This is the oldest occurrence of a wavelet we could trace back.

0000011001

thonormal wavelet basis. The latter wavelets are generated *dynamically*, that is, rather than using translates of a single prototype function, he uses the classical wave equation in three dimensions to generate the family. Potvliege [173] proposed waveletlike basis functions, based on polar basis functions.

The developments of wavelet theory linked to propagation are also intertwined with that of the fractional-order Fourier transform [144, 157, 165]. There is a tight relation between Fresnel diffraction and the fractional-order Fourier transform [169]: while the former is evaluated on a plane, the latter is evaluated on a spherical surface, whose radius is related to the fractional order. Mendlovic, *et al.* [146] introduced a fractional wavelet transform (not to be confused with the fractional wavelets proposed by Unser and Blu [211]). It is essentially a fractional Fourier transform, followed by a continuous wavelet transform. The fractional order is determined in such a way as to maximize the mean-square error between the input and the reconstructed signal. The implementation is optical.

There also exist a number of formulations of the Fresnel transform in terms of simple building blocks. Hamam and Bougrenet de la Tocnaye [79] interpret the Fresnel diffraction as the composition of replicas of the original propagated field at well chosen distances related to Talbot planes. In the same spirit, Hamam [78] proposed a formulation of the Fresnel transform using functions that are self-similar and localized. It is however limited to periodic functions.

Another, application of wavelets in optics, closely related to our problem, is the demodulation of interference signals. These signals are usually 1D, or at least, they are treated as if they were 1D. Wavelet techniques to determine the local frequency of a signal are mainly based on the fact that the phase of the continuous wavelet transform of an interference pattern using an analytical wavelet is related to the phase of the signal's analytical counterpart [42]. White light interferograms have been analyzed by Sandoz [183], and Recknagel and Notni [178]. Watkins *et al.* [220] proposed a phase distribution determination algorithm based on the integration of a phase gradient which is, in turn, determined by a continuous wavelet transform. A continuous wavelet transform (using Paul wavelets) has also been used to evaluate optical phase distributions by Afifi *et al.* [1]. Cherbuliez *et al.* [26, 27] used continuous wavelet transforms for dynamic phase shifting, a technique where the object's deformation or motion is responsible for creating the phase shifts. The analysis is performed on the temporal signal acquired at every pixel. Tomassini *et al.* [204] analyzed laser plasma interferograms with a continuous wavelet transform ridge extraction technique. More recently, a method that combines spectral interferometry and wavelength multiplexing was introduced for 3D imaging [60]. The decoding relies on the signal analysis

0000011010

based on its continuous wavelet transform.

More traditional applications of waveletlike denoising can also be found in situations that are specific to coherent imaging systems, namely speckle noise. Wavelet thresholding algorithms for speckle noise suppression have been proposed and compared [50, 51, 66, 67, 98, 112, 136].

The approach we follow in Chapter 2 is in many aspects close to the concept of unitary equivalence proposed by Baraniuk and Jones [5]. The idea is to go into a transformed domain (via a change of basis using a unitary transform) thus converting the traditional systems into new systems with different properties that are possibly better adapted to existing image processing techniques.

Finally, this review would not be complete without a glimpse at Gabor wavelets. Meyer [150, Chap. 5] acknowledges Gabor as the first person to have introduced time-frequency wavelets. However, he also notices that "difficulties appear when a signal is to be decomposed into Gabor wavelets. As long as only continuous decompositions are considered [...] Gabor wavelets may be used as if they were an orthonormal basis, but the corresponding discrete algorithms are either inexistent or require considerable tricks that make them too complicated". The stability of Gabor expansions [61] has notably been studied by Bastiaans [7] and Janssen [94]. Coifman and Meyer showed that modulated Gaussians can form unconditional Wilson bases of L_2 [30]. Yet, the above cited examples lack a representation of functions in stable and nonredundant multiresolution bases. A way to circumvent this problem is the topic of Chapter 2.

1.4   Organization of the Thesis

The thesis is organized as follows.

In Chapter 2, we present a new family of waveletlike functions: Fresnelets. They are a conceptual, mathematical, and practical tool that is of use whenever the Fresnel transform is involved. We give the mathematical foundations and applications to hologram simulation and reconstruction. An important result that we derive is a Heisenberg-like uncertainty principle for the Fresnel transform. This also allows us to review the Fresnel transform's main properties since they are involved for the construction of the Fresnelet bases. Two properties that are inherent to Fresnelets, their space-frequency localization and their energy compaction ability, will be the starting points for applications described in Chapters 3 and 5, respectively.

In Chapter 3, we take advantage of the first joint localization property and come up with a zero-order term and twin-image removal algorithm that takes full advantage of the space-frequency information

repartition in the Fresnelet domain.

In Chapter 4, we propose an alternative procedure to the optical-reconstruction-inspired algorithm, that is, the separation of the reconstruction problem into two distinct problems: phase and amplitude retrieval (a fringe analysis, respectively spatial phase-shifting interferometry problem) and propagation simulation. To this end, we propose a parametric amplitude and phase retrieval method that can be viewed as a generalization of widely-used (both spatial and temporal) phase-shifting algorithms. Its main advantage is that it is applicable for complicated setups, including those that include a microscope objective.

In Chapter 5, we take advantage of the second important property of Fresnelets, namely their ability to produce sparse representations of Fresnel fields and holograms. We use this concept to implement an effective and robust autofocus method, that is, a way to set the distance parameter automatically.

Finally, in Chapter 6, we compare a number of algorithms (previously existing and newly proposed ones) in a variety of situations by quantitative simulation experiments. We conclude that the proposed methods result in flexible algorithms that are competitive with preexisting ones and superior to them in many cases. They are also applicable over a wide range of situations while keeping the computational cost low.

Chapters 2, 3, and 4 are based on the published Refs. [127–129]. A paper based on Chapter 5 has been submitted for publication [130].

1.5 Conventions

We use the following definition of the Fourier transform $\hat{f}(v)$ of a function $f(x)$

$$\hat{f}(v) = \int_{-\infty}^{\infty} f(x) \exp(-2i\pi x v)\,dx, \tag{1.1}$$

$$f(x) = \int_{-\infty}^{\infty} \hat{f}(v) \exp(2i\pi v x)\,dv. \tag{1.2}$$

With this definition, $\|f\| = \|\hat{f}\|$. We recall several relevant properties in Appendix A.

We use the following form of the free-space propagation operator $\mathscr{R}_{(d)}$, defined for functions of two variables as the Fresnel transform

$$\mathscr{R}_{(d)}\{f\}(\mathbf{x}) = \frac{e^{ik_\lambda d}}{i\lambda d} \iint_{-\infty}^{\infty} f(\xi,\eta) \exp\left\{\frac{i\pi}{\lambda d}[(\xi-x)^2 + (\eta-y)^2]\right\}\,d\xi d\eta, \tag{1.3}$$

where λ is the wavelength of the light, $k_\lambda = 2\pi/\lambda$ its wave number, d the propagation distance and $\mathbf{x} = (x, y)$.

0000011100

Chapter 2

Fresnelets: New Multiresolution Wavelet Bases for Digital Holography

Abstract[a]— We propose a construction of new waveletlike bases that are well suited for the reconstruction and processing of optically generated Fresnel holograms recorded on CCD-arrays. The starting point is a wavelet basis of L_2 to which we apply a unitary Fresnel transform. The transformed basis functions are shift-invariant on a level-by-level basis but their multiresolution properties are governed by the special form that the dilation operator takes in the Fresnel domain. We derive a Heisenberg-like uncertainty relation that relates the localization of Fresnelets with that of their associated wavelet basis. According to this criterion, the optimal functions for digital hologram processing turn out to be Gabor functions, bringing together two separate aspects of the holography inventor's work.

We give the explicit expression of orthogonal and semi-orthogonal Fresnelet bases corresponding to polynomial spline wavelets. This special choice of Fresnelets is motivated by their near-optimal localization properties and their approximation characteristics. We then present an efficient multiresolution Fresnel transform algorithm, the Fresnelet transform. This algorithm allows for the reconstruction (backpropagation) of complex scalar waves at several user-defined, wavelength-independent resolutions. Furthermore, when reconstructing numerical holograms, the subband decomposition of the Fresnelet transform naturally separates the image to reconstruct from the unwanted zero-order and twin image terms. This greatly facilitates their suppression. We show results of experiments carried out on both synthetic (simulated) data sets as well as on digitally acquired holograms.

---

[a]This chapter is based on Ref. [127].

2.1   Introduction

In digital Fresnel holography, the hologram results from the interference between the wave reflected or transmitted by the object to be imaged and a reference wave. One arrangement that is often used is to record the distribution of intensity in the hologram plane at the output of a Michelson interferometer. The digital reconstruction of the complex wave (amplitude and phase) near the object is based on the Fresnel transform, an approximation of the diffraction integral [72]. Since Fresnel holography is in essence a lens-less process, sharp details like object edges tend to be spread out over the entire image plane. Therefore, standard wavelets, which are typically designed to

process piecewise smooth signals, will give poor results when applied directly to the hologram. We present a new family of wavelet bases that is tailor-made for digital holography.

While analytical solutions to the diffraction problem can be given in terms of Gauss-Hermite functions [72], those do not satisfy the completeness requirements of wavelet theory [199] and are therefore of limited use for digital processing[1]. This motivates us to come up with basis functions that are well-suited for the problem at hand. The approach that we are proposing here is to apply a Fresnel transform to a wavelet basis of L_2 to simulate the propagation in the hologram formation process and build an adapted wavelet basis.

We have chosen to concentrate on B-spline bases for the following reasons:

- The B-splines have excellent approximation characteristics (in some asymptotic sense, they are π times better than Daubechies wavelets [13]).

- The B-splines are the only scaling functions that have an analytical form in both time and frequency domains; hence, there is at least some hope that we can derive their Fresnel transforms and associated wavelets explicitly.

- The B-splines are nearly Gaussians and their associated wavelets very close to Gabor functions (modulated Gaussians) [207]. This property will turn out to be crucial because we will show that these functions are well localized with respect to the holographic process.

This chapter is organized as follows. In Section 2.2, we define the unitary Fresnel transform in one and two dimensions. In section 2.3 we review several of its key properties that are needed in order to define the new bases. We also investigate the spatial localization properties of the Fresnel transform and derive a Heisenberg-like uncertainty relation. In Section 2.4, we define the Fresnelet bases. We briefly review B-splines and their associated wavelet bases and show how to construct the corresponding Fresnelet bases. We derive an explicit closed-form expression for orthogonal and semi-orthogonal Fresnelet bases corresponding to polynomial spline wavelets. We also discuss their properties including their spatial localization and multiresolution structure. In Section 2.5, we show how to implement our multiresolution Fresnel transform. Finally, in Section 2.6, we apply our method to the reconstruction of holograms using both simulated and real-world data.

---

[1]In particular, they lack a two-scale relation.

2.2 Fresnel Transform

2.2.1 Definition

We define the unitary Fresnel transform with parameter $\tau \in \mathbb{R}_+$ of a function $f \in L_2(\mathbb{R})$ as the convolution integral

$$\tilde{f}_\tau(x) = k_\tau * f(x) \text{ with } k_\tau(x) = \begin{cases} 1/\tau \exp\left(i\pi (x/\tau)^2\right) & \tau > 0 \\ \mathrm{e}^{i\pi/4} \delta(x) & \tau = 0. \end{cases} \tag{2.1}$$

which is well defined in the L_2 sense. Our convention throughout this paper will be to denote the Fresnel transform with parameter τ of a function using the tilde and the associated index τ. The frequency response of the Fresnel operator is:

$$\hat{k}_\tau(v) = \mathrm{e}^{i\frac{\pi}{4}} \mathrm{e}^{-i\pi(\tau v)^2}, \tag{2.2}$$

with the property that $\left|\hat{k}_\tau(v)\right| = 1$, $\forall v \in \mathbb{R}$. As the transform is unitary, we get a Parseval equality:

$$\forall f, g \in L_2(\mathbb{R}) \qquad \langle f, g \rangle = \langle \tilde{f}_\tau, \tilde{g}_\tau \rangle \tag{2.3}$$

and for $f = g$ a Plancherel equality:

$$\forall f \in L_2(\mathbb{R}) \qquad \|f\| = \|\tilde{f}_\tau\|. \tag{2.4}$$

Therefore, we have that $\tilde{f}_\tau \in L_2(\mathbb{R})$. The inverse transform in the space domain is given by:

$$f(x) = (\tilde{f}_\tau * k_\tau^{-1})(x) \text{ with } k_\tau^{-1}(x) = k_\tau^*(x) = \begin{cases} 1/\tau \exp\left(-i\pi (x/\tau)^2\right) & \tau > 0 \\ \mathrm{e}^{-i\pi/4} \delta(x) & \tau = 0. \end{cases}$$
$$\tag{2.5}$$

It is simply derived by conjugating the operator in the Fourier domain:

$$\hat{k}_\tau^{-1}(v) = \mathrm{e}^{-i\frac{\pi}{4}} \mathrm{e}^{i\pi(\tau v)^2} = \hat{k}_\tau^*(v). \tag{2.6}$$

2.2.2 Example: Gaussian Function

The Fresnel transform of the Gaussian function:

$$g(x) = \mathrm{e}^{-\pi(x/\sigma)^2} \tag{2.7}$$

is again a Gaussian, modulated by a chirp function:

$$\tilde{g}_\tau(x) = a \, \mathrm{e}^{-\pi(x/\sigma')^2} \mathrm{e}^{i\pi(x/\tau')^2} \tag{2.8}$$

where $a = \mathrm{e}^{i\pi/4} (\sigma/(\sigma^2 + i\tau^2)^{1/2})$ is the complex amplitude, $\sigma'^2 = (\sigma^4 + \tau^4)/\sigma^2$ is the new variance and $\tau'^2 = (\sigma^4 + \tau^4)/\tau^2$ is the chirp parameter. As the parameter τ increases, the variance and therefore the spatial spreading of the transformed function increases as well. We further investigate this particular aspect of the Fresnel transform in Subsection 2.3.5.

0000011111

2.2.3 Two-Dimensional Fresnel Transform

We define the unitary two dimensional Fresnel transform of parameter $\tau \in \mathbb{R}_+^*$ of a function $f \in L_2(\mathbb{R}^2)$ as the 2D convolution integral

$$\tilde{f}_\tau(\mathbf{x}) = \tilde{f}_\tau(x, y) = (f * K_\tau)(\mathbf{x}) \tag{2.9}$$

where the kernel is:

$$K_\tau(\mathbf{x}) = \frac{1}{\tau^2}\, e^{i\pi(\|\mathbf{x}\|/\tau)^2}. \tag{2.10}$$

A key property is that it is separable:

$$K_\tau(\mathbf{x}) = \frac{1}{\tau^2}\, e^{i\pi(\|\mathbf{x}\|/\tau)^2} = k_\tau(x)\, k_\tau(y). \tag{2.11}$$

Thus, we will be able to perform most of our mathematical analysis in one dimension and simply extend the results to two dimensions by using separable basis functions.

Up to a complex multiplicative constant, this definition is equivalent to the free-space propagation formula in the Fresnel approximation, which relates the complex values of a propagating wave, measured in two planes perpendicular to the direction of propagation and separated by a distance d. Specifically, we have

$$U_d(x, y) = \frac{e^{ik_\lambda d}}{i\lambda d} \iint U(\xi, \eta) \exp\left(\frac{i\pi}{\lambda d}\left((\xi - x)^2 + (\eta - y)^2\right)\right) d\xi d\eta \tag{2.12}$$

$$= -i\, e^{ik_\lambda d}\, \tilde{U}_\tau(x, y), \qquad \tau = \sqrt{\lambda d}, \tag{2.13}$$

where λ is the wavelength of the light an $k_\lambda = 2\pi/\lambda$ its wavenumber. In other words, the amplitudes and phases of the wave at two different depths are related to each other via a 2D Fresnel transform.

2.3 Properties of the Fresnel Transform

Conventional wavelet bases are built using scaled and dilated versions of a suitable template. For building our new wavelet family, it is thus essential to understand how the Fresnel transform behaves with respect to the key operations in multiresolution wavelet theory; i.e. dilation and translation. In Subsections 2.3.1 to 2.3.4, we recall properties of the Fresnel transform that are central to our discourse but are also documented in the optics literature [72, pp. 114–119]. In Subsection 2.3.5, we give a new result, which is an uncertainty relation for the Fresnel transform. For clarity, the results are presented for 1D functions but, using the separability property, they can easily be extended to 2D functions.

0000100000

2.3.1 Duality

To compute the inverse of the Fresnel transform we can use following dual relation:

$$f^*(x) = \left((\tilde{f}_\tau)^* \right)_\tau^{\sim}(x), \quad f \in L_2(\mathbb{R}). \tag{2.14}$$

Computing the inverse Fresnel transform of a function is therefore equivalent to taking its complex conjugate, computing the Fresnel transform and again taking the complex conjugate. In other words, the operator $f \mapsto (\tilde{f}_\tau)^*$ is involutive.

2.3.2 Translation

As the Fresnel transform is a convolution operator, it is obviously shift-invariant:

$$(f(\cdot - x_0))_\tau^{\sim}(x) = \tilde{f}_\tau(x - x_0), \quad x_0 \in \mathbb{R}. \tag{2.15}$$

2.3.3 Dilation

The Fresnel transform with parameter τ of the dilated function $f(x/s)$ is:

$$\left(f\left(\frac{\cdot}{s}\right) \right)_\tau^{\sim}(x) = \tilde{f}_{\tau/s}\left(\frac{x}{s}\right), \quad s \in \mathbb{R}_+^*. \tag{2.16}$$

This relation involves a dilation by s of the Fresnel transform of f with a rescaled parameter $\tau' = \tau/s$. This ratio also appears in the definition of the so-called *Fresnel number* $N_F = (s/\tau)^2$, where $\tau^2 = \lambda d$; it is used to characterize the diffraction of light by a square aperture of half-width s and at a distance d [72].

2.3.4 Link with the Fourier Transform

So far, we have considered the Fresnel transform as a convolution operator. Interestingly, there is also a direct multiplicative relation with the Fourier transform [72]. Computing the Fresnel transform $\tilde{g}_\tau$ of a function $g \in L_2(\mathbb{R})$ can be done by computing the Fourier transform of an associated function $f(x) = \tau k_\tau(x) g(x)$. The frequency variable is then interpreted as an appropriately scaled space variable:

$$\tilde{g}_\tau(x) = k_\tau(x)\, \hat{f}\left(\frac{x}{\tau^2}\right). \tag{2.17}$$

2.3.5 Localization Issues

Our approach for the construction of a Fresnelet basis will take a wavelet basis and transform it. This still leaves many possibilities to choose the original basis. A suitable basis should take into account one of the least intuitive aspects of holography, namely that the propagation process tends to spread out features that are initially well localized in

the object domain. Getting a better understanding of the notion of resolution in holography and setting up a criterion that will guide us in the choice of an optimal wavelet is what we are after in this section.

The tight link between the Fresnel and the Fourier transform (2.17) suggests that they should both have similar (de)localization properties. Here we derive an uncertainty relation for the Fresnel transform that is the analog of the Heisenberg inequality [81] for the Fourier transform.

In the sequel, we denote the average μ_f of the squared modulus of a function $f \in L_2(\mathbb{R})$ by:

$$\mu_f = \frac{1}{\|f\|^2} \int_{-\infty}^{\infty} x|f(x)|^2 \, dx$$

and its variance σ_f^2 around this average by:

$$\sigma_f^2 = \frac{1}{\|f\|^2} \int_{-\infty}^{\infty} (x - \mu_f)^2 |f(x)|^2 \, dx.$$

Theorem 1 (Uncertainty relation for the Fresnel transform) *Let $g \in L_2(\mathbb{R})$ and $\tilde{g}_\tau \in L_2(\mathbb{R})$ its Fresnel transform with parameter τ. We have following inequality for the product of their variances:*

$$\sigma_g^2 \sigma_{\tilde{g}_\tau}^2 \geq \frac{\tau^4}{16\pi^2}. \tag{2.18}$$

This inequality is an equality if and only if there exist x_0, ω_0, b real and a complex amplitude a such that:

$$g(x) = a \, e^{i\omega_0 x} \, e^{-b(x-x_0)^2} \, e^{-i\pi(x/\tau)^2} \tag{2.19}$$

Furthermore, if $g(x)$ is real valued, the following relation holds:

$$\sigma_g^2 \sigma_{\tilde{g}_\tau}^2 \geq \frac{\tau^4}{16\pi^2} + \sigma_g^4. \tag{2.20}$$

This inequality is an equality if and only if there exist x_0, a, b real, such that:

$$g(x) = a \, e^{-b(x-x_0)^2} \tag{2.21}$$

Also, (2.20) implies a lower bound on the variance for $\sigma_{\tilde{g}_\tau}$ that is independent of g:

$$\sigma_{\tilde{g}_\tau}^2 \geq \frac{\tau^2}{2\pi}.$$

The proof of Theorem 1 is given in Appendix 2.A.

This result implies that narrow functions yield functions with a large energy support when they are transformed. It suggests that Gaussians and Gabor-like functions, modulated with the kernel function

0000100010

as in (2.19) should be well suited for processing and reconstructing holograms as they minimize the spatial spreading of the energy. This is especially satisfying because it brings two separate aspects of Gabor's research together: he is both the inventor of holography [62] and of the Gabor transform [61, 94], which is a signal representation as a linear combination of atoms of the form (2.19). We are not aware of anyone having pointed out this connection before.

We will base our Fresnelets construction on wavelet bases that are close to these optimal functions. Practically, in the case of a digital hologram measurement where a transformed function is available over a finite support and with a given sampling step, we may use the above uncertainty relation to get a bound on the maximal resolution to expect when reconstructing the original function.

A direct illustration of the second part of this Theorem can be found in the example of Subsection 2.2.2; indeed, it can be verified that the product of the variance of the Gaussian and that of its Fresnel transform achieves the lower bound in (2.20).

2.4 Fresnelet Bases

To construct our new Fresnelet bases, we will apply a Fresnel transform to a wavelet basis. Here, we will explain what happens when we apply the transform to a general Riesz basis of $L_2(\Omega)$, where the dimension of the domain Ω is arbitrary e.g. $\Omega = \mathbb{R}$ or $\mathbb{R}^2$.

2.4.1 Fresnel Transform of a Riesz Basis

Let $\{u_l\}_{l \in \mathbb{Z}}$ be a Riesz basis of $L_2(\Omega)$ and $\{v_l\}_{l \in \mathbb{Z}}$ its dual. Then, $\forall f \in L_2(\Omega)$, we can write following expansion:

$$f = \sum_l \underbrace{\langle f, v_l \rangle}_{c_l} u_l = \sum_l \langle f, u_l \rangle v_l \tag{2.22}$$

Let $\tilde{u}_l = \mathcal{U} u_l$ where $\mathcal{U}$ is a unitary operator (e. g. the Fresnel transform). First, it is easy to see that $\mathcal{U}$ maps the biorthogonal set $S = \{u_l, v_l\}_{l \in \mathbb{Z}}$ into another biorthogonal set $\tilde{S} = \{\tilde{u}_l, \tilde{v}_l\}_{l \in \mathbb{Z}}$:

$$\begin{aligned} \langle \tilde{v}_l, \tilde{u}_m \rangle &= \langle \mathcal{U} v_l, \mathcal{U} u_m \rangle \\ &= \langle \underbrace{\mathcal{U} \mathcal{U}^\dagger}_{1} v_l, u_m \rangle = \delta_{l,m}. \end{aligned}$$

Here $\mathcal{U}^\dagger$ denotes the adjoint of $\mathcal{U}$. Let us now show that $\tilde{S}$ is also complete. For the set S, we define the sequence:

$$f_N = \sum_{l=1}^{N} \langle f, v_l \rangle u_l, \ \forall f \in L_2(\Omega)$$

and have the completeness equation:

$$\lim_{N\to\infty} \|f - f_N\|^2 = 0. \tag{2.23}$$

Note that the Riesz basis hypothesis ensures that $f_N \in L_2(\Omega)$. Because $\mathcal{U}$ is unitary, we have:

$$\begin{aligned}\langle f, v_l\rangle &= \langle \mathcal{U}f, \mathcal{U}v_l\rangle \\ &= \langle \tilde{f}, \tilde{v}_l\rangle\end{aligned} \tag{2.24}$$

and therefore:

$$\|f - f_N\|^2 = \|\tilde{f} - \tilde{f}_N\|^2$$

which proves that the transformed set $\tilde{S}$ is complete as well.

Similarly, the Parseval relation (2.24) can also be used to prove that S and $\tilde{S}$ have the same Riesz bounds. The Riesz bounds are the tightest constants $A > 0$ and $B < \infty$ that satisfy the Riesz inequality:

$$A\|\langle v_l, f\rangle\|^2_{\ell_2} \le \|f\|^2_{L_2} \le B\|\langle v_l, f\rangle\|^2_{\ell_2}.$$

They are the same for the transformed set:

$$A\|\langle \tilde{v}_l, \tilde{f}\rangle\|^2_{\ell_2} \le \|\tilde{f}\|^2_{L_2} \le B\|\langle \tilde{v}_l, \tilde{f}\rangle\|^2_{\ell_2}.$$

Thus, we can conclude that the Fresnel transform, which is a unitary operator from $L_2(\Omega)$ into $L_2(\Omega)$, maps Riesz bases into other Riesz bases, with the same Riesz bounds. Similarly, if we only consider a subset of basis functions that span a subspace of $L_2(\Omega)$ (e.g. a multiresolution subspace) we can show that it maps into a transformed set that is a Riesz basis of the transformed subspace with the same Riesz bounds.

Relation (2.24) is important for this proof but it is also most relevant for the reconstruction of an image f given its transform $\tilde{f}$. It indicates that we can obtain the expansion coefficients in (2.22) directly by computing the series of inner products $\langle \tilde{f}, \tilde{v}_l\rangle$. This is one of the key ideas for our construction.

2.4.2 B-splines

The uncertainty relation for the Fresnel transform suggests the use of Gabor-like functions. Unfortunately, these functions cannot yield a multiresolution basis of $L_2(\mathbb{R})$. They don't satisfy the partition of unity condition, implying that a representation of a function in term of shifted Gaussians won't converge to the function as the sampling step goes to zero [206]. Furthermore, they don't satisfy a two-scale relation which is required for building wavelets and brings many advantages regarding implementation issues.

0000100100
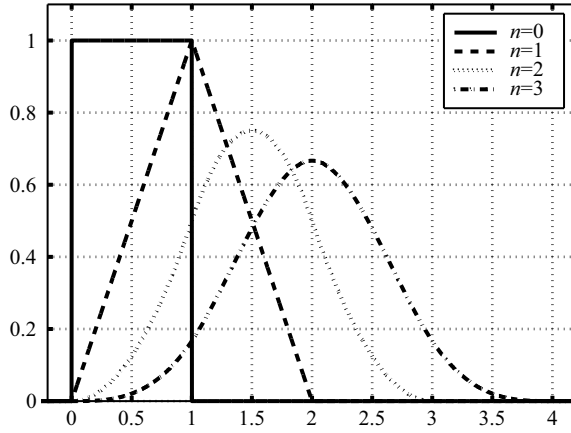
Fig. 2.1. B-splines of degree $n = 0, 1, 2, 3$.

We will therefore base our construction on B-splines which are Gaussian-like functions that do yield wavelet bases; they are also well localized in the sense of the uncertainty principle for the Fresnel transform (2.20).

B-splines [213] are defined in the Fourier domain by :

$$\hat{\beta}^n(\nu) = \left(\frac{1 - e^{-2i\pi\nu}}{2i\pi\nu} \right)^{n+1} = \text{sinc}^{n+1}(\nu) \, e^{-i\pi\nu(n+1)}$$

where $\text{sinc}(x) = \sin(\pi x)/(\pi x)$ and $n \in \mathbb{N}$.

The corresponding expression for the B-spline of degree n in the time domain (see Fig. 2.1) is:

$$\beta^n(x) = \Delta^{n+1} * \frac{(x)_+^n}{n!}$$

where $(x)_+^n = \max(0, x)^n$ (one-sided power function); Δ^{n+1} is the $(n + 1)$th finite-difference operator:

$$\Delta^{n+1} = \sum_{k=0}^{n+1} (-1)^k \binom{n+1}{k} \delta(x - k)$$

which corresponds to the $(n + 1)$-fold iteration of the finite difference operator (see [213]): $\Delta = \delta(x) - \delta(x - 1)$. Explicitly, we have following expression for the B-spline of degree n:

$$\beta^n(x) = \sum_{k=0}^{n+1} (-1)^k \binom{n+1}{k} \frac{(x - k)_+^n}{n!}. \tag{2.25}$$

This definition is equivalent to the standard approach where the B-splines of degree n are constructed from the $(n + 1)$-fold convolution

of a rectangular pulse:

$$\beta^n(x) = \underbrace{\beta^0 * \cdots * \beta^0}_{n+1 \text{ times}}(x)$$

$$\beta^0(x) = \begin{cases} 1, & 0 < x < 1 \\ \frac{1}{2}, & x = 0 \text{ or } 1 \\ 0, & \text{otherwise.} \end{cases}$$

2.4.3 Polynomial Spline Wavelets

The B-splines satisfy all the requirements of a valid scaling function of $L_2(\mathbb{R})$, that is, they satisfy the three necessary and sufficient conditions [199]:

$$\text{Riesz Basis:} \qquad 0 < A \leq \sum_{k \in \mathbb{Z}} \left| \hat{\beta}^n(v+k) \right|^2 \leq B < \infty$$

$$\text{Two-scale relation:} \quad \beta^n\left(\frac{x}{2}\right) = \sum_{k \in \mathbb{Z}} h(k)\beta^n(x-k) \qquad (2.26)$$

$$\text{Partition of unity:} \quad \sum_{k \in \mathbb{Z}} \beta^n(x-k) = 1$$

where the filter $h(k)$ is the binomial filter $h(k) = \frac{1}{2^n}\binom{n+1}{k}$. These conditions ensure that B-splines can be used to generate a multiresolution analysis of $L_2(\mathbb{R})$.

Unser *et al.* [208] have shown that one can construct a general family of semi-orthogonal spline wavelets of the form:

$$\psi^n\left(\frac{x}{2}\right) = \sum_k g(k)\beta^n(x-k) \qquad (2.27)$$

such that the functions

$$\left\{ \psi^n_{j,k} = 2^{\frac{-j}{2}} \psi^n(2^{-j}x - k) \right\}_{j \in \mathbb{Z}, k \in \mathbb{Z}} \qquad (2.28)$$

form a Riesz basis of $L_2(\mathbb{R})$. These wavelets come in different brands: orthogonal, B-spline (of compact support), interpolating, etc... They are all linear combinations of B-splines and are thus entirely specified from the sequence $g(k)$ in equation (2.27). Here, we will consider B-spline wavelets [209], which have the shortest support in the family.

The main point here is that by using the properties of the Fresnel transform (linearity, shift invariance and scaling), we can easily derive the family of functions $\left\{ \left(\psi^n_{j,k} \right)^{\sim}_{\tau} = k_\tau * \psi^n_{j,k} \right\}_{j \in \mathbb{Z}, k \in \mathbb{Z}}$, provided that we know the Fresnel transform of their main constituent, the B-spline.

0000100110

2.4.4 Fresnelets

In this section, we introduce our new wavelets: Fresnelets. They will be specified by taking the Fresnel transform of (2.27). Thus, the remaining ingredient is to determine the Fresnel transform of the B-splines.

F-splines

We define the Fresnel spline, or F-spline of degree $n \in \mathbb{N}$ and parameter $\tau \in \mathbb{R}_+^*$ (denoted $\tilde{\beta}_\tau^n(x)$) as the Fresnel transform with parameter τ of a B-spline $\beta^n(x)$ of degree n:

$$\tilde{\beta}_\tau^n(x) = (\beta^n * k_\tau)(x).$$

Theorem 2 *The F-spline of degree n and parameter τ has the closed form:*

$$\tilde{\beta}_\tau^n(x) = \sum_{k=0}^{n+1} (-1)^k \binom{n+1}{k} u_{n,\tau}(x - k) \tag{2.29}$$

where:

$$u_{n,\tau}(x) = \int_0^x \frac{(x - \xi)^n}{n!} k_\tau(\xi) \, d\xi. \tag{2.30}$$

The proof of Theorem 2 is given in Appendix 2.B.

F-splines have many similarities with B-splines. For example, to get (2.29), one just substitutes the one-sided power function used in the definition of the B-spline (2.25) with the functions $u_{n,\tau}$.

Theorem 3 *The functions $u_{n,\tau}$ can be calculated recursively:*

$$u_{n,\tau}(x) = \frac{\tau}{2i\pi n!} x^{n-1} - \frac{\tau^2}{2i\pi n} u_{n-2,\tau}(x) + \frac{x}{n} u_{n-1,\tau}(x). \tag{2.31}$$

For $n = 0$ we have:

$$u_{0,\tau}(x) = \frac{1}{\sqrt{2}} \left(C\left(\frac{\sqrt{2}}{\tau} x \right) + i S\left(\frac{\sqrt{2}}{\tau} x \right) \right)$$

where $C(x)$ and $S(x)$ are the so-called Fresnel integrals*:*

$$C(x) = \int_0^x \cos\left(\frac{\pi}{2} t^2 \right) dt, \quad S(x) = \int_0^x \sin\left(\frac{\pi}{2} t^2 \right) dt$$

For $n = 1$ we have:

$$u_{1,\tau}(x) = x \, u_{0,\tau}(x) - \frac{\tau^2}{2i\pi} \left(k_\tau(x) - \frac{1}{\tau} \right).$$

0000100111

The proof of Theorem 3 is given in Appendix 2.C.

This gives us a straightforward way to evaluate the F-splines as the Fresnel integrals can be computed numerically [174]. Furthermore, we can also transpose the well-known B-spline recursion formula:

$$\beta^n(x) = \frac{x}{n}\beta^{n-1}(x) + \frac{n+1-x}{n}\beta^{n-1}(x-1) \qquad (2.32)$$

to the Fresnel domain.

Theorem 4 *We have following recursion formula for the F-splines:*

$$\tilde{\beta}_\tau^n(x) = \frac{x\tilde{\beta}_\tau^{n-1}(x) + (n+1-x)\tilde{\beta}_\tau^{n-1}(x-1)}{n}$$

$$+ \frac{i\tau^2}{2\pi n}\Delta^2\tilde{\beta}_\tau^{n-2}(x). \quad (2.33)$$

The proof of Theorem 4 is given in Appendix 2.D.

Fresnelet Multiresolutions

Let us now transpose the classical multiresolution relations of wavelet theory to the Fresnelet domain. The two scale relation (2.26) becomes:

$$\tilde{\beta}_{\tau/2}^n\left(\frac{x}{2}\right) = \sum_k h(k)\tilde{\beta}_\tau^n(x-k) \qquad (2.34)$$

In classical wavelet theory, embedded multiresolution spaces are generated through dilation and translation of one single function. The Fresnel transform preserves the embeddedness of those spaces. The important modification comes from the *dilation* relation (2.16) which changes the generating function from one scale to the next. The difference is that in the transformed domain there is one generating function for each *scale*.

Formally, we consider, for $j \in \mathbb{Z}$, the sequence of spaces $\{\tilde{V}_{j,\tau}\}$ defined as:

$$\tilde{V}_{j,\tau} = \operatorname*{span}_{k\in\mathbb{Z}}\left\{\tilde{\beta}_{\tau2^{-j}}^n(2^{-j}x-k)\right\} \cap L_2(\mathbb{R})$$

corresponding to the sequence of spaces $\{V_j\}$ defined as:

$$V_j = \operatorname*{span}_{k\in\mathbb{Z}}\left\{\beta^n(2^{-j}x-k)\right\} \cap L_2(\mathbb{R}).$$

The subspaces V_j satisfy the requirements for a multiresolution analysis [199]:

1. $V_{j+1} \subset V_j$ and $\bigcap V_j = 0$ and $\overline{\bigcup V_j} = L_2(\mathbb{R})$ (completeness).

2. Scale invariance: $f(x) \in V_j \Leftrightarrow f(2x) \in V_{j-1}$.

0000101000

3. Shift invariance: $f(x) \in V_0 \Leftrightarrow f(x - k) \in V_0$.

4. Shift-invariant basis: V_0 has a stable Riesz basis $\{\beta^n(x - k)\}$.

For the sequence $\{\tilde{V}_{j,\tau}\}$ the shift-invariance is preserved within each scale but requirement 2 is clearly not fulfilled because of the scaling property (2.16) of the Fresnel transform. We nevertheless get a modified set of multiresolution analysis requirements for the Fresnel transform:

1') $\tilde{V}_{j+1,\tau} \subset \tilde{V}_{j,\tau}$ and $\bigcap \tilde{V}_{j,\tau} = 0$ and $\overline{\bigcup \tilde{V}_{j,\tau}} = L_2(\mathbb{R})$ (completeness).

2') Scale invariance: $f(x) \in \tilde{V}_{j,\tau} \Leftrightarrow \tilde{f}_{\sqrt{3}\tau}(2x) \in \tilde{V}_{j-1,\tau}$.

3') Shift invariance: $f(x) \in \tilde{V}_{0,\tau} \Leftrightarrow f(x - k) \in \tilde{V}_{0,\tau}$.

4') Shift-invariant basis: V_0 has a stable Riesz basis $\left\{\tilde{\beta}_\tau^n(x - k)\right\}$.

Condition 2' is obtained by observing that $f(x) \in \tilde{V}_{j,\tau} \Leftrightarrow f * k_\tau^{-1} \in V_j$. As we require the V_j to satisfy the scale invariance condition 2, we have $f * k_\tau^{-1}(2x) \in V_{j-1}$ hence $(f * k_\tau^{-1}(2\cdot)) * k_\tau(x) \in \tilde{V}_{j-1,\tau}$. And finally:

$$\left(f * k_\tau^{-1}(2\cdot)\right) * k_\tau(x) = (f * k_\tau^*) * k_{2\tau}(2x)$$
$$= e^{i\frac{\pi}{4}} \tilde{f}_{\sqrt{3}\tau}(2x).$$

Specifically, the generating functions corresponding to the B-spline wavelets of (2.27) are:

$$\tilde{\psi}_{\tau/2}^n \left(\frac{x}{2}\right) = \sum_k g(k) \tilde{\beta}_\tau^n(x - k)$$

where $\tilde{\beta}_\tau^n(x)$ is given by (2.29). The corresponding Fresnelets are such that:

$$\operatorname*{span}_{k \in \mathbb{Z}} \left\{\tilde{\psi}_{\tau/2}^n\left(\frac{x}{2} - k\right)\right\} \perp \operatorname*{span}_{k \in \mathbb{Z}} \left\{\tilde{\beta}_{\tau/2}^n\left(\frac{x}{2} - k\right)\right\}.$$

For the multiresolution subspaces, we have that the residual spaces $\tilde{W}_{j,\tau}$ defined as:

$$\tilde{W}_{j,\tau} = \operatorname*{span}_{k \in \mathbb{Z}} \left\{\tilde{\psi}_{\tau 2^{-j}}^n(2^{-j}x - k)\right\}.$$

are such that

$$\tilde{W}_{j+1,\tau} \perp \tilde{V}_{j+1,\tau}$$

and

$$\tilde{W}_{j+1,\tau} \oplus \tilde{V}_{j+1,\tau} = \tilde{V}_{j,\tau}.$$

The above expressions extend the meaning of multiresolution to the fresnelet domain.
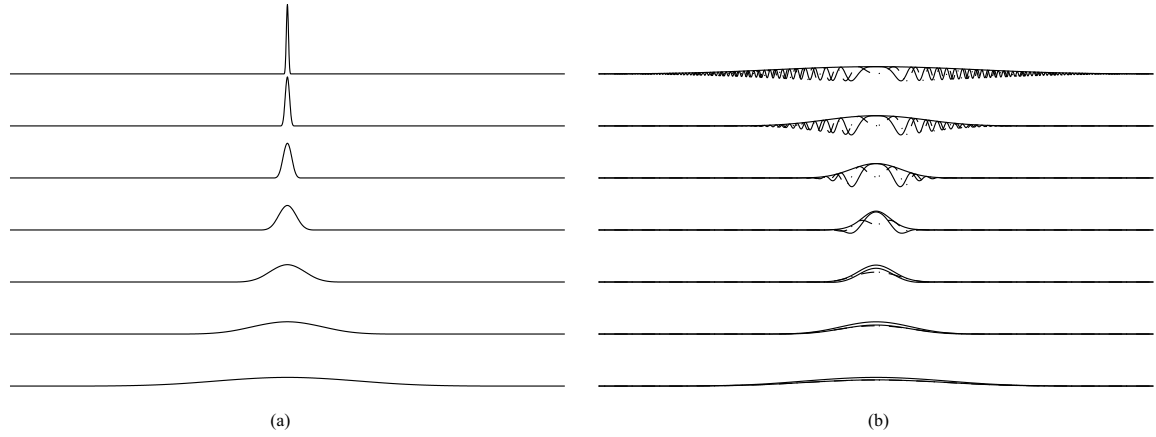
Fig. 2.2.   B-Spline multiresolution and its Fresnel counterpart.   (a) B-splines: $2^{(-j/2)}\beta^3(2^{-j}x)$, $j = -2,-1,0,1,2,3,4$. (b) Corresponding F-splines: $2^{(-j/2)}\tilde{\beta}^3_{\tau 2^{-j}}(2^{-j}x)$. In this illustration, $\tau = 0.9$. The real part is displayed with a continuous, the imaginary part with a dashed line. For the F-splines, we also show the envelopes of the signals.

Fresnelet multiresolution example

In Fig. 2.2 we show a sequence of dyadic scaled B-splines of degree $n = 3$ and their counterpart in the Fresnel domain. The effect of the spreading is clearly visible: as the B-splines get finer ($j = 1, 2, 3, 4$) the corresponding F-splines get larger. In contrast to the Fourier transform, as the B-splines get larger ($j = -1, -2$), the corresponding F-splines' support doesn't get smaller than the B-splines'. This behavior is in accordance with relation (2.20).

The main practical consequence for us is: if we want to reconstruct a hologram at a fine scale, that is, express it as a sum of narrow B-splines, the equivalent basis functions on the hologram get larger. Our special choice of Fresnelet bases limits this phenomenon as much as possible; it is nearly optimal in the sense of our uncertainty relation for real functions (2.20) as they asymptotically converge to Gabor functions [207].

2.5   Implementation of the Fresnelet Transform

In this section we derive a numerical Fresnelet transform algorithm based on our Fresnelets decomposition.

We consider a function $\tilde{f}_\tau(x)$ which is the Fresnel transform of a function $f \in L_2(\mathbb{R})$, i.e., $\tilde{f}_\tau(x) = k_\tau * f(x)$. In a digital holography experiment, this would be the measured phase and amplitude of a propagated wave (without interference with a reference wave). Given some measurements of $\tilde{f}$, the goal is thus to find the best approximation of f in our multiresolution basis. For instance, one can start the process by determining the coefficients c_k that give the closest approximation

of f (in the L_2 sense) at the finest scale of representation:

$$f = \sum_k c_k u(x-k), \quad c_k = \langle f, v(x-k) \rangle = \langle \tilde{f}, \tilde{v}(x-k) \rangle$$

where u and v (respectively $\tilde{u}$ and $\tilde{v}$) are dual bases that are linear combinations of B-splines β^n (respectively F-splines $\tilde{\beta}_\tau$).

Therefore we only need to compute the inner-products of the transformed function with the shifted F-splines that have been appropriately rescaled:

$$d_k = \left\langle f, \frac{1}{h}\beta^n\left(\frac{\cdot}{h}-k\right) \right\rangle = \left\langle \tilde{f}_\tau, \frac{1}{h}\tilde{\beta}^n_{\tau/h}\left(\frac{\cdot}{h}-k\right) \right\rangle. \qquad (2.35)$$

Our present implementation is based on a convolution evaluated in the Fourier domain using FFTs. It can be justified as follows. Using Plancherel's identity for the Fourier transform, we express the inner products (2.35) as:

$$d_k = \left\langle \hat{\tilde{f}}_\tau, \hat{\tilde{\beta}}^n_{\tau/h}(h\cdot)\, e^{-2i\pi kh\cdot} \right\rangle$$
$$= \int \hat{\tilde{f}}_\tau(v)\hat{\tilde{\beta}}^n_{\tau/h}(hv)\, e^{-2i\pi khv}\, dv.$$

In practice, we don't know $\tilde{f}_\tau(x)$ in a continuous fashion, but we can easily compute a sampled version of its Fourier transform by applying the FFT to the measured values. If we also approximate the above integral by a Riemann sum, we end up with the implementation formula:

$$d_k = \frac{1}{NT} \sum_{l=-N/2+1}^{N/2} \hat{\tilde{f}}_\tau\left(\frac{l}{NT}\right)\hat{\tilde{\beta}}^n_{\tau/h}\left(\frac{hl}{NT}\right) e^{-2i\pi khl/(NT)}$$

where T is the sampling step of the measured function. We can make use of the FFT a second time to compute this sum if we consider sampling steps on the reconstruction side that are multiples of the sampling step of the measured function: $h = mT$, $m = 1, 2, \dots$, then:

$$d_k = \frac{1}{NT} \sum_{l=-N/2+1}^{N/2} \hat{\tilde{f}}_\tau\left(\frac{l}{NT}\right)\hat{\tilde{\beta}}^n_{\tau/(mT)}\left(m\frac{l}{N}\right) e^{-2i\pi mkl/N}$$

The algorithm is thus equivalent to a filtering followed by downsampling by m. It is also possible to proceed hierarchically by applying the standard wavelet decomposition algorithm once we have the fine scale coefficients d_k.

See also the FFT implementation of the fractional spline wavelet transform proposed by Blu and Unser [14].

Fig. 2.3.   (a) Amplitude and (b) phase of the test target. The bars width is 256μm. The sampling step is $T = 10\mu$m and 512×512 samples are evaluated. The amplitude is equal to 1 (dark gray) or $\sqrt{2}$ (light gray). The phase is equal to 0 (black) or $\pi/4$ (light gray). (c) Perspective view. The grayscale is representative for the amplitude and the elevation for the phase.
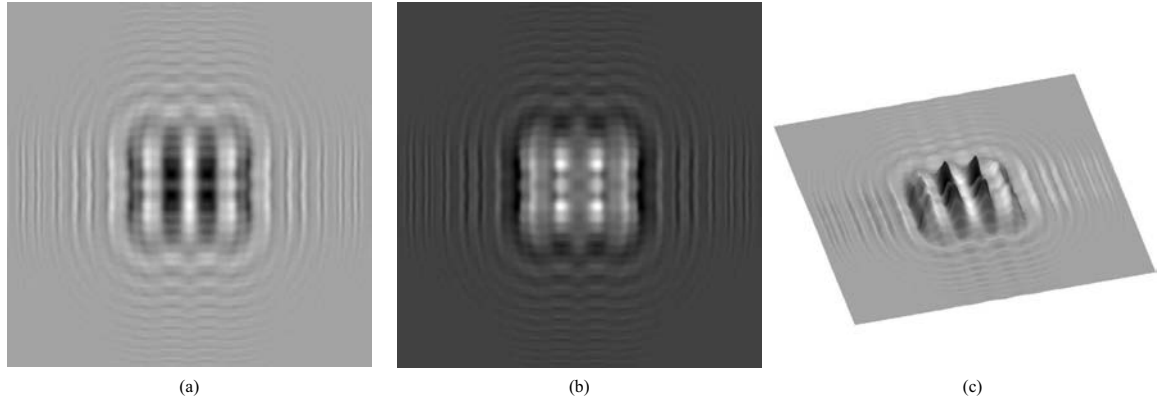
Fig. 2.4.   Propagated target's (a) amplitude and (b) phase. $d = 30$ cm and $\lambda = 632.8$ nm. The sampling step is $T = 10\mu$m and 512×512 samples are evaluated. (c) Perspective view.

2.6   Applications and Experiments

We will now validate our multiresolution Fresnelet-based algorithm and illustrate it in practice on experimental digital holographic data.

2.6.1   Simulation: Propagation of a Test Wave Front

First, we will use our Fresnelet formalism to compute the Fresnel transform of a test pattern that will be used as gold standard to evaluate our algorithm. Although our methodology is more general, for explanatory purposes we consider the case of a plane wave that is being reflected on a test target. The test target is given by three bars. They are of a given thickness and have a different reflectivity than the background they lie on. A plane wave that travels in a normal direction to the target is reflected. In a plane close to the target, the reflected wave's phase is directly proportional to the target's topology whereas

0000101100

the wave's amplitude characterizes the target's reflectivity. The key motif of this test pattern is a bar $b(x, y)$ expressed as a tensor product of two B-splines of degree 0:

$$b(x, y) = e^{i3\pi/4} \, \beta^0 \left(\frac{x}{w_x} \right) \beta^0 \left(\frac{y}{w_y} \right) + \sqrt{2}$$

$$= \begin{cases} e^{i\frac{\pi}{4}}, & \text{on the bar} \\ \sqrt{2}, & \text{outside.} \end{cases} \qquad (2.36)$$

Its Fresnel transform of parameter τ is:

$$\tilde{b}_\tau(x, y) = e^{i3\pi/4} \, \tilde{\beta}^0_{\tau/w_x} \left(\frac{x}{w_x} \right) \tilde{\beta}^0_{\tau/w_y} \left(\frac{y}{w_y} \right) + \sqrt{2} \, e^{i\pi/2}. \qquad (2.37)$$

The amplitude and phase of the target and of the propagated target are shown in Figs. 2.3 and 2.4. More complex targets or different phases and amplitudes can be implemented easily with this method.

2.6.2 Backpropagation of a Diffracted Complex Wave

In this experiment, we took the analytical propagated target we just described as the input for our multiresolution Fresnelet transform algorithm. We reconstructed the original target at dyadic scales. In concrete terms, we computed the inner products with F-splines of varying widths: $\tilde{\beta}^n_{\tau/2^j}(x/2^j)\tilde{\beta}^n_{\tau/2^j}(y/2^j)$, $j = 0, 1, 2, 3, 4$, $n = 3$. We then reconstructed the corresponding images using the underlying spline model. This is also equivalent to running the inverse wavelet transform algorithm up to a specified scale. The results are presented in Fig. 2.5. At the finest scale ($j = 0$), the sampling step is the same as the one used to sample the propagated wave. To ensure that the reconstructed wave agrees with the initial analytical target, we computed the peak signal to noise ratio (PSNR) of the reconstructed amplitude and phase for the finest reconstruction scale $j = 0$. We took following definition of the PSNR:

$$\text{PSNR} = 10 \log_{10} \left(\frac{(\max\{|f|\} - \min\{|f|\})^2}{\frac{1}{N_x N_y} \sum_{k,l} |f(k, l) - f'(k, l)|^2} \right)$$

were f is our (complex) gold standard target and f' the reconstructed target. We obtain a PSNR of 23.10 dB. We can thus say that our algorithm reconstructs the target reasonably well.

2.6.3 Hologram Reconstruction

For this experiment, we considered true holographic data, recorded using a similar system as in [36]. We give a simplified diagram of the experimental setup in Fig. 2.6.
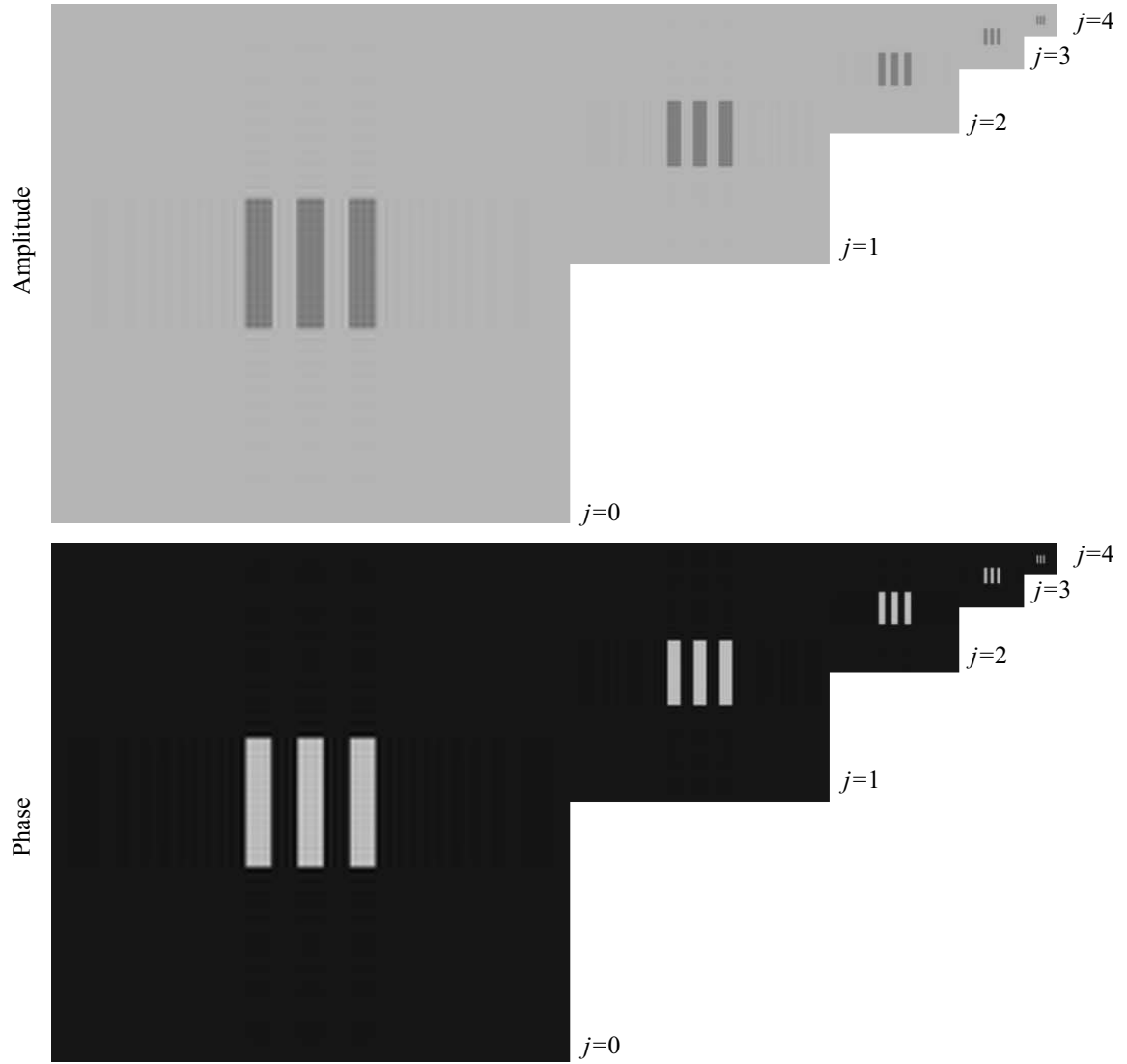
Fig. 2.5. Reconstructed amplitude (top) and phase (bottom).

An object (United States Air Force 1951 (USAF 1951) target) was illuminated using a He-Ne laser ($\lambda = 632.8$nm). The reflected wave was then directed to the 776×572 pixels CCD camera. The camera recorded the interference (hologram) of this propagated wave with a plane reference wave in an off-axis geometry. The sampling step of the CCD was $T = 10\mu$m.

We denote $f(x, y)$ the reflected wave in the vicinity of the object and $\tilde{f}_\tau(x, y)$ the complex amplitude of the propagated wave in the CCD plane. The hologram is the intensity $I(x, y)$ measured by the camera and results from the interference of the propagated wave $\tilde{f}_\tau$ and the reference (plane) wave $R(x, y) = A e^{i(k_x x + k_y y)}$:

$$I(x, y) = |\tilde{f}_\tau(x, y) + R(x, y)|^2 = |\tilde{f}_\tau|^2 + |R|^2 + R^* \tilde{f}_\tau + R(\tilde{f}_\tau)^*. \qquad (2.38)$$

The measured hologram is reproduced in Fig. 2.7.
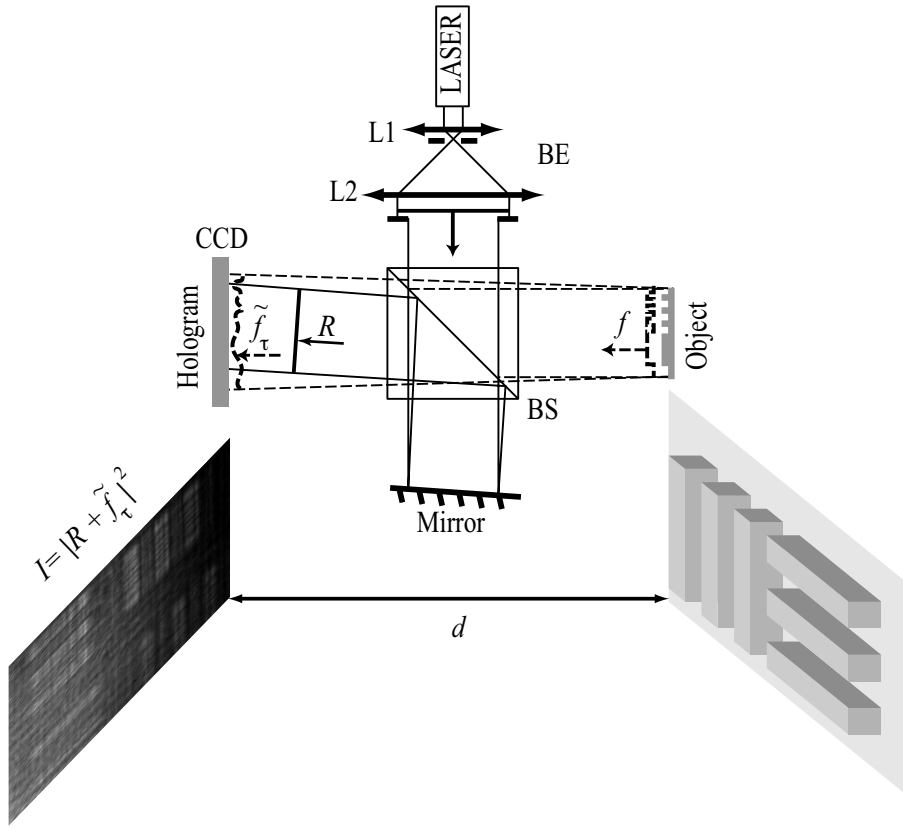
Fig. 2.6. Experimental digital holography setup. A He-Ne LASER ($\lambda = 632.8$nm) beam is expanded by the beam expander (BE) system made of two lenses L1 and L2 and diaphragms. The beam-splitter BS splits the beam. One part illuminates the object. The reflected wave f propagates to the CCD camera at a distance d of the object. In the camera plane the propagated wave is $\tilde{f}_\tau$ where $\tau^2 = \lambda d$. The second part of the beam is reflected by a slightly tilted mirror and impinges on the CCD with a certain angle i.e., its wave vector $\mathbf{k} = (k_x, k_y, k_z)$ has nonzero components k_x and k_y. The plane reference wave evaluated in the plane of the CCD is $R(x, y) = Ae^{i(k_x x + k_y y)}$. The interference of $\tilde{f}_\tau$ and R gives the hologram $I = |R + \tilde{f}_\tau|^2$.

The two first terms in (2.38) are known as the *zero-order*, the third and fourth terms as the *image* and *twin image* terms respectively [72]. In the frequency domain, their energy is concentrated around three frequencies: $(0,0)$ for the zero-order, $(-k_x, -k_y)$ for the image and (k_x, k_y) for the twin image. This is clearly visible in Fig. 2.8.

Prior to reconstructing $f(x, y)$ we multiplied the hologram by a numerical reference wave $R' = e^{i(k'_x x + k'_y y)}$:

$$R'I = R'|\tilde{f}_\tau|^2 + R'|R|^2 + R'R^* \tilde{f}_\tau + R'(\tilde{f}_\tau)^* R.$$

The values k'_x and k'_y were adjusted precisely to the experimental values k_x, k_y, such that the third term (which is the one we are interested in) becomes $R'R^* \tilde{f}_\tau = a\tilde{f}_\tau$ where a is some complex constant. We applied zero padding to the hologram (resulting in a 2048×2048 input image) to ensure a clear spatial separation of the three reconstructed
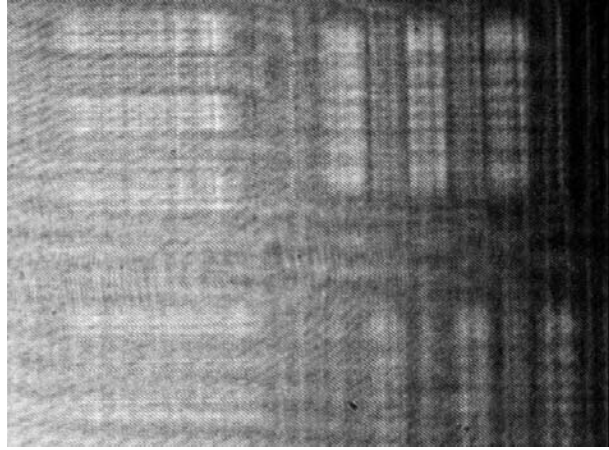
Fig. 2.7. Measured hologram. There are 776×572 samples. The sampling step is 10μm. (Data courtesy of T. Colomb, F. Montfort and Ch. Depeursinge, IOA/EPFL)
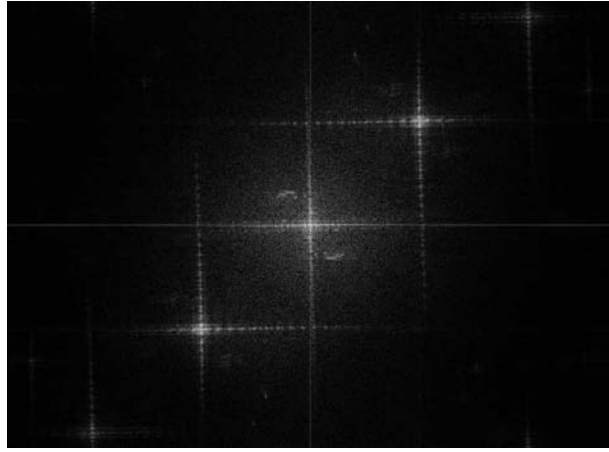
Fig. 2.8. Absolute value of the Fourier transform of the hologram. The frequency origin is in the center.

terms.

We then applied our Fresnelet transform to this (de-)modulated hologram $R'I$. The reconstruction distance d was adjusted to 35 cm resulting in the proper parameter $\tau = \sqrt{\lambda d}$. In Fig. 2.9 we show the Fresnelet coefficients corresponding to the inner products of $R'I$ with the tensor product basis functions

$$\tilde{\psi}^n_{\tau/2^j}(x/2^j)\tilde{\beta}^n_{\tau/2^j}(y/2^j),$$
$$\tilde{\psi}^n_{\tau/2^j}(x/2^j)\tilde{\psi}^n_{\tau/2^j}(y/2^j),$$
$$\tilde{\beta}^n_{\tau/2^j}(x/2^j)\tilde{\psi}^n_{\tau/2^j}(y/2^j),$$
$$\text{and} \quad \tilde{\beta}^n_{\tau/2^J}(x/2^J).\tilde{\beta}^n_{\tau/2^J}(y/2^J)$$

for $n = 3$, $j = 0, \ldots, J$ and $J = 4$. These coefficients are complex and we are only showing their modulus. From these coefficients we could

0000110000
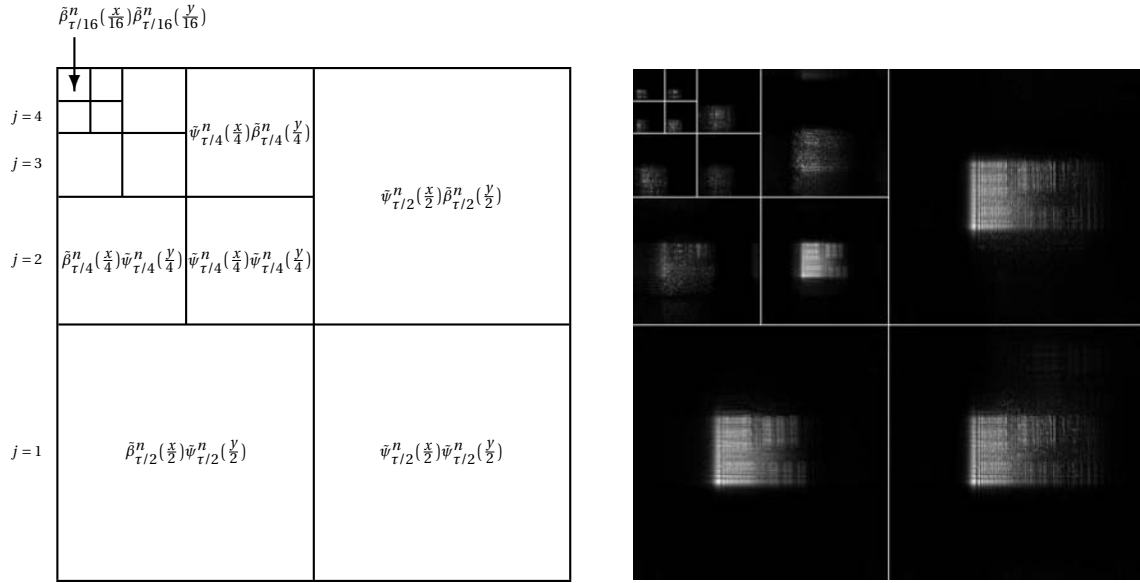
Fig. 2.9. Fresnelet transform of the modulated hologram $R'I$ (coefficient's amplitude). There are 2048×2048 coefficients.

recover the reconstructed signal (amplitude and phase) at any dyadic scale as it is shown in the pyramids of Fig. 2.10. It is important to remember that all the information to get a finer scale from the coarsest scale (top left) is contained in the subbands of the Fresnelet transform of Fig. 2.9.

The experiment shows that the three hologram terms are spatially separated in the reconstruction: the zero-order term in the center, the image below left and the twin image up right (not visible). One can also notice how the zero-order term vanishes as the reconstruction scale gets coarser. This is visible in both the pyramid (Fig. 2.10) where more and more energy goes into the image term as the image gets coarser, and in the Fresnelet transform (Fig. 2.9) where the zero-order term coefficient's energy is mainly in the highpass subbands. The explanation for this behavior is the following. As mentioned earlier, the hologram's energy is concentrated around the three frequencies $(-k_x, -k_y)$, $(0,0)$, and (k_x, k_y), corresponding respectively to the image, the zero-order, and the twin image. When we multiply the hologram by $R'(x, y) \approx R(x, y) = e^{i(k_x x + k_y y)}$, the different terms are shifted by (k_x, k_y) in frequency and their new respective locations are $(0,0)$, (k_x, k_y) and $(2k_x, 2k_y)$. As the energy corresponding to the zero order and twin image terms is shifted to high frequencies, it is mainly encoded in the fine scale (highpass) Fresnelet coefficients. Coarse scale reconstructions (which discard the high frequency information) will therefore essentially suppress the zero order or twin image terms, which is a nice feature of our algorithm.
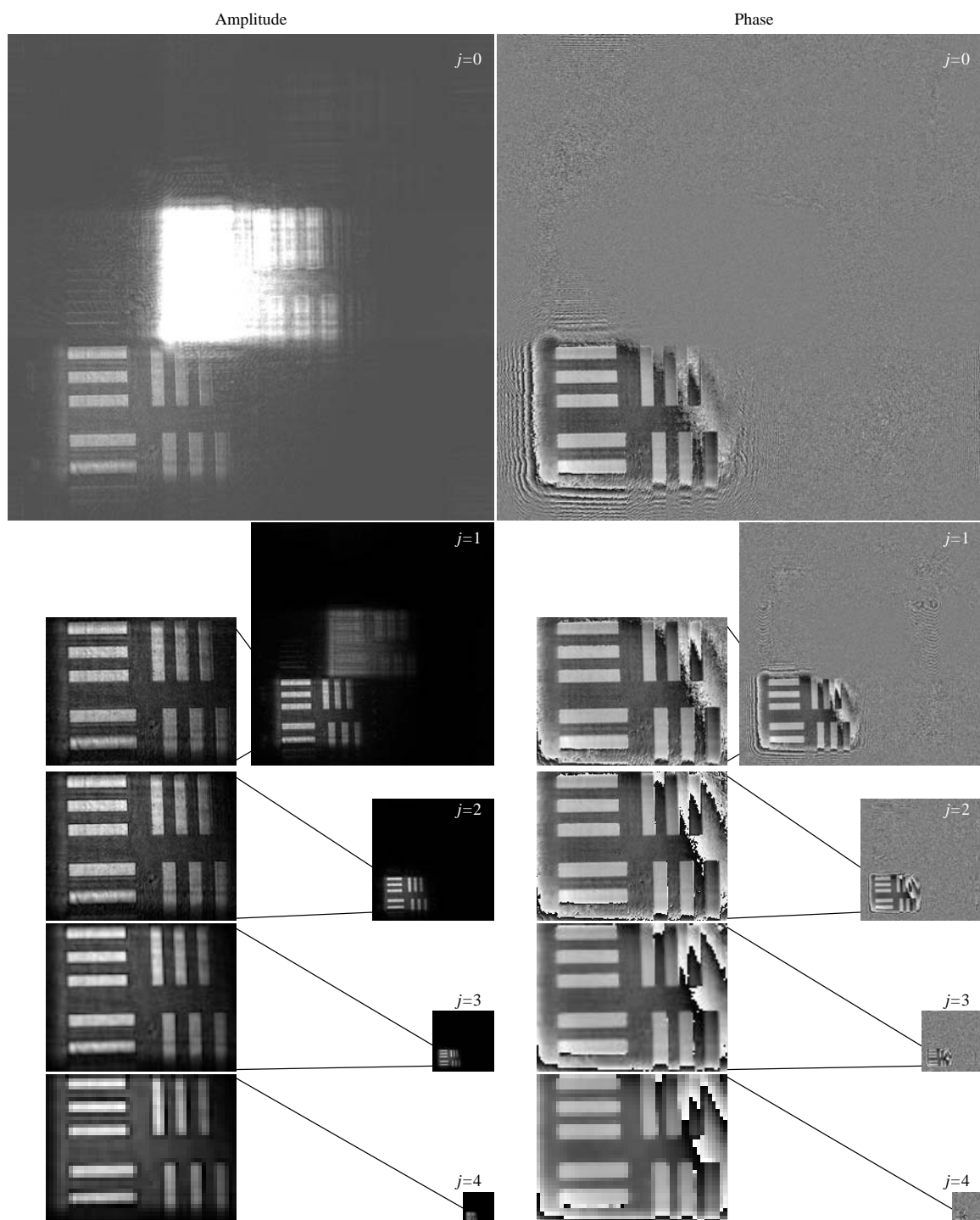
Fig. 2.10. Reconstructed amplitude and phase from the Fresnelet coefficients in Fig. 2.9 for $j = 0, 1, 2, 3, 4$. The contrast was stretched for each image to the full grayscale range, except for the amplitude at $j = 0$. At the finest scale ($j = 0$) the size of the images is 2048 × 2048.

2.7 Discussion

We have seen that the wavefronts reconstructed with the Fresnelet transform from the simulated data agree with the theoretical gold standard and that the algorithm can be applied successfully to reconstruct real-world holographic data as well. Although ringing artifacts may be distinguished at fine scales, they tend to disappear as the scale gets coarser.

The presented method differs from the traditional reconstruction algorithms used in digital holography which implement an inverse Fresnel transform of the data. The Fresnel transform algorithms fall into two main classes [108]. The first approach [Fig. 2.11(a)], as described in [108], uses the convolution relation (2.1). It is implemented in the Fourier domain and needs two FFTs. The transformed function's sampling step T' is the same as that of the original function. The three terms—the image, the twin image (that is suppressed at all scales in the Fresnelet algorithm) and the zero-order)—are visible in Fig. 2.11(a). The second method [Fig. 2.11(b)] uses the link with the Fourier transform (2.17) [36, 108]. We call this implementation a Chirp-Fourier Fresnel transform (ChFFrT) (See Chapter 6). The discretization of this relation requires only one FFT. As this method relies on the special interpretation of the spatial frequency variable as a rescaled space variable, the sampling step of the transformed function is $T' = \lambda d / (NT)$ where N is the number of samples in one direction. Therefore it depends on the distance, the wavelength and the number of measured samples. In particular if the number of samples in the x and y directions are not the same, e.g., in Fig. 2.11(b), the corresponding sampling steps do not agree. In the work of Cuche *et al.* [36], the parameters are set such that the reconstruction is at approximately one fourth the scale of the digitized hologram.

The first advantage of our approach is that it allows us to choose the sampling step on the reconstruction side. It can be any multiple $T' = mT$ for $m = 1, 2, 4, 8, \ldots$ The computational cost of our algorithm is the same as that of a filtering in the Fourier domain; i.e., roughly the cost of two FFTs.

Also, as our method is based on the computation of inner products, it leaves more freedom for treating boundary conditions. One possibility to reduce the influence of the finite support of the CCD camera is to use weighted, or renormalized inner products.

More than just a Fresnel transform, our Fresnelet transform provides us with wavelet coefficients. A remarkable feature is that the energy of the unwanted zero-order and twin images is concentrated within the fine scale subbands. This opens up new perspectives for their selective suppression (see Chapter 3) in the wavelet domain as an alternative to other proposed algorithms ([38, 106]). In addition,
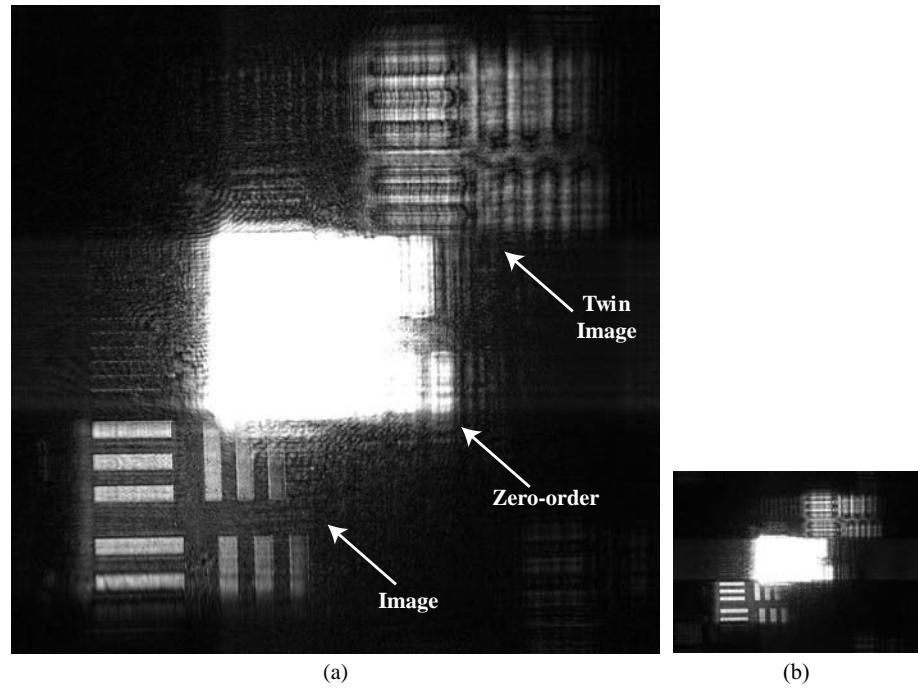
Fig. 2.11. Reconstructed amplitudes from the hologram of Fig. 2.7 using alternative methods based on the discretization of (a) the convolution relation (2.1) and (b) the Fourier formulation (2.17) of the Fresnel transform. For (a), the hologram was padded with zeros to a size of 2048×2048 and the sampling step is $T' = T = 10\,\mu$m. For the reconstruction in (b) the 776×572 hologram was fed directly into the algorithm resulting in different sampling steps in the x and y directions: $T_x' = \lambda d/(N_x T) = 28.54\,\mu$m and $T_y' = \lambda d/(N_y T) = 38.72\,\mu$m.

it allows us to apply simple wavelet-domain thresholding techniques to reduce the measurement noise in the reconstructed images.

2.8 Conclusion

We have constructed a new wavelet basis for the processing and reconstruction of digital holograms by taking advantage of the mathematical properties of the Fresnel transform. We have motivated our choice of B-splines as elementary building blocks based on a new uncertainty relation.

We have demonstrated that the method works and that it is applicable to the reconstruction of real data. Our method offers several advantages: it allows to reconstruct at different user-specified and wavelength independent scales. Furthermore, reconstructions at coarse scale allow for optimal filtering of the zero-order and the twin image and also result in less noisy images.

0000110100

2.A Proof of Theorem 1

Proof: We first recall the Heisenberg uncertainty relation for the Fourier transform. Let $f \in L_2(\mathbb{R})$. We have following inequality:

$$\sigma_f^2 \sigma_{\hat{f}}^2 \geq \frac{1}{16\pi^2}. \tag{2.39}$$

This inequality is an equality if and only if there exist t_0, ω_0, b real and a complex amplitude a such that:

$$f(t) = a \, e^{i\omega_0 t} \, e^{-b(t-t_0)^2}. \tag{2.40}$$

Let $f(x) = e^{i\pi(x/\tau)^2} g(x)$. We start by noting that f and g have the same norm:

$$\|f\|^2 = \int_{-\infty}^{\infty} \left| e^{i\pi(x/\tau)^2} g(x) \right|^2 \mathrm{d}x = \int_{-\infty}^{\infty} |g(x)|^2 \mathrm{d}x = \|g\|^2,$$

the same mean:

$$\mu_f = \frac{1}{\|f\|^2} \int_{-\infty}^{\infty} x \left| e^{i\pi(x/\tau)^2} g(x) \right|^2 \mathrm{d}x$$

$$= \frac{1}{\|g\|^2} \int_{-\infty}^{\infty} x |g(x)|^2 \mathrm{d}x = \mu_g,$$

and finally the same variances:

$$\sigma_g^2 = \frac{1}{\|g\|^2} \int_{-\infty}^{\infty} (x - \mu_g)^2 |g(x)|^2 \mathrm{d}x$$

$$= \frac{1}{\|g\|^2} \int_{-\infty}^{\infty} (x - \mu_g)^2 \left| e^{i\pi(x/\tau)^2} f(x) \right|^2 \mathrm{d}x$$

$$= \frac{1}{\|f\|^2} \int_{-\infty}^{\infty} (x - \mu_f)^2 |f(x)|^2 \mathrm{d}x$$

$$= \sigma_f^2.$$

Also, g and $\tilde{g}_\tau$ have the same means. Without loss of generality, we will from now on consider that f and g have unit norm $\|f\| = \|g\| = 1$ and that they have zero mean $\mu_f = \mu_g = 0$. Using the link between the Fresnel and Fourier transforms (2.17), we compute the variance of $\tilde{g}$:

$$\sigma_{\tilde{g}_\tau}^2 = \int_{-\infty}^{\infty} x^2 |\tilde{g}_\tau(x)|^2 \mathrm{d}x$$

$$= \int_{-\infty}^{\infty} x^2 \left| \frac{1}{\tau} e^{2i\pi(x/\tau)^2} \hat{f}\left(\frac{x}{\tau^2}\right) \right|^2 \mathrm{d}x$$

$$= \tau^4 \int_{-\infty}^{\infty} v^2 |\hat{f}(v)|^2 \mathrm{d}v$$

$$= \tau^4 \sigma_{\hat{f}}^2.$$

The product of the variances becomes:

$$\sigma_g^2 \sigma_{\tilde{g}_\tau}^2 = \tau^4 \sigma_f^2 \sigma_{\hat{f}}^2 \geq \frac{\tau^4}{16\pi^2}.$$

From the Heisenberg uncertainty relation, we know that this inequality is an equality if and only if there exist x_0, ω_0, b real and a complex amplitude a such that:

$$g(x) = a \, e^{i\omega_0 x} \, e^{-b(x-x_0)^2} \, e^{-i\pi(x/\tau)^2}.$$

To prove the second part of the statement, we compute the variance of the transformed function explicitly:

$$\begin{aligned}
\sigma_{\tilde{g}_\tau}^2 &= \frac{1}{\tau^2} \int_{-\infty}^{\infty} x^2 \left| \hat{f}\left(\frac{x}{\tau^2}\right) \right|^2 \, dx \\
&= \tau^4 \int_{-\infty}^{\infty} x^2 |\hat{f}(x)|^2 \, dx \\
&= \frac{\tau^4}{4\pi^2} \int_{-\infty}^{\infty} |f(x)'|^2 \, dx \\
&= \frac{\tau^4}{4\pi^2} \int_{-\infty}^{\infty} \left| g(x)' + \frac{2i\pi x}{\tau^2} g(x) \right|^2 \, dx.
\end{aligned}$$

If $g(x)$ is real valued, there are no cross terms in the modulus. Thus, we get:

$$\begin{aligned}
\sigma_{\tilde{g}_\tau}^2 &= \tau^4 \int_{-\infty}^{\infty} |\nu \hat{g}(\nu)|^2 \, d\nu + \int_{-\infty}^{\infty} |x g(x)|^2 \, dx \\
&= \tau^4 \sigma_{\hat{g}}^2 + \sigma_g^2
\end{aligned}$$

and finally:

$$\sigma_{\tilde{g}_\tau}^2 \sigma_g^2 = \tau^4 \sigma_{\hat{g}}^2 \sigma_g^2 + \sigma_g^4 \geq \frac{\tau^4}{16\pi^2} + \sigma_g^4$$

which is an equality if and only if there exist x_0, a, b real, such that:

$$g(x) = a \, e^{-b(x-x_0)^2}.$$

To derive the lower bound on the variance $\sigma_{\tilde{g}_\tau}^2$ we rewrite (2.20) as:

$$\sigma_{\tilde{g}_\tau}^2 \geq \frac{\tau^4}{16\pi^2} \frac{1}{\sigma_g^2} + \sigma_g^2.$$

The right-hand side is minimal for $\sigma_g^2 = \tau^2/(4\pi)$ and therefore:

$$\sigma_{\tilde{g}_\tau}^2 \geq \frac{\tau^2}{2\pi}.$$

$\square$

0000110110

2.B   Proof of Theorem 2

Proof: $u_{n,\tau}(x)$ satisfies, for $n \geq 1$:

$$
\begin{aligned}
u'_{n,\tau}(x) &= \frac{\mathrm{d}}{\mathrm{d}x} \int_0^x \frac{(x-\xi)^n}{n!} k_\tau(\xi)\,\mathrm{d}\xi \\
&= \int_0^x \frac{(x-\xi)^{n-1}}{(n-1)!} k_\tau(\xi)\,\mathrm{d}\xi \\
&= u_{n-1,\tau}(x)
\end{aligned}
$$

and for $n = 0$:

$$
u'_{0,\tau}(x) = k_\tau(x).
$$

Therefore, by differentiating $u_{n,\tau}$ $(n+1)$ times, we hit the kernel of the Fresnel Transform operator:

$$
u_{n,\tau}^{(n+1)}(x) = k_\tau(x).
$$

We can now calculate the Fresnel transform of a B-spline of degree n:

$$
\begin{aligned}
\tilde{\beta}_\tau^n(x) &= (\beta^n * k_\tau)(x) \\
&= \left(\beta^n * u_{n,\tau}^{(n+1)}\right)(x).
\end{aligned}
$$

As differentiation and convolution commute, we have:

$$
\begin{aligned}
\tilde{\beta}_\tau^n(x) &= \left(\frac{\mathrm{d}^{n+1}}{\mathrm{d}x^{n+1}}\beta^n\right) * u_{n,\tau}(x) \\
&= \left(\sum_{k=0}^{n+1}(-1)^k \binom{n+1}{k}\delta(x-k)\right) * u_{n,\tau}(x) \\
&= \sum_{k=0}^{n+1}(-1)^k \binom{n+1}{k} u_{n,\tau}(x-k).
\end{aligned}
$$

$\square$

2.C Proof of Theorem 3

Proof: We integrate (2.30) by parts, using $(\mathrm{d}/\mathrm{d}x)\,k_\tau(x) = (2i\pi x/\tau^2)\,k_\tau(x)$:

$$
\begin{aligned}
u_{n,\tau}(x) &= \int_0^x \frac{(x-\xi)^n}{n!}\, k_\tau(\xi)\,\mathrm{d}\xi \\
&= \left[-\frac{(x-\xi)^{n+1}}{(n+1)!}\, k_\tau(\xi) \right]_0^x \\
&\quad - \int_0^x -\frac{(x-\xi)^{n+1}}{(n+1)!}\, \frac{2i\pi\xi}{\tau^2}\, k_\tau(\xi)\,\mathrm{d}\xi \\
&= \frac{x^{n+1}}{\tau(n+1)!} - \frac{2i\pi}{\tau^2} \\
&\quad \times \left(\int_0^x \frac{(x-\xi)^{n+2}}{(n+1)!}\, k_\tau(\xi)\,\mathrm{d}\xi \right. \\
&\qquad\qquad \left. -x \int_0^x \frac{(x-\xi)^{n+1}}{(n+1)!}\, k_\tau(\xi)\,\mathrm{d}\xi \right) \\
&= \frac{x^{n+1}}{\tau(n+1)!} \\
&\quad - \frac{2i\pi}{\tau^2}\big((n+2)\, u_{n+2,\tau}(x) - x\, u_{n+1,\tau}(x) \big)
\end{aligned}
$$

which we rewrite under the form (2.31). The expressions for $u_{0,\tau}(x)$ and $u_{1,\tau}(x)$ follow immediately from the general definitions of $u_{n,\tau}$, the Fresnel integrals and the recursion formula (2.31). □

2.D Proof of Theorem 4

Proof: We begin by computing the Fresnel transform of a B-spline that is multiplied by x:

$$
\begin{aligned}
(x\beta^n)^{\sim}_\tau(x) &= \int_{-\infty}^{\infty} (x-\xi)\beta^n(x-\xi)\, k_\tau(\xi)\,\mathrm{d}\xi \\
&= x\tilde\beta^n_\tau(x) - \int_{-\infty}^{\infty} \frac{\tau^2}{2i\pi}\beta^n(x-\xi)\, \frac{\mathrm{d}}{\mathrm{d}x} k_\tau(\xi)\,\mathrm{d}\xi \\
&= x\tilde\beta^n_\tau(x) - \frac{\tau^2}{2i\pi}\left(\frac{\mathrm{d}}{\mathrm{d}x}\beta^n(x) \right)^{\sim}_\tau.
\end{aligned}
$$

We can now use the B-spline's differentiation formula [213]:

$$
\frac{\mathrm{d}}{\mathrm{d}x}\beta^n(x) = \beta^{n-1}(x) - \beta^{n-1}(x-1) = \Delta\beta^{n-1}(x)
$$

to get:

$$
(x\beta^n)^{\sim}_\tau(x) = x\tilde\beta^n_\tau(x) - \frac{\tau^2}{2i\pi}\Delta\tilde\beta^{n-1}_\tau(x).
$$

0000111000

We rewrite (2.32) as:

$$\beta^n(x) = \frac{1}{n}\Delta(x\beta^{n-1}(x)) + \beta^{n-1}(x-1)$$

to finally get its Fresnel transform:

$$
\begin{aligned}
\tilde{\beta}_\tau^n(x) &= \frac{1}{n}\Delta\left(x\tilde{\beta}_\tau^{n-1}(x) - \frac{\tau^2}{2i\pi}\Delta\tilde{\beta}_\tau^{n-2}(x)\right) \\
&\quad + \tilde{\beta}_\tau^{n-1}(x-1) \\
&= \frac{x\tilde{\beta}_\tau^{n-1}(x) + (n+1-x)\tilde{\beta}_\tau^{n-1}(x-1)}{n} \\
&\quad + \frac{i\tau^2}{2\pi n}\Delta^2\tilde{\beta}_\tau^{n-2}(x).
\end{aligned}
\tag{2.41}
$$

$\square$

Chapter 3

Nonlinear Fresnelet Approximations for Interference-Term Suppression

Abstract[a]— We present a zero-order term and twin image elimination algorithm for digital Fresnel holograms that were acquired in an off-axis geometry. These interference terms arise when the digital hologram is reconstructed and corrupt the result. Our algorithm is based on the Fresnelet transform, a waveletlike transform that uses basis functions tailor-made for digital holography. We show that in the Fresnelet domain, the coefficients associated to the interference terms are separated both spatially and with respect to the frequency bands. We propose a method to suppress them by selectively thresholding the Fresnelet coefficients. Unlike other methods that operate in the Fourier domain and affect the whole spacial domain, our method operates locally in both space and frequency, allowing for a more targeted processing.

---

[a]This chapter is based on Ref. [128].

3.1   Introduction

The hologram is a measure of the intensity that results from the object wave's interference with a reference wave. In the so-called off-axis geometry, the reference wave and object wave travel in slightly different directions thus giving rise to interference fringes. During optical reconstruction, the object wave may be reproduced by illuminating the chemically processed hologram with a reconstruction beam. The latter is diffracted. Three diffraction orders may be distinguished: the $+1$ order which is an exact replica of the object wave, the undiffracted zero-order term, and the -1 order term.

In digital holography [36, 73, 109], the photographic plate is replaced by a CCD camera. The hologram is stored in the computer as a digital image and the reconstruction process is carried out by simulating the physical diffraction phenomenon. Since wave propagation can be modeled with good accuracy in the Fresnel regime by the Fresnel transform, it can be easily implemented. However, since digital recording media have a lower resolution than those used in classical holography, the fringes' spacing must be larger to be resolved. This means that the reference beam's angle cannot be as high. As a conse-

quence, the three diffracted waves do, at least partially, overlap during reconstruction.

So far, only algorithms have been proposed that either filter the relevant information in the Frequency domain [38, 106, 133], or, that take advantage of the spatial separation of the different orders after propagation. However, neither approach is completely satisfactory, since either the reconstructed wave's bandwidth or its field of view are drastically limited. Here, we derive a nonlinear signal approximation algorithm that takes advantage of the interference-terms' separation in both frequency and space. To this end, we make use of the family of shift invariant, multiresolution basis functions that we proposed in Chapter 2 (see also [127]), namely Fresnelets.

The chapter is organized as follows: In Section 3.2, we review the Fresnel transform and holography. In Section 3.3, we briefly describe Fresnelets. In Section 3.4 we propose our new approximation algorithm which we finally illustrate and test on simulation examples in Section 3.5.

3.2 Fresnel Transform and Holography

3.2.1 Fresnel Transform

Three fundamental properties of the Fresnel transform are of particular interest to us, since they give a direct insight on how well the diffraction terms are separated in either space or frequency. First, a modulated signal undergoes a shift after the transform. Let $f \in L_2(\mathbb{R})$ and $g(x) = \exp(2i\pi\nu_0 x)f(x + \nu_0\tau^2/2)$ be a modulated version of the function. Then its Fresnel transform with parameter τ, is

$$\tilde{g}_\tau(x) = \exp(-i\pi\nu_0^2\tau^2)\exp(2i\pi\nu_0 x)\tilde{f}_\tau\left(x - \frac{\nu_0\tau^2}{2}\right). \qquad (3.1)$$

Second, the Fresnel transform is a unitary convolution operator and, as such, the spectrum of the transformed signal remains unchanged. This property may be recognized immediately from the Fresnel operator's frequency response

$$\hat{k}_\tau(\nu) = e^{i\pi/4}\exp(-i\pi(\tau\nu)^2) \qquad (3.2)$$

where $\left|\hat{k}_\tau(\nu)\right| = 1$ implies the spectrum invariance

$$\left|\hat{f}(\nu)\right|^2 = \left|\hat{\tilde{f}}_\tau(\nu)\right|^2 \qquad \forall\tau \in \mathbb{R}_+. \qquad (3.3)$$

Last, localized features spread out during the propagation process and obey a Heisenberg-like uncertainty principle [127]. The latter

0000111100

gives a lower bound to the product of a function's variance and that of its transform

$$\sigma_f^2 \sigma_{\tilde{f}_\tau}^2 \geq \frac{\tau^4}{16\pi^2}.$$ (3.4)

For real functions there is also a lower bound on $\sigma_{\tilde{f}_\tau}^2 \geq \tau^2/2\pi$, that is independent of f.

3.2.2 Holography

Information in the hologram plane

The hologram measured with the CCD camera, $I(\mathbf{x}) \in \mathbb{R}_+$ results from the interference, at every location $\mathbf{x} = (x, y)$, of the object wave $\Psi(\mathbf{x}) \in \mathbb{C}$ with a plane reference wave $R(\mathbf{x}) = A(\mathbf{x})\exp\big(i(k_x x + k_y y)\big)$ (where $\mathbf{k}_\lambda = (k_x, k_y, k_z)$ is the wave vector)

$$I(\mathbf{x}) = |\Psi(\mathbf{x}) + R(\mathbf{x})|^2.$$ (3.5)

This equation may be expanded to identify the three interference terms

$$I(\mathbf{x}) = \underbrace{|R(\mathbf{x})|^2 + |\Psi(\mathbf{x})|^2}_{\text{zero-order}} + \underbrace{R^*(\mathbf{x})\Psi(\mathbf{x})}_{+1\ \text{order}} + \underbrace{R(\mathbf{x})\Psi^*(\mathbf{x})}_{-1\ \text{order}}.$$ (3.6)

In the hologram plane, they overlap completely.

Plane wave diffraction by a hologram

To reconstruct the object wavefront, we apply a Fresnel transform to the hologram (which is equivalent to physically illuminating the hologram with a plane wave that travels perpendicularly to the hologram). As the propagation distance grows, the unmodulated zero-order stays located in the central part of the image, while the ±1 orders move away from the center according to property (3.1) (see Fig. 3.1). The higher the modulation frequency (or equivalently, the angle between the reference and the object wave), the larger the separation. Because the acquisition device's sampling step remains large, the modulation frequency is limited, as well as the angle between the object and the reference wave. Therefore, the spatial separation between the different orders is limited and they do, at least partially, overlap.

Moreover, the uncertainty relation on the Fresnel transform implies a broadening of the zero and −1 orders as the distance increases (see Fig. 3.2). In contrast, the +1 order's support first shrinks until the original image-hologram distance is reached and starts broadening again for larger distances.

Fresnel Transform

Spectrum
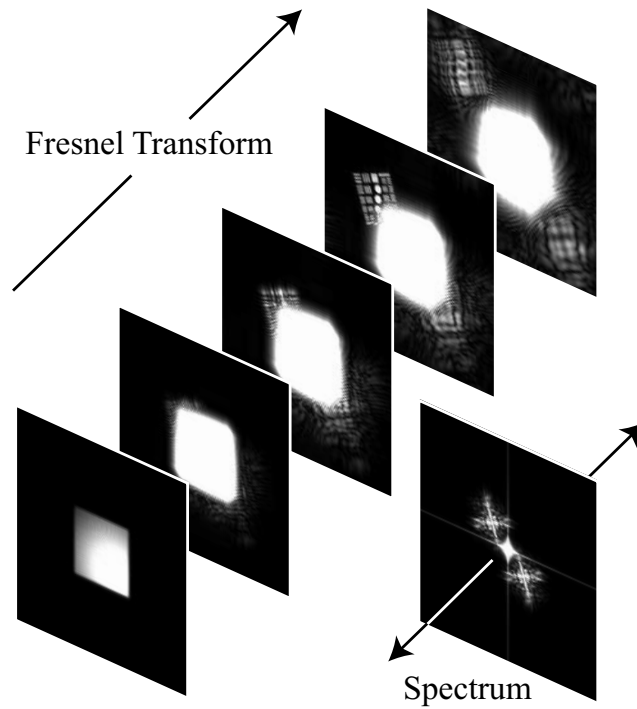
Fig. 3.1. Information repartition in the diffracted wave. Each depth has an associated shift invariant, multiresolution Fresnelet basis. For the in-focus distance, the associated wavelet basis is a standard wavelet basis.

Frequency content

The three terms have their energy clearly separated in the frequency domain and located around their respective modulation frequency. This property was recognized early on to be of use in digital holography, since several algorithms that keep only the relevant frequency information (+ 1 order) and discard the rest via a bandpass filtering procedure have been proposed. Their implementation can be carried out in either the spatial [106, 133] or frequency domain [38]. All these filtering procedures are linear. However, since they limit the spectral content of the image to reconstruct, details are lost. Moreover, since such filtering procedures are nonlocal, the whole field of view is affected.

Interestingly, property (3.3) implies that the diffracted-wave's spectrum at any distance from the hologram remains unchanged (see Fig. 3.1). This means, that the filtering may be equivalently performed at any distance.

3.3 Fresnelets

Fresnelet bases are wavelet bases that have undergone a Fresnel transform. We focus on Fresnelets associated with B-spline wavelets, since
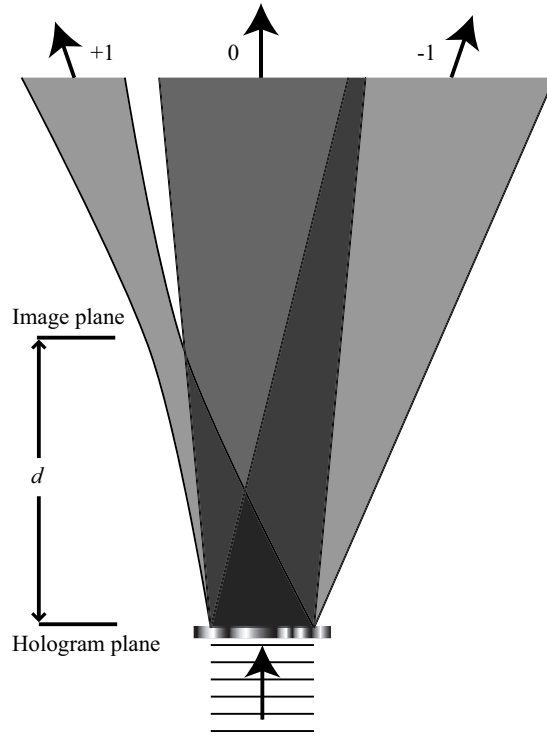
Fig. 3.2.   Support broadening of the wave diffracted by an off-axis Fresnel holo-gram.

their expression may be derived in both frequency and space [127]. They have many desirable properties required for the digital process-ing of holograms: for example, they tend to be optimal with respect to the spatial energy spreading as they can be shown to converge to Gabor functions [127]. The construction is based on the definition of the Fresnel spline, or F-spline of degree $n \in \mathbb{N}$ and parameter $\tau \in \mathbb{R}_+$, denoted $\tilde{\beta}_\tau^n(x)$, that is the Fresnel transform with parameter τ of a B-spline $\beta^n(x)$ of degree n

$$\tilde{\beta}_\tau^n(x) = (\beta^n * k_\tau)(x).$$

The generating functions are then constructed as linear combinations of F-splines

$$\tilde{\psi}_{\tau/2}^n\left(\frac{x}{2}\right) = \sum_k g(k)\tilde{\beta}_\tau^n(x - k)$$

and are entirely specified from the sequence $g(k)$. They correspond to the general family of semi-orthogonal spline wavelets of the form

$$\psi^n\left(\frac{x}{2}\right) = \sum_k g(k)\beta^n(x - k). \tag{3.7}$$

The transformed basis functions are shift-invariant on a level-by-level basis but their multiresolution properties are governed by the special form that the dilation operator takes in the Fresnel domain. In our

case, given that the wavelength is fixed, the parameter $\tau = \sqrt{\lambda d}$ only depends on the depth d of the propagation. For each depth there is an associated basis.

From now on, we only consider orthonormal Fresnelet bases of $L_2(\mathbb{R}^2)$, denoted

$$\left\{\tilde{\psi}^n_{\tau,j,\mathbf{m},p}\right\}_{j\in\mathbb{Z},\mathbf{m}\in\mathbb{Z}^2,p=1,2,3}, \quad \tilde{\psi}^n_{\tau,j,\mathbf{m},p}(\mathbf{x}) = \frac{1}{\sqrt{2^j}}\tilde{\psi}^n_{\tau/2^j,p}\left(\frac{\mathbf{x}}{2^j} - \mathbf{m}\right). \quad (3.8)$$

These may be constructed for example from the separable orthonormal wavelet basis of $L_2(\mathbf{R}^2)$

$$\left\{\psi^n_{j,\mathbf{m},1}(\mathbf{x}), \psi^n_{j,\mathbf{m},2}(\mathbf{x}), \psi^n_{j,\mathbf{m},3}(\mathbf{x})\right\}_{j\in\mathbb{Z},m\in\mathbb{Z}^2} \quad (3.9)$$

where the two-dimensional wavelets

$$\psi^n_{j,\mathbf{m},p}(\mathbf{x}) = \frac{1}{2^j}\psi^n_p\left(\frac{\mathbf{x}}{2^j} - \mathbf{m}\right) \quad (3.10)$$

are separable products of the Battle-Lemarié scaling function $\phi^n(x)$ and wavelet $\psi^n(x)$ of degree n [8, 124]:

$$\psi^n_1(\mathbf{x}) = \phi^n(x)\psi^n(y), \psi^n_2(\mathbf{x}) = \psi^n(x)\phi^n(y), \psi^n_3(\mathbf{x}) = \psi^n(x)\psi^n(y). \quad (3.11)$$

We introduce the condensed notation $\mathbf{k} = (p, j, \mathbf{m}) \in \{1,2,3\} \times \mathbb{Z} \times \mathbb{Z}^2$

For a given setup, a single set of coefficients may be used to generate the diffracted wave at any depth, simply by replacing the basis functions in the expansion

$$\tilde{f}_\tau(\mathbf{x}) = \sum_{\mathbf{k}} c_{\mathbf{k}}\tilde{\psi}^n_{\tau,\mathbf{k}}(\mathbf{x}) \quad (3.12)$$

with those associated to a different depth. In our case, the diffracting wave in the hologram plane is given by $I(\mathbf{x})$, the coefficients are obtained by computing the inner products

$$c_{\mathbf{k}} = \langle I, \tilde{\psi}^n_{\tau,\mathbf{k}}\rangle. \quad (3.13)$$

3.4 Algorithm

We now propose an algorithm that selectively suppresses the Fresnelet coefficients in order to keep only coefficient whose energy is mainly related to the $+1$ order. It is a fully automatic two-step process. First, we suppress the zero-order and second, the -1 order.

0001000000
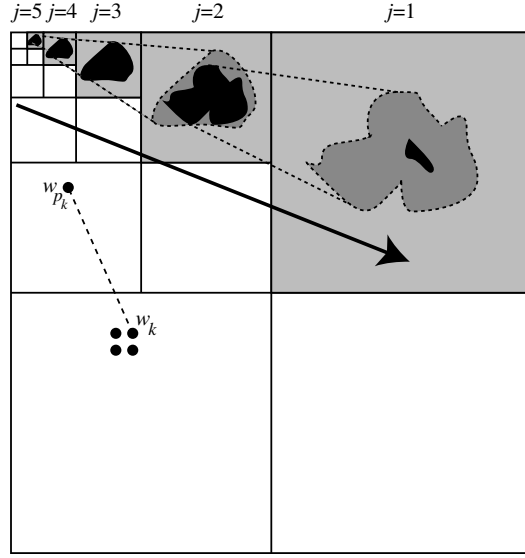
Fig. 3.3. Schematic representation of the hierarchical thresholding algorithm.

Zero-order term suppression

The first step consists in the computation of the hologram's Fresnelets coefficients (3.13), where the parameter $\tau = \sqrt{\lambda d}$ must be adjusted properly. This not only yields a decomposition of the information in several frequency bands, but also in terms of their spatial distribution within the frequency bands. The energy that is associated to the (unmodulated) zero-order is mainly concentrated at low frequencies. The algorithm proceeds from coarse to fine: a threshold value t_j is associated to every frequency band j. The parent coefficient of $c_{\mathbf{k}}$ is denoted $c_{\mathbf{p_k}}$ (Fig. 3.3). The new coefficients $c'_{\mathbf{k}}$ are computed at the coarsest scale $j = J$ as

$$c'_{\mathbf{k}} = \begin{cases} c_{\mathbf{k}} & \text{if } |c_{\mathbf{k}}| < t_J \\ 0 & \text{if } |c_{\mathbf{k}}| \geq t_J \end{cases} \tag{3.14}$$

and for the finer scales $j < J$

$$c'_{\mathbf{k}} = \begin{cases} c_{\mathbf{k}} & \text{if } |c_{\mathbf{k}}| < t_j \\ 0 & \text{if } |c_{\mathbf{k}}| \geq t_j \text{ and } |c_{\mathbf{p_k}}| \geq t_{j+1}. \end{cases} \tag{3.15}$$

Unlike denoising algorithms that set low energy coefficients to zero, our method eliminates high energy coefficients. The test on the parent coefficient ensures that high frequency coefficients are only removed in regions that are corrupted by the zero-order. The signal is reconstructed with Fresnelets of parameter $\tau = 0$ which yield a reconstruction with the real image (+ 1 order) at proper focus and the zero-order suppressed.
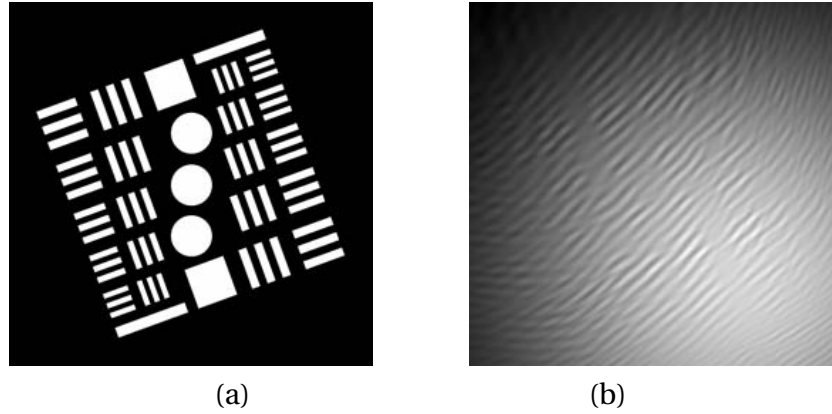
Fig. 3.4. (a) Amplitude of test target. (256×256 pixels, $T = 10\mu$m, $d = 0.25$m, $\lambda = 632.8$nm) (b) simulated hologram

Minus 1 order term suppression

Since in the Fresnelet domain, information located around a particular frequency cannot be distinguished from that lying around the opposite sign frequency, and since the $+1$ and -1 order are indeed located at opposite frequencies, a second step is required to suppress the -1 order. We start by a pointwise multiplication of the wave obtained in the first step, with a digital wave of the form

$$R^*(\mathbf{x}) = \exp\big(-i(k_x x + k_y y)\big),$$

the complex conjugate of the reference wave. This modulation shifts the frequencies such that the -1 order is located around the frequency origin. We then apply a Fresnelet transform with parameter $\tau = 0$ before going through the same thresholding scheme as in the first step, but with new thresholding values. After inverse transforming the coefficients and (de)modulating the result using a digital wave of the form $R'(\mathbf{x}) = \exp\big(2i(k_x x + k_y y)\big)$, we obtain a reconstruction that is free of interference terms.

3.5 Results

A hologram was obtained by simulating the propagation of the wave reflected by a test target using a procedure described in Subsection 2.6.1 (See also [127]). We have chosen the following values for the various parameters: $T = 10\mu$m (camera's sampling step), $d = 0.25$ m (object-camera distance), $\lambda = 632.8$ nm (light wavelength). The angle between the reference wave vector and the normal to the CCD plane was set to 0.45°. The reference wave's intensity profile is Gaussian. The test target and the simulated hologram are shown in Fig. 3.4.
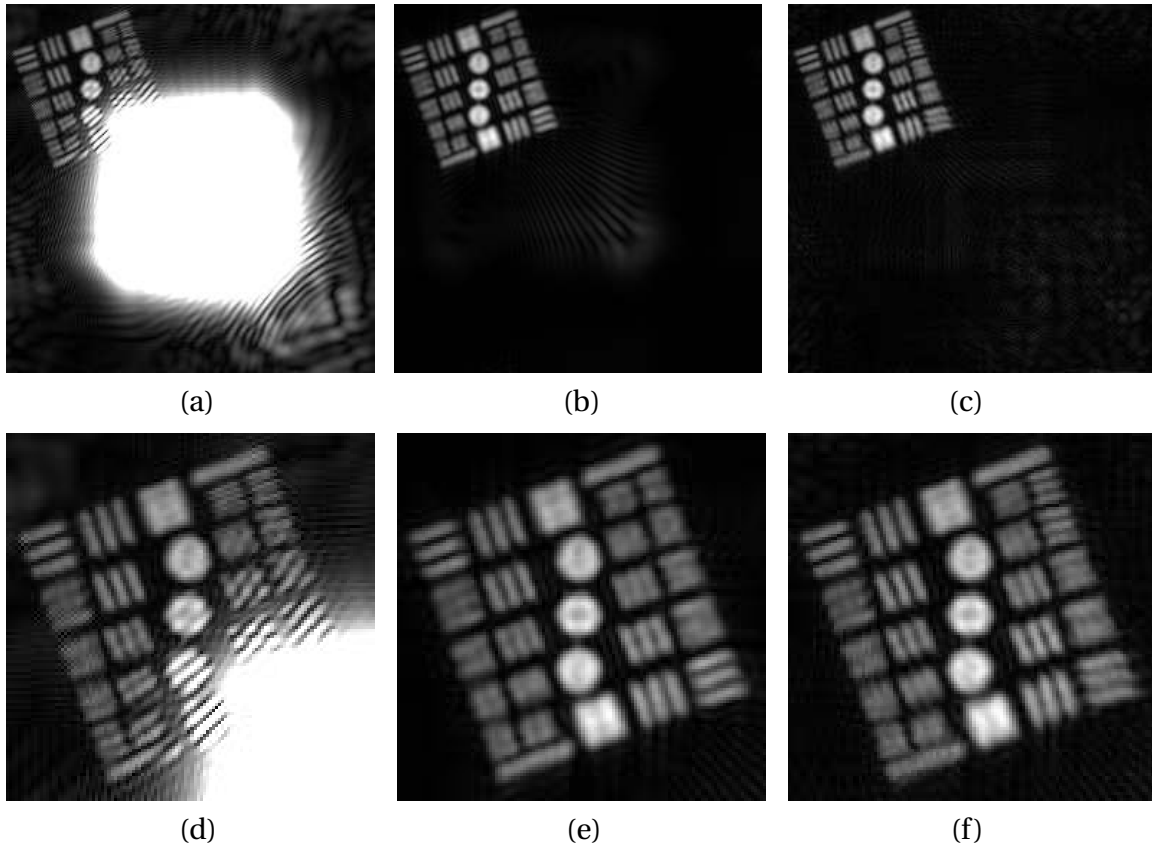
Fig. 3.5. Reconstructed amplitude: (a) without filter, (b) with frequency filter, (c) with wavelet threshold. (d), (e), (f) detail images.

In Fig. 3.5(a), we show the wave diffracted by the hologram in the image plane without any interference-term suppression scheme applied. The field of view is limited because of the zero-order overlap. A filtering scheme that keeps only a circular frequency band around the $+1$ order term was used to obtain Fig. 3.5(b). Finally, in Fig. 3.5(c), we show the reconstruction with the proposed algorithm. High frequency features are well preserved in regions where the zero-order does not overlap, such as the bars in the upper right. By contrast, the same bars are completely blurred in the bandpass filtering approach. The two approaches behave similarly in regions were the zero-order overlaps. Hence, the wavelet-based approach only removes high frequency information in regions already corrupted by the zero-order but keeps it intact in other regions.

3.6 Conclusion

We have proposed a zero and -1 order term suppression algorithm for digital hologram reconstruction. It takes advantage of the information distribution of the different diffraction terms in both frequency

and space. This is made possible by the use of the Fresnelet transform which has the ability to separate the information in the hologram accordingly. Unlike algorithms that are based on a bandpass filtering of the hologram, high frequency features that would normally get lost over the whole field of view are only suppressed where necessary.

Chapter 4

Complex-Wave Retrieval From a Single Off-Axis Hologram

Abstract[a]— We present a new digital two-step reconstruction method for off-axis holograms recorded on a CCD camera. First, we retrieve the complex object wave in the acquisition plane from the hologram's samples. In a second step, if required, we propagate the wave front by using a digital Fresnel transform to achieve proper focus. This algorithm is sufficiently general to be applied to sophisticated optical setups that include a microscope objective. We characterize and evaluate the algorithm by using simulated data sets and demonstrate its applicability to real-world experimental conditions by reconstructing optically acquired holograms.

---

[a]This chapter is based on Ref. [129]. We thank one of the latter paper's anonymous reviewers for providing many relevant pointers to the phase-shifting literature.

4.1   Introduction

So far, most methods that aimed at retrieving the complex wave from the hologram were directly inspired by the optical reconstruction process: The chemically processed photographic plate (the hologram) is illuminated, and the image (respectively the virtual image) is generated by the diffracted wave. The translation of this physical process into a numerical algorithm is nearly literal. Simulating the diffraction process boils down to computing the propagation of a complex wave, which can be done using several approximations [108]. The hologram may also be multiplied by an appropriate digital counterpart of a reference wave beforehand or afterward to retrieve the proper phase [36].

The most blatant disadvantage of approaches that imitate the physical process is that the reconstructed image is severely corrupted by interference terms: the zero-order and the out-of-focus twin-image. While several techniques have been proposed for removing them [38, 106, 133], the presence of these terms still remains a determining factor that limits the quality of the reconstructed image, or at least the field of view. The present approach overcomes this disadvantage by intrinsically removing the zero-order and the twin-image terms without the need for any pre- or post-processing.

The method we put forward has two steps. First, we estimate the
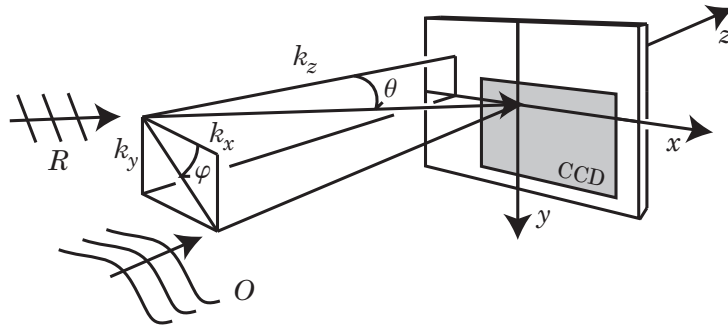
Fig. 4.1. Schematic view of the off-axis geometry.

amplitude and phase in the acquisition plane by applying a new algorithm that retrieves the complex wave in the CCD plane from the real-valued measurements. The key idea is to perform a nonlinear change of variables, so that the reconstruction may be performed by use of a method that is reminiscent of phase-shifting techniques. The algorithm is based on a local least-squares estimation of the amplitude and phase by assuming an *a priori* model of the reference wave's phase. Once the complex object wave is recovered in the acquisition plane, we (back)propagate the wave (which contains neither zero-order nor twin-image terms) to restore a focused image using a digital implementation of the Fresnel transform. This chapter concentrates on the first step, that is, the phase retrieval from a single interferogram in several configurations that fulfill the appropriate hypotheses.

We consider digital holograms acquired in an off-axis geometry (see Fig. 4.1), which permit complex wave front retrieval from one single, two-dimensional, real-valued intensity image.

This chapter is organized as follows: In Section 4.2, we briefly review existing methods for digital, off-axis holography reconstruction and, more generally, related algorithms in interferometry. In Section 4.3, we present the phase retrieval algorithm, specifically targeted to the application at hand. In Section 4.4, we present some experimental examples and validations of the technique using both synthetic (simulated) and true measurement data.

4.2   Review of Existing Algorithms

Before presenting our method, we briefly review the most widely used techniques for reconstructing digital holograms, as well as a large body of related work in interferometry.

0001000110
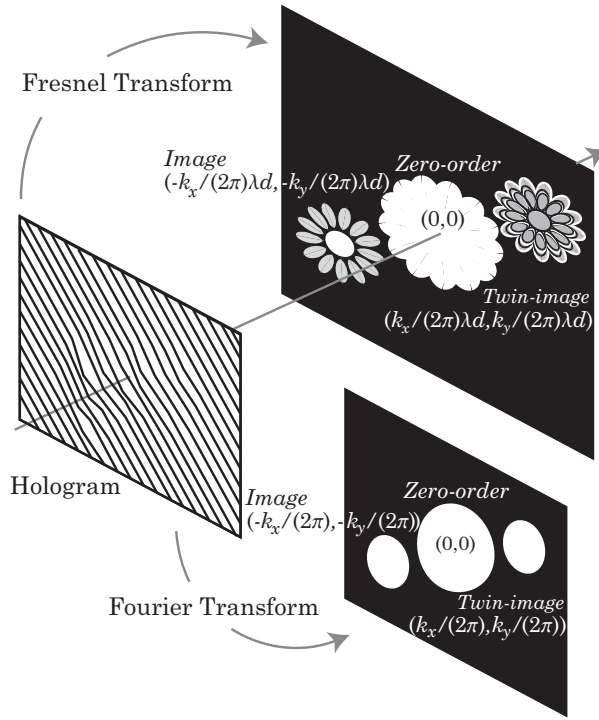
Fig. 4.2. Information separation of the interferogram using the Fourier, respectively Fresnel transform.

4.2.1 Standard (Linear) Reconstruction Techniques

The hologram originates from the interference between an object and a reference wave:

$$I(\mathbf{x}) = |R(\mathbf{x}) + \Psi(\mathbf{x})|^2$$
$$= \underbrace{|R(\mathbf{x})|^2 + |\Psi(\mathbf{x})|^2}_{\text{zero-order}} + R^*(\mathbf{x})\Psi(\mathbf{x}) + \Psi^*(\mathbf{x})R(\mathbf{x}), \qquad (4.1)$$

where $R(\mathbf{x})$ is the reference wave and $\Psi(\mathbf{x})$ the object wave evaluated in the acquisition plane. The first two intensity contributions in Eq. (4.1) are known as the zero-order term, while the third and fourth are the image and twin-image terms, respectively. These terms are superimposed in the hologram space, the plane in which the acquisition was made. When the hologram is acquired in an off-axis geometry, {that is, $R(\mathbf{x}) = \exp[i(k_x x + k_y y)]$ where $\mathbf{k}_\lambda = (k_x, k_y, k_z)$ is the wave vector}, they can be separated either by taking the hologram's Fourier transform or its Fresnel transform (see Fig. 4.2).

This is simply because the three terms are separated in the Fourier domain: the zero-order term is located around the origin, while the image and twin-image are centered on $(-k_x/(2\pi), -k_y/(2\pi))$ (image) and $(k_x/(2\pi), k_y/(2\pi))$ (twin-image), respectively. Alternatively, after application of a Fresnel transform with distance d and wavelength λ,

the three terms will be located at respective positions:

$$(0,0) \quad \text{(zero order)},$$
$$\left(-k_x/(2\pi)\lambda d, -k_y/(2\pi)\lambda d\right) \quad \text{(image)},$$
$$\text{and} \quad \left(k_x/(2\pi)\lambda d, k_y/(2\pi)\lambda d\right) \quad \text{(virtual image)}.$$

The most popular reconstruction methods for digital holograms are in essence linear techniques: They filter out the useless information (twin-image, zero-order) and keep the image information [36, 103, 104]. Instead of first transforming the hologram to another domain (Fourier domain or diffracted plane), the filtering operation can also be performed in the spatial domain by convolving the hologram with a suitable complex-valued function [216]. The frequency responses of the filters in both cases are similar.

4.2.2 Other Related Techniques

The first part of the method that we are proposing for digital holography consists of the demodulation of a fringe pattern, a general problem for which a wide variety of algorithms have been devised. One of the most popular, the Fourier transform technique [137, 202], is essentially a linear technique that selectively filters the relevant information in the Fourier domain. In fact, it is formally equivalent to the way recent zero-order and twin-image-removal algorithms for digital holography operate. Many variants have been proposed to overcome some limitations and to optimize the technique [18, 103, 158, 180]. Similar results have been achieved by using equivalent spatial convolution filters [104, 216].

Alternatively, there exist various methods that may be regarded as the spatial counterparts of temporal phase-shifting methods [74, 105]. The latter require several interferograms to be recorded, each corresponding to a particular shift of the reference's phase; the phase estimation is done at each pixel using the pixels at the same location in the other interferograms. In contrast, spatial phase-shifting algorithms [88, 110, 111, 137, 147, 175, 224] use the neighboring pixels (on the same line) of a single interferogram to carry out the estimations. The phase to retrieve is assumed to vary slowly and the carrier frequency to be constant. The general method has been improved in many ways, for example to compensate for nonideal acquisition devices and conditions [21, 25, 35, 153, 184, 187, 223].

A number of spatial demodulation algorithms have been proposed that are able to demodulate interferograms with closed fringes [115, 141, 142, 188, 229]. Thus, they might also form the basis of a two-step procedure to reconstruct digital off-axis holograms acquired in the presence of a microscope lens, since such general setups possibly

yield closed fringes. They would, however, require some adaptation to our problem, a strategy that we are not pursuing here.

Finally, a general approach for reconstructing digital holograms that inherently takes into account the statistical nature of the measured data [196, 197] may also be adapted to reconstruct our type of data.

4.3 Proposed Complex-Wave Retrieval Algorithm

Our approach to reconstructing digital holograms is decomposed into two distinct and independent parts. Starting from the digitally acquired interferogram, these are:

1. Reconstruction of the object wave's amplitude and phase in the acquisition plane by using an algorithm that is reminiscent of phase-shifting methods in interferometry.

2. Numerical propagation of the reconstructed wave front to attain proper focus in the image plane.

Here, we focus mainly on the first step. The second step, if required, can be implemented efficiently by use of a Fresnel propagation algorithm; for example, a procedure based on the Fresnelet transform (see Chapter 2 or Ref. [127]). From now on, we restrict ourselves to optical setups with an off-axis geometry. An illustration of such an arrangement is given in Fig. 4.1. We shall discuss the requirements of our method in more detail in what follows, but we can already state that they are no more demanding than those required by digital-hologram-reconstruction algorithms mentioned earlier [36, 108]. The main advantages of treating the two problems independently are as follows: (1) the approach provides more flexibility for the treatment of boundary conditions, (2) there are fewer parameters to set simultaneously (decoupling effect), and (3) the zero-order and twin-image terms are implicitly suppressed—they simply do not arise because the process does not involve simulating a wave's diffraction by the hologram.

4.3.1 Complex-Wave Retrieval Algorithm

The methodology that we follow, requires a precise description of the reference wave's phase in the form of a parametric mathematical model. The simplest example is that of a plane reference wave. We will, however, consider a more general model for the reference wave that is also suitable for the more sophisticated optical setups
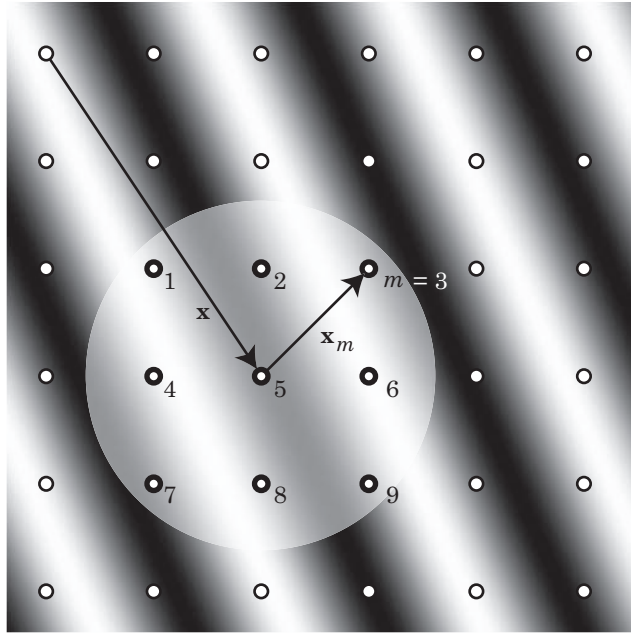
Fig. 4.3. Schematic hologram with a grid denoting the pixels' centers.

that are encountered in microscopy (Subsection 4.4.2). Both the measurement and the calibration may be done within a single acquisition frame provided that there are regions where the object wave is constant. These regions are used for the second purpose.

The key idea of our algorithm is that we consider the measured quantity $I(\mathbf{x})$, the intensity of the hologram, and $\theta(\mathbf{x})$, the phase of the reference wave in the hologram plane $R(\mathbf{x}) = A(\mathbf{x})\exp[i\theta(\mathbf{x})]$, to vary much more rapidly with $\mathbf{x}$ than the unknown quantities $\Psi(\mathbf{x}) \in \mathbb{C}$, the complex wave to retrieve, and $A(\mathbf{x}) \in \mathbb{R}_+^*$, the amplitude of the reference wave. Although modeling the reference wave's phase has proved to be very effective, doing the same for its amplitude $A(\mathbf{x})$ is much more problematic because of the latter's highly unpredictable changes observed when repeating the experiment over longer time periods (real-time imaging). For this reason we consider it an unknown.

We regard $\Psi(\mathbf{x})$ and $A(\mathbf{x})$ to be constant (lowest order approximation) within the neighborhood of a given point of interest $\mathbf{x}$. We shall discuss the requirements for this condition in more detail in Subsection 4.3.3. With this hypothesis, determining the phase and amplitude of $\Psi(\mathbf{x})$ together with $A(\mathbf{x})$ is equivalent to solving at each location $\mathbf{x}$ the following set of M nonlinear equations:

$$I(\mathbf{x}+\mathbf{x}_m) = \left| \Psi(\mathbf{x}) + A(\mathbf{x})\exp[i\theta(\mathbf{x}+\mathbf{x}_m)]\right|^2, \qquad (4.2)$$

where the $\mathbf{x}+\mathbf{x}_m$ ($m = 1,\ldots,M$) are the positions of the M pixels within the considered neighborhood of $\mathbf{x}$ (see Fig. 4.3). We further simplify

0001001010
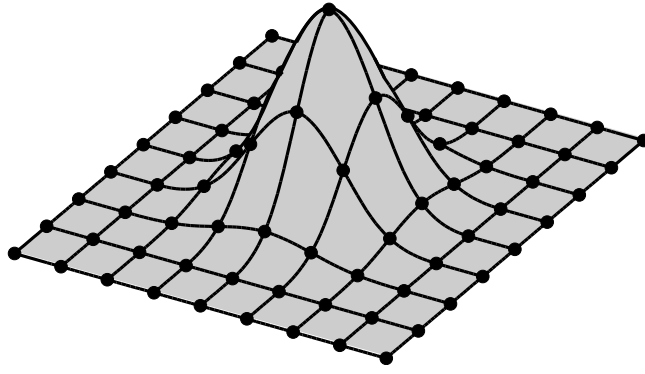
Fig. 4.4. Weights computed from the tensor product of two cubic B-splines and a window size $L_W = 9$, $M = 81$.

the notation by assigning an index m to a variable at position $\mathbf{x} + \mathbf{x}_m$:

$$
\begin{aligned}
I_m &= |\Psi + A\exp(i\theta_m)|^2 \\
&= |\Psi|^2 + A^2 + 2\Re(R_m^*\Psi).
\end{aligned} \tag{4.3}
$$

We propose to retrieve the unknown parameters by solving the above nonlinear set of equations in the least-squares sense [69], i.e.,

$$
\arg \min_{A \in \mathbb{R}_+^*, \Psi \in \mathbb{C}} \sum_m w_m \left| I_m - [|\Psi|^2 + A^2 + 2\Re(R_m^*\Psi)] \right|^2. \tag{4.4}
$$

The nonnegative weights w_m ensure that the intensities that are far away from the point of interest account for less than those that are in its close vicinity, and allow us to be consistent with the hypothesis of a (nearly) constant Ψ and A. For brevity, they are normalized such that $\sum_m w_m = 1$. In practice, we may use a simple indicator function or use weights that correspond to a smooth function, typically, a tensor product of B-splines of degree n (e.g. $n = 3$). This is a separable, bell-shaped, Gaussian-like function that is nearly isotropic and has a finite support [213]. The weighting function can be written as

$$
\begin{aligned}
w(k, l) &= \beta^n(k/s)\beta^n(l/s), \\
&\text{with } s = (L_W - 1)/(n + 1),
\end{aligned} \tag{4.5}
$$

and with $-(L_W-1)/2 \le k, l \le (L_W-1)/2$, where L_W is the side-width of the window and where $\beta^n(x)$ denotes the central B-spline of degree n. An illustration of such a weighting window, for a B-spline of degree 3 (cubic B-spline) and a window of size $L_W^2 = 9^2 = M$ is given in Fig. 4.4. Other forms of windows may be used (Hanning, etc.) but the B-spline offers computational advantages in that there exist fast convolution algorithms (either waveletlike or based on iterated moving averages) with a complexity that does not depend on the window's size [210].

We introduce the auxiliary variables $Z \in \mathbb{C}$ and $U \in \mathbb{R}_+$ defined by

$$\Psi = Z/A, \tag{4.6}$$

$$U = |Z|^2/A^2 + A^2. \tag{4.7}$$

If we now define the normalized reference wave $V_m \in \{z|z \in \mathbb{C}, |z| = 1\}$ by $V_m = R_m^*/A = \exp(-i\theta_m)$ and make the appropriate substitutions, the nonlinear problem (4.4) becomes

$$\arg\min_{U,Z} \sum_m w_m |I_m - U - 2\Re(V_m Z)|^2, \tag{4.8}$$

which may be solved by use of a linear method. The original variables Ψ and A are restored by the following (nonlinear) operations

$$\Psi = Z/A \tag{4.9}$$

$$A_\pm = + \left(\frac{U \pm \sqrt{U^2 - 4|Z|^2}}{2} \right)^{1/2}. \tag{4.10}$$

Note that these equations are well-defined and consistent with the hypothesis $A \in \mathbb{R}_+^*$ since $U^2 \geq U^2 - 4|Z|^2 = (|Z|^2/A^2 - A^2)^2 \geq 0$. Furthermore, if we make the assumption that $|\Psi| < A$, i.e., that the object wave's amplitude is smaller than the reference wave's (which is experimentally advisable to yield highly contrasted fringes), there is only one possible solution for A. The fact that $A_- \leq A_+$ and the Viète relation for the roots of Eq. (4.7), $A_-^2 A_+^2 = |Z|^2$, imply that $A_-^2 \leq |Z| \leq A_+^2$. Thus, $A_- \leq |\Psi|$, which rules this case out as an acceptable solution.

The problem now boils down to finding values of U and Z that satisfy Eq. (4.8). These must be the solutions of the normal equations:

$$\sum_m w_m [I_m - U - 2\Re(V_m Z)] = 0,$$

$$\sum_m w_m V_m [I_m - U - 2\Re(V_m Z)] = 0,$$

$$\sum_m w_m V_m^* [I_m - U - 2\Re(V_m Z)] = 0, \tag{4.11}$$

which are obtained by differentiating relation (4.8) with respect to U (which is real), Z, and Z^* (since Z is complex). If we rearrange the terms, we get

$$\sum_m w_m I_m = U + 2\Re\left(Z \sum_m w_m V_m \right),$$

$$\sum_m w_m V_m I_m = U \sum_m w_m V_m + Z \sum_m w_m V_m^2 + Z^*,$$

$$\sum_m w_m V_m^* I_m = U \sum_m w_m V_m^* + Z + Z^* \sum_m w_m V_m^{*2}. \tag{4.12}$$

0001001100

Finally, by setting $\alpha = \sum_m w_m V_m$ and $\beta = \sum_m w_m V_m^2$, we end up with a set of three linear equations to solve at every location:

$$\begin{bmatrix} 1 & \alpha & \alpha^* \\ \alpha & \beta & 1 \\ \alpha^* & 1 & \beta^* \end{bmatrix} \begin{pmatrix} U \\ Z \\ Z^* \end{pmatrix} = \begin{pmatrix} \sum_m w_m I_m \\ \sum_m w_m V_m I_m \\ \sum_m w_m V_m^* I_m \end{pmatrix}. \qquad (4.13)$$

4.3.2   Relation to Phase-Shifting Methods

We now briefly discuss similarities and differences between the proposed algorithm and related methods in interferometry. A central contribution of this chapter is the change of variables of Eqs. (4.6) and (4.7) that transforms the nonlinear holography problem (4.4) into a form that may be solved with a linear algorithm. In particular, this step may be inverted uniquely, provided that the amplitude of the reference wave is greater than that of the object wave. Once the change of variables is performed, the remaining mathematics is essentially the same as for phase-shifting algorithms: For specific choices of the reference wave (for example, a plane wave whose wave vector is horizontal) and a suitable one-dimensional weighting function, the linear part of our formulation is equivalent to previously proposed spatial phase-shifting algorithms [35, 111, 137, 147, 184, 224]. One notable difference, however, is that we consider a two-dimensional spatial weighting function that lets us be much less restrictive regarding the choice of the reference wave's form (plane, parabolic, etc.) and orientation. This point is essential, since we need to deal with non-planar reference waves in the case of microscopy. From a methodological point of view, problem (4.4) may also be seen as the spatial counterpart of the generalized (temporal) phase-shifting algorithm of Lai and Yatagai [113]. The analogy, however, is only formal since temporal phase-shifting requires several interferograms to be measured. Our method does not include all *ad hoc* developments that have been proposed to optimize both temporal and spatial phase-shifting techniques [82, 171, 176, 201], except for the use of a weighting function, which has been found to have beneficial effects, albeit only in the one-dimensional case [184, 224].

We now have to investigate the appropriateness of the hypothesis of a constant phase in the vicinity of a point. This should enable us to set the right width of the weighting function (respectively the size of the neighborhood window) to consider.

4.3.3   Sampling Considerations

The achievable resolution for holographic reconstruction is dictated mainly by two parameters: the spatial frequency of the reference wave (which influences the fringe spacing) and the sampling step of

the digital acquisition system (CCD). The bounds for the minimal sampling steps can be deduced from the Shannon–Whittaker sampling theory. A thorough treatment of the sampling of digital holograms, including aspects related to the non-ideal sampling by the CCD can be found in the literature [107, 161]. There are also closely related discussions more specific to spatial [21, 35, 166] and temporal [82] phase shifting.

In the simplest case of an interference pattern measured in a plane and involving two plane waves, it is the angle that the reference wave's wave vector makes with the object wave's that specifies the spacing of the fringes. As a simple illustration we consider a plane reference wave given by

$$R(\mathbf{x}, z) = \exp[i(k_x x + k_y y + k_z z)],\tag{4.14}$$

whose interference with an object wave that is also a plane wave traveling perpendicularly to the acquisition device plane ($z = 0$), [that is, $O(\mathbf{x}, z) = \exp(ikz)$, $k = (k_x + k_y + k_z)^{1/2}$] leads to a hologram of the form $I(\mathbf{x}, 0) = |R(\mathbf{x}, 0) + O(\mathbf{x}, 0)|^2 = 2 + 2\cos(k_x x + k_y y)$ (see Fig. 4.1). Let T be the sampling step of the CCD. To achieve alias-free sampling of the interference pattern, one must have

$$k_x < \pi/T, \qquad k_y < \pi/T.\tag{4.15}$$

The maximal incidence angle $\theta_{\max}$ is defined when $k_x = k_y = \pi/T$, in which case

$$\sin(\theta_{\max}) = \frac{(k_x^2 + k_y^2)^{1/2}}{2\pi/\lambda} \leq \frac{\lambda}{\sqrt{2}T}.\tag{4.16}$$

Thus, decreasing the incidence angle ensures that the conditions for proper sampling are met. On the other hand, working with a low carrier frequency results in the expected resolution dropping. By experimenting with our algorithm, we have found that it works well if the window covers at least one period of the interference pattern. Depending on the form of the window (simple indicator function or more sophisticated weighting function), and in the case of the most rapidly varying fringes (critical sampling), the window should be at least 3 × 3 (respectively 7 × 7 in the case of a cubic B-spline). If the window size is taken too small, the linear system becomes unstable. On the other hand, taking too large a window has the consequences of increasing the computation time and decreasing the resolution of the retrieved phase.

4.3.4 Variable-Window-Size Algorithm

So far, we have considered the weighting window to be the same for all positions at which we want to retrieve the phase, but this is not a

requirement. If the reference is not a plane wave, or if the setup involves a lens, the fringes may have a different spacing depending on the **x** position; i.e., the local carrier frequency is variable. How does one choose an optimal window size in this case? In light of the discussion in Subsection 4.3.3, having the same window size for each position is obviously not optimal. Therefore, if we have a model for the reference wave, it makes good sense to tune and adapt the window size to it. Practically, we define a table containing the width of the weighting function to consider at each position. This table can typically be designed on the basis of the reference wave's model. Since the weighting function may have to be evaluated at every location, another reason for the choice of the B-spline is that, because it is a polynomial, its computation is reasonably fast.

4.3.5   Computational Complexity

To compute the amplitude and phase for N pixels, the presented algorithm requires $\mathcal{O}(\tilde{M}N) = \mathcal{O}(N)$ operations where N is the number of retrieved phase points and $\tilde{M}$ is the average number of points covered by the window function at a given location.

The linear complexity of the present algorithm makes it attractive for large image sizes. Furthermore, the fact that we do not rely on a fast Fourier Transform (FFT)—which usually imposes periodic boundary conditions—allows us to use more general boundary conditions or to work on arbitrary regions of interest without further increasing computation time. For instance, in our implementation, we used mirror boundary conditions that give a more natural way of extending the signal and have proved to be the extension of choice in many other applications. We therefore get rid of artifacts that are typically introduced by the periodic assumption. For the image sizes we used (512×512), for a 7×7 window, and given that our implementation was designed to handle variable window sizes (and therefore does not take advantage of possible separability and convolution properties [210]), the algorithm takes approximatively 0.51 s (respectively 1.6 s in the B-spline-weighted case) whereas an FFT-based filtering typically takes around 0.56 s (1.8 GHz PowerPC G5).

For the second part of our algorithm (i.e., propagation), which usually involves the computation of FFTs, the number of operations is $\mathcal{O}[N\log(N)]$.
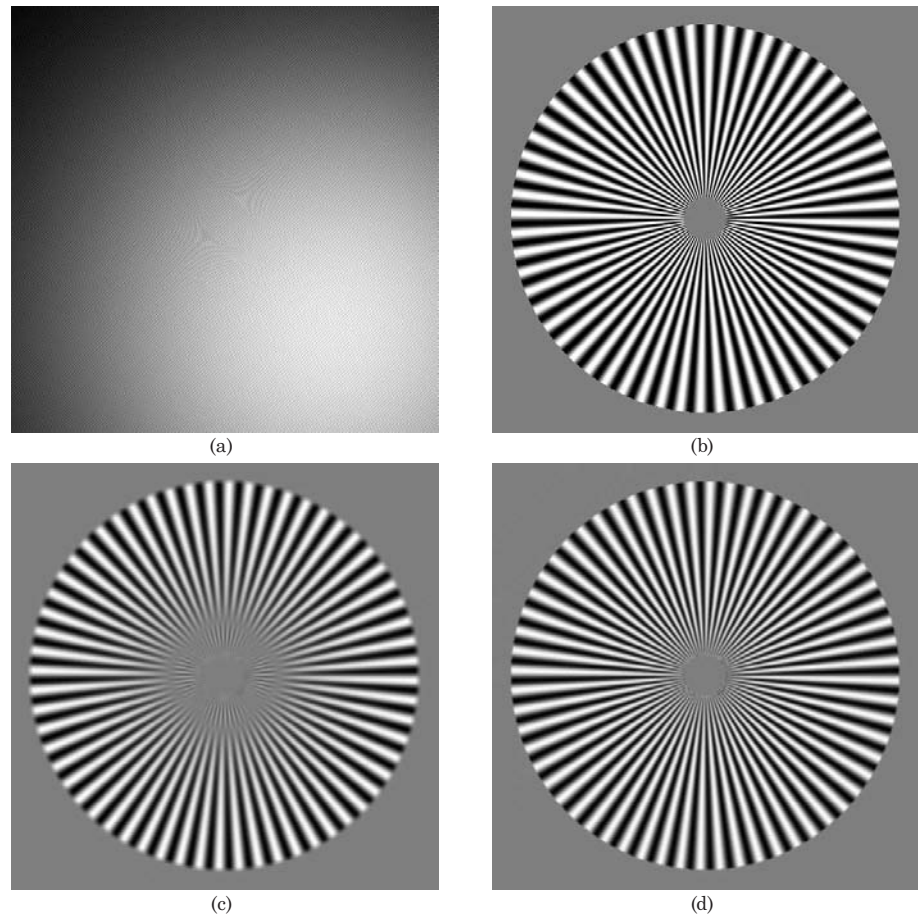
Fig. 4.5.   (a) Simulated hologram (b) Original phase (c) Reconstructed phase (d) Reconstructed phase with weighted algorithm.

4.4   Results

4.4.1   Phase-Retrieval Simulation

This first experiment consists of a simple interference simulation to test the first part of our algorithm (i.e., phase retrieval). The starting point is a test target (respectively a complex test wave) in the CCD plane. The modulus of the complex object wave is constant over the whole plane of interest while the phase follows a sinusoidal pattern depending on the polar angle. The phase varies between $-\pi/5$ and $\pi/5$. The thus-defined spoke target is shown in Fig. 4.5(b). To simulate the hologram, we create the interference by adding a complex reference wave. The latter wave is a plane wave that makes an angle of $\theta = 1.224°$ with the acquisition plane. It has a slowly varying Gaussian-shaped amplitude that is typical of experimental illumination sources. The hologram is shown in Fig. 4.5(a). The sampling step was chosen to be $T = 10~\mu$m (typical sampling step of commercial CCD cameras) and $\lambda = 632.8$ nm the wavelength (He-Ne laser). The re-

sulting fringe's k-vector (that defines the fringe's frequency and orientation) is $\mathbf{K} = (1.5, 1.5)$, resulting in a fringe period $\Lambda = 2\pi/\|\mathbf{K}\| \approx 3$ pixels. We are now aiming at reconstructing the complex test wave from the simulated interference pattern. To reconstruct the image we used a window size of 7×7 pixels at every point with either a simple indicator function or a cubic B-spline with support of 7×7 pixels. The reconstructed phase is given in Figs. 4.5(c) and (d), respectively. As expected, the resolution is limited by the respective width of the weighting functions, which is smaller for the cubic B-spline than for the indicator function. This can be verified by examining the center of the reconstructed phase in Fig. 4.5(c), where the algorithm fails to reconstruct the high spatial frequency. In Fig. 4.5(d) we can see that much better results are achieved by using the cubic B-spline weighted algorithm. The support of the weighting functions and hence the computational complexity is, however, the same in both cases.

4.4.2   Phase Retrieval for Setups Containing a Lens

We now consider the image of an object wave that has traveled through a lens:

$$\Psi_I(\mathbf{x}) = \Psi\left(\frac{\mathbf{x}}{-\mathcal{M}}\right) \exp\left(i\pi \frac{\|\mathbf{x}\|^2}{\mathcal{M}\lambda f}\right), \tag{4.17}$$

where $\mathcal{M}$ is the magnification[1], f the focal length of the lens, and λ the wavelength. It is a magnified version of the object wave $\Psi(\mathbf{x})$ multiplied by a quadratic phase term. Note that, for the sake of simplicity, we have chosen to consider an infinite-aperture lens.

We considered a wavelength $\lambda = 632.8$ nm and a lens curvature $\pi/(\mathcal{M}\lambda f) = 0.333 \times 10^8$ m^{-2}. The reference wave makes an angle $\theta = 0.6529°$ with the optical axis. We are interested in recovering $\Psi(\mathbf{x}/\mathcal{M})$ through the samples of this function. Thus we place in the image plane, perpendicular to the optical axis, a CCD whose size is 500×500 pixels with a sampling step of $T = 10$ μm. The measured hologram in the image plane is given by

$$I(\mathbf{x}) = \left| A(\mathbf{x}) \exp[i(k_x x + k_y y)] + \Psi\left(\frac{\mathbf{x}}{-\mathcal{M}}\right) \exp\left(i\pi \frac{\|\mathbf{x}\|^2}{\mathcal{M}\lambda f}\right) \right|^2, \tag{4.18}$$

with $A(\mathbf{x}) \in \mathbb{R}_+^*$. This expression can be written equivalently as

$$I(\mathbf{x}) = \left| A(\mathbf{x}) \exp\left[i\left(\frac{1}{D}\|\mathbf{x} - \mathbf{x}_c\|^2 + C\right) + \Psi\left(\frac{\mathbf{x}}{-\mathcal{M}}\right)\right] \right|^2, \tag{4.19}$$

---

[1] $\mathcal{M} = d_I/d_O > 0$, where d_O is the distance between the object and the lens, and d_I the distance between the lens and the image plane.
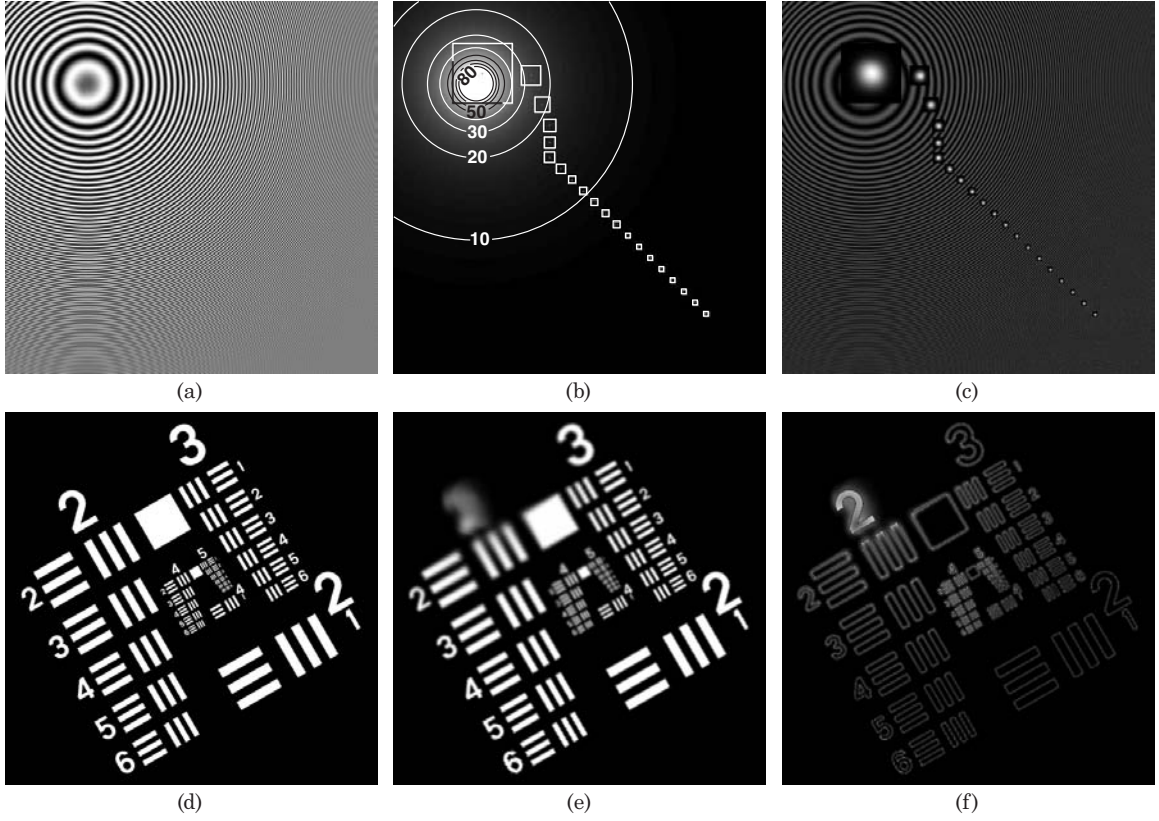
Fig. 4.6. (a) Simulated hologram. (b) Window width table visualization; maximum width: 80 pixels (white regions), minimum width: 7 pixels (black regions) (c) Weighted hologram. (d) Test wave's phase. In black regions it equals $\pi/30$, in bright regions $2\pi/30$. (e) Reconstructed phase. (f) Difference image. Black is 0, white is $3\pi/30$.

where $\mathbf{x}_c = (x_c, y_c) \in \mathbb{R}^2$, $C \in \mathbb{R}$, and $D \in \mathbb{R}^*$, and it can be interpreted as the interference of the complex wave Ψ with a non-planar wave. It is thus sufficient to adjust the parameters D, x_c, and y_c appropriately to specify our model. In real-world experiments, we determine them by a simple procedure based on a standard one-dimensional signal demodulation technique. We select a horizontal line segment from the measured hologram where the object wave's phase is assumed to be constant and where the measured intensity is therefore given by $I(x) = a(x) + b(x)\cos[(x - x_c)^2/D_x + C']$. The offset $a(x)$ is removed by low-pass filtering. We then compute the corresponding analytic signal using Matlab's HILBERT function [193]. The principal value of this signal is then unwrapped and fitted to a quadratic function yielding parameters D_x and x_c. The procedure is repeated with a vertical line segment, yielding D_y and y_c. For an astigmatism-free system $D_x = D_y = D$. Further adjustments that may be necessary are currently done manually. In case the parameters are not set correctly, our algorithm is still operational but the phase difference between the true and the modeled wave will be added to the returned phase. One

may consider other parametric models for the reference wave [140] but the procedure described above is limited to those that are separable.

Our aim in this experiment was to reconstruct a "gold standard" wave front $\Psi(\mathbf{x}/\mathcal{M})$ that has a constant intensity and whose phase is either $\pi/30$ or $2\pi/30$ according to a United States Air Force 1951 test target pattern. The phase is reproduced in Fig. 4.6(d). The reference wave is a plane wave with a constant amplitude that we set 10 times higher than that of the object wave. The resulting hologram is given in Fig. 4.6(a). The hologram consists of concentric fringes whose spacing varies in a quadratic way. We applied the variable-window-size algorithm to recover the phase. We have defined a matrix containing for each pixel of the measured hologram the size of the window to consider in order to retrieve the phase at that particular point. The maximum window size was set to $\overline{L}_W = 80$ and the minimum to $\underline{L}_W = 7$ as illustrated in Fig. 4.6(b). The side-width L_W of the window was defined as the local fringe period computed using:

$$
L_W(x, y) = \begin{cases} \underline{L}_W & \text{if } K(x, y) > 2\pi/\underline{L}_W \\ \overline{L}_W & \text{if } K(x, y) < 2\pi/\overline{L}_W, \\ 2\pi/K(x, y) & \text{otherwise,} \end{cases}
$$

where $K(x, y) = \|\mathbf{K}(x, y)\| = \|(x/D + 2x_c/D, y/D + 2y_c/D)\|$ is the norm of the local fringe k-vector. Note that we kept the minimum to be 7 pixels even though the minimal local fringe period is $\Lambda \approx 3.5$ pixels. This ensured a stable algorithm. The windows themselves were taken to be B-splines of degree 3. In Fig. 4.6(c) we show the hologram for which the pixels in the neighborhood of several locations [square regions shown in Fig. 4.6(b)] have been weighted. The reconstructed phase is given in Fig. 4.6(e) and the difference image between the original and reconstructed image in Fig. 4.6(f). We can clearly see in Fig. 4.6(e) that the whole field of view is available and not perturbed by any interference terms whatsoever. As we have a variable window size, the resolution is variable too. At places where the window size is large the resolution is low: The digit 2 is not recognizable anymore. On the other hand, in regions where the spatial modulation frequency is too high, the under-sampling introduces artifacts (see Group 2, element 6). Spatial frequencies of up to 32 lines per mm are resolved (Group 5, element 1) with a sampling step of the interferogram $T = 10\,\mu\text{m}$ (50 lines per mm). When we use windows with a variable width, our reconstruction time is much more substantial (6.9 s on a 1.8 GHz PowerPC G5 computer) but we believe that it can be decreased by using waveletlike techniques.
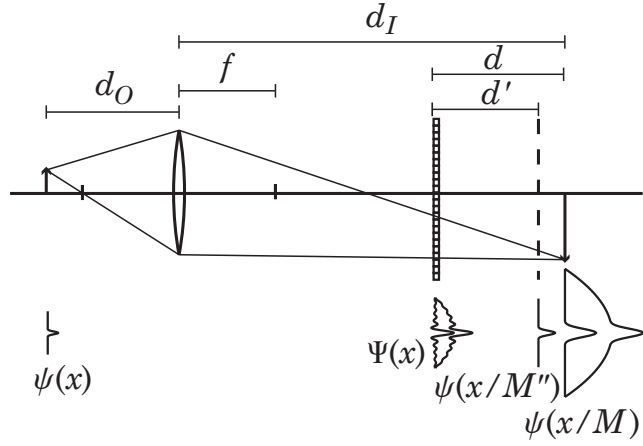
Fig. 4.7. Phase aberration compensation and phase retrieval in the case of a microscopy setup. The CCD is not in the image plane.

4.4.3 Experimental Digital Holographic Microscopy

In this experiment, we have applied our method to measurements that were performed by Cuche *et al.* with a digital holographic microscope setup [37]. The specimen (a USAF test target) is illuminated by a plane wave and the reflected light is collected by a microscope objective. The CCD camera records the interference of this object wave with a reference plane wave in an off-axis geometry. The CCD is in front of the image plane at a distance d (Fig. 4.7). This implies that the complex wave that we will recover in the camera plane will be out-of-focus and require a propagation step to yield the desired image of the specimen, as is the case for lens-less Fresnel holography.

In the vicinity of the object, we denote the reflected wavefront by $\psi(\mathbf{x})$. The complex wave in the image plane is a magnified version of the object multiplied by a quadratic phase

$$\psi_I(\mathbf{x}) = \psi\left(\frac{\mathbf{x}}{-\mathcal{M}}\right) \exp\left(i\pi \frac{\|\mathbf{x}\|^2}{\mathcal{M}\lambda f}\right) \tag{4.20}$$

Again, we have considered a lens of infinite aperture as our starting model. The expression of the complex wave in the CCD plane can be given by back-propagating Eq. (4.20) by use of the definition of the Fresnel transform

$$\tilde{\psi}(\mathbf{x}) = \mathcal{R}_{(-d)}\left\{\psi\left(\frac{\cdot}{-\mathcal{M}}\right) \exp\left(i\pi \frac{\|\cdot\|^2}{\mathcal{M}\lambda f}\right)\right\}(\mathbf{x}) \tag{4.21}$$

$$= \Psi(\mathbf{x}) \exp\left(i\frac{\|\mathbf{x}\|^2}{D}\right),$$

$$\Psi(\mathbf{x}) = \mathcal{R}_{(-d')}\left\{\psi\left(\frac{\cdot}{-\mathcal{M}''}\right)\right\}(\mathbf{x}), \tag{4.22}$$

0001010100

where

$$d' = d - \frac{d^2}{\mathcal{M}f}, \tag{4.23}$$

$$D = \frac{\lambda(\mathcal{M}f - d)}{\pi}, \tag{4.24}$$

$$\mathcal{M}'' = \mathcal{M} - d/f. \tag{4.25}$$

Equation (4.22) is a consequence of the Fresnel transform's properties [72].

Assuming a plane reference wave, the procedure to recover $\Psi(\mathbf{x})$ from $I(\mathbf{x})$ is the one described in Subsection 4.4.2, as the intensity measured by the CCD camera,

$$I(\mathbf{x}) = \left| A(\mathbf{x}) \exp[i(k_x x + k_y y)] + \Psi(\mathbf{x}) \exp\left(i\frac{1}{D}\|\mathbf{x}\|^2\right) \right|^2 \tag{4.26}$$

has the same form as Eq. (4.18). Once Ψ is recovered, the last step is its propagation up to the proper distance d' to yield

$$\psi\left(\frac{\mathbf{x}}{-\mathcal{M}''}\right) = \mathcal{R}_{(d')}\{\Psi\}(\mathbf{x}) \tag{4.27}$$

The parameters d', D, and k_x, k_y are adjusted numerically. In general, these quantities cannot be obtained experimentally with the required level of accuracy. However, in the case of a reflection setup for holographic microscopy, the phase distribution over a flat background area can be assumed to be constant and the reconstruction parameters adjusted to match this constraint. The fringe period Λ varies between 4 and 15 pixels and the window size was set accordingly in our model with the minimum window size set to 7.

In Fig. 4.8(a) we show the hologram, i.e., $I(\mathbf{x})$. Fig. 4.8(b) shows the reconstructed amplitude (phase is not shown) in the CCD plane. The amplitude and phase after applying the Fresnel transform to reach proper focus is given in Figs. 4.8(c) and (d). In Figs. 4.8(e) and (f), we show the reconstructions from the same data set obtained by using an alternative (linear) technique without any zero-order or twin-image removal scheme. In the latter approach, the quadratic-phase exponential induced by the objective is compensated numerically by multiplying the diffracted wave by a numerical phase mask [37]. The zero order is the bright square portion that masks the center of the image. The image itself is on the upper left while the twin image is located in the lower right. Only the image is in focus.

Remarkably, the reconstructions using the new approach are not perturbed by the zero-order or twin-image terms. Furthermore, the field of view is also larger.
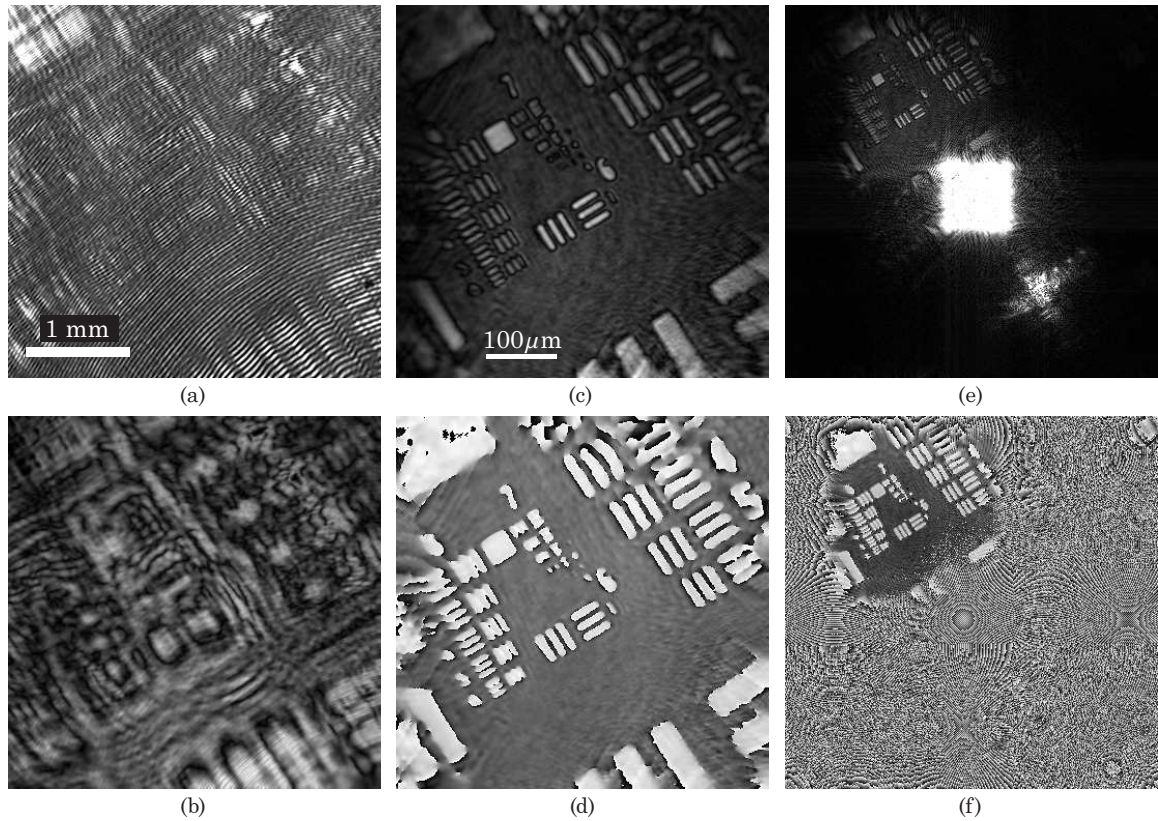
Fig. 4.8. (a) Measured hologram (Data courtesy of E. Cuche, IOA, EPFL and P. Marquet, Université de Lausanne), (b) Reconstructed amplitude in the CCD plane. Reconstructed amplitude (c), and phase (d), with adjusted focus. Reconstructed amplitude (e) and phase (f) with an alternative technique [37]. All images are 360×360 pixels. The phase images' grayscale covers the range $(-\pi, \pi]$.

4.5 Conclusion

We have presented a new approach for reconstructing complex waves from a single digital hologram. The method works for holograms acquired in an off-axis geometry. This experimental arrangement allows for the three-dimensional information to be encoded in one single interferogram, and therefore permits work at increased acquisition rates, which is required when investigating an object that undergoes fast changes. Since very low intensities can be used, it is particularly indicated for the study of biological samples. The working hypothesis for our procedure is that the object wave has slower local variations (low-pass spectrum) than the reference wave, a condition that tends to be met in a wide variety of applications. As the illumination amplitude often has a Gaussian amplitude, its spatial variation is also sufficiently slow to fulfill the requirement for the reference wave's amplitude.

The advantages of our method over others that rely on FFTs for the phase retrieval are manifold. Our algorithm has a linear complex-

ity in the number of points where the amplitude and phase are to be retrieved. Since it is a local algorithm, it offers much flexibility for working in the spatial domain: variable window size, boundary conditions, etc. Also, a local defect of quality in the measurement will not deteriorate the quality of the whole reconstruction. The problem we solve is nonlinear. We take advantage of the extra information provided by the zero order and the twin image, which is discarded in linear reconstruction methods. Since the core of our algorithm is linear, the computation time remains reasonable.

To achieve reconstruction at optimal resolution in the case of a non-planar reference wave or when microscope objectives are used, we advise use of the variable-window-size algorithm. It ensures a stable reconstruction over the whole field of view. In such circumstances, the size of the window should be adapted to the modulation frequency. To obtain a stable reconstruction, we found that the equivalent window size should be at least 3 pixels. We also recommend the use of a tensor product of cubic B-spline window functions, which are separable as well as nearly isotropic. Their finite support makes them highly suitable for a numerical implementation.

Chapter 5

Autofocus for Digital Fresnel Holograms that Uses a Fresnelet-Sparsity Criterion

Abstract[a]— We propose a robust autofocus method for reconstructing digital Fresnel holograms. The numerical reconstruction involves simulating the propagation of a complex wavefront to the appropriate distance. Since the latter value is difficult to determine manually, it is desirable to rely on an automatic procedure for finding the optimal distance to achieve high quality reconstructions. Our algorithm maximizes a sharpness metric related to the sparsity of the signal's expansion in distance-dependent waveletlike Fresnelet bases. We show results from simulations and experimental situations that confirm its applicability.

---

[a]This chapter is based on Ref. [130].

5.1 Introduction

The computerized reconstruction of complex-valued object waves from Fresnel holograms [62] acquired electronically and digitized [36, 37, 73, 103, 109, 185, 225] relies on the numerical computation of wave propagation. A possible approach for a wide variety of setups is to consider the free-space propagation formula in the Fresnel approximation, which relates the complex values of a propagating complex scalar wave measured in two planes perpendicular to the direction of propagation and separated by a distance d (see Fig. 5.1). It is defined [72] as

$$
\begin{aligned}
f_d(\mathbf{x}) &= \mathscr{R}_d\{f\}(\mathbf{x}) \\
&= \frac{\exp(i k_\lambda d)}{i \lambda d} \iint f(\mathbf{x}') \exp\left(\frac{i\pi}{\lambda d} \|\mathbf{x} - \mathbf{x}'\|^2 \right) d\mathbf{x}'
\end{aligned}
\tag{5.1}
$$

where λ is the wavelength of the light, $k_\lambda = 2\pi/\lambda$ its wavenumber, and $\mathbf{x} = (x, y)$. In a holography experiment, the interference of the diffracted wave with a reference wave is recorded on a CCD and can be written as

$$
I(\mathbf{x}) = |f_d(\mathbf{x}) + R(\mathbf{x})|^2.
\tag{5.2}
$$
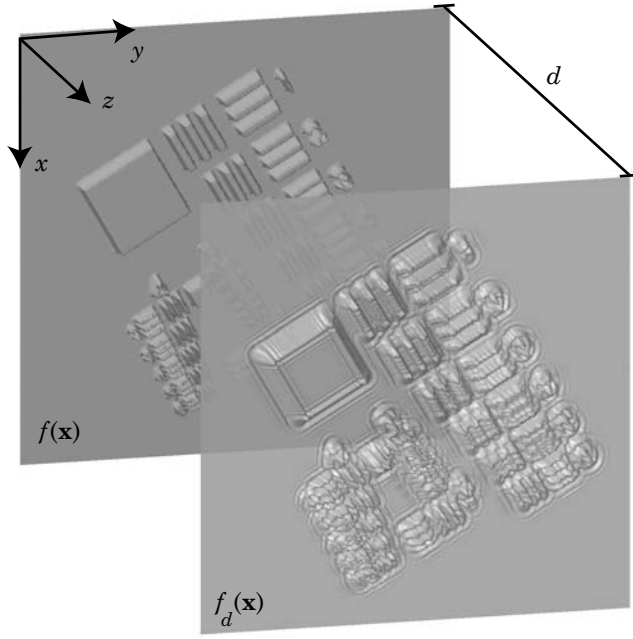
Fig. 5.1. Fresnel propagation

The reconstruction of the complex-valued wave f in the object's vicinity from one or several measurements of I may conveniently be accomplished in two steps: First, one reconstructs the wave f_d in the CCD-plane from I, for example by use of a parametric phase retrieval procedure [129], and second, one computes f through an appropriate discretization of Eq. (5.1). To perform the latter operation, the distance parameter d in Eq. (5.1) must be set accurately. In Chapter 2, we have proposed a numerical multiresolution reconstruction implementation for evaluating Eq. (5.1) based on a Fresnelet decomposition (see also Ref. [127]). Here, we show how this procedure can also be used advantageously to adjust the focusing parameter d in an accurate, robust and fast manner. Our method is based on the maximization of the sparsity of the Fresnelet representation, which appears to be a natural choice in the light of the multiresolution, wavelet-transformlike reconstruction method we have adopted.

This chapter is organized as follows. In Section 5.2, we list a number of possible approaches to autofocusing. In Section 5.3, we emphasize the concept of sparse image representations, which is central to our approach. In Section 5.4, we give the formal definition of distance-dependent Fresnelet bases and of the Fresnelet-based propagation algorithm. In Section 5.5, we introduce the autofocus algorithm and its underlying sparsity measure. In Section 5.6, we illustrate and validate the method using both synthetic (simulated) and true measurement data.

0001011010

5.2 Existing Methods

5.2.1 Image Quality Functionals

Although our algorithm is specifically designed for the reconstruction of complex Fresnel fields, it is in keeping with applications that aim at synthesizing and acquiring images, as well as assessing their quality through the evaluation (and eventually the determination of an extremum) of an image quality functional that depends on some imaging parameter to be optimized—here, the distance. More specifically, such procedures are used for providing feedback to acquisition devices for automatically setting the distance and alignment between their constituents as in optical imaging [48, 95], electronic microscopy [47] and holography [126] or for the optical reconstruction of acoustic holograms [228]. They also appear in devices that actively correct the incoming wavefront to overcome aberrations in astronomical imaging [23, 155] or microscopy [96]. Yet another use of such functionals is image quality assessment of acquisition devices and displays [132]. They are central for local sharpness evaluation in the case of image fusion and depth evaluation in images of three-dimensional scenes [76, 86] as well as for determining particle location. They are also instrumental for the estimation of unknown imaging parameters for degraded image restoration [135], digital aberration correction and deconvolution, and for computerized image reconstruction for various modalities, including coherent imaging [56, 57]. The automatic setting of the distance parameter for numerical reconstruction of complex wave fields from digitally acquired holograms (digital holography) also falls into this last category [71].

The selection of a suitable image quality metric is usually an *ad hoc* choice, driven by the imaging system's characteristics. Insensitivity to specific conditions and invariance with respect to diverse transforms [55, 192] constitute another goal. The perfect functional should be an unimodal function over a wide range of parameter values with a low computational cost [75]. Also, defining sharpness in the first place implies agreement on some *a priori* knowledge on the image to reconstruct. Possible requirements might be to achieve images with high contrast, sharp edges, or crisp details. Such criteria are highly application-dependent and possibly difficult to apply in the presence of noise.

5.2.2 Related Work

Gillespie *et al.* [71] have proposed to use the reconstructed image's self-entropy, for measuring the focus, albeit with quantized levels of gray. Ferraro *et al.* [52] have recently proposed an autofocus algo-

rithm for digital in-line holography that tracks the axial displacement of the sample in real time by measuring the phase shift of the hologram fringes. The use of an autofocus method has also been reported by Hobson *et al.* [83] although they do not give details on its implementation.

We are aware of at least three occurrences of wavelets for focus estimation and/or holographic reconstruction, albeit unrelated to the method we propose. Widjaja *et al.* [222] have proposed to improve a focus measure based on the autocorrelation of an image whose edges have been enhanced using a continuous wavelet transform. Rooms *et al.* [181] estimate image blur by analyzing the sharpness of its sharpest edges by evaluating the Lipschitz exponent based on the analysis of the scalogram, obtained by a continuous wavelet transform (CWT). Onural *et al.* [162] have proposed methods for hologram reconstruction and space-depth analysis for the three-dimensional determination of particle location by use of scaling-chirp functions. Their formulation of the Fresnel diffraction formula makes it isomorphic to the continuous wavelet transform formulation, provided the commonly-used admissibility condition is extended appropriately.

5.3   Sparse Image Representations

A standard approach in image processing and optics is to express the signal of interest as a weighted sum of basis functions. Fourier, Hermite-Gauss or wavelet bases are among the most popular candidates for such expansions. Although it is possible, in theory, to express a finite energy signal in any of these bases, in practice, the choice of one or the other is usually dictated by specific properties of the basis functions. A family might be selected, for example, because it diagonalizes an operator that is relevant to the application at hand (e.g. the Hermite-Gauss modes for fiber-optics problems). Another reason for choosing a specific basis is that it may yield a sparse representation of the signal; i.e., most of the signal's energy is packed into a few coefficients only. Local Gabor representations, and in particular wavelet bases [139], are good candidates to yield sparse representations of natural images [54, 159]. The reason for the wavelet transform's excellent energy compaction properties for a large palette of images is that wavelets are well-localized and that they yield very small coefficients in smooth signal regions thanks to their vanishing moments properties. This energy-compaction property of the wavelet transform has been recognized early on, and has proved to be useful in a wide variety of applications, ranging from superresolution image restoration [44], efficient noise reduction algorithms [45, 221] and state of the art image compression algorithms [46], including the re-

cently adopted JPEG2000 standard [90]. Sparse representations also play an important role in blind source separation algorithms [231].

Fresnel fields and holograms are not natural images, and their decomposition is sparse only if the basis functions are well-chosen. Our guiding principle to reconstruct focused wavefronts is that their expansion in a distance-dependent basis should be sparse.

5.4 Fresnelets

5.4.1 Definition

We consider the separable orthonormal wavelet basis of $L_2(\mathbf{R}^2)$

$$\left\{ \psi^1_{j,\mathbf{m}}(\mathbf{x}), \psi^2_{j,\mathbf{m}}(\mathbf{x}), \psi^3_{j,\mathbf{m}}(\mathbf{x}) \right\}_{j \in \mathbb{Z}, m \in \mathbb{Z}^2} \tag{5.3}$$

where the two-dimensional wavelets

$$\psi^p_{j,\mathbf{m}}(\mathbf{x}) = \frac{1}{2^j} \psi^p \left(\frac{\mathbf{x}}{2^j} - \mathbf{m} \right) \tag{5.4}$$

are constructed with separable products of the cubic Battle-Lemarié scaling function $\phi(x)$ and wavelet $\psi(x)$ [8, 124]:

$$\psi^1(\mathbf{x}) = \phi(x)\psi(y), \psi^2(\mathbf{x}) = \psi(x)\phi(y), \psi^3(\mathbf{x}) = \psi(x)\psi(y). \tag{5.5}$$

For the sake of brevity, we index the basis functions with a single index $\mathbf{k}$ that includes the scale j, translation $\mathbf{m}$, and wavelet type p:

$$\psi_{\mathbf{k}}(\mathbf{x}) = \psi^p_{j,\mathbf{m}}(\mathbf{x}), \quad \mathbf{k} = (p, j, \mathbf{m}) \in \{1, 2, 3\} \times \mathbb{Z} \times \mathbb{Z}^2. \tag{5.6}$$

In practice, one only considers a finite number of scales and translates (because of the finite resolution and support of the image, and appropriate boundary conditions).

A complex wave field $f(\mathbf{x})$, measured in a plane perpendicular to propagation, may be decomposed in this basis according to

$$f(\mathbf{x}) = \sum_{\mathbf{k}} c_{\mathbf{k}} \psi_{\mathbf{k}}(\mathbf{x}), \tag{5.7}$$

where the coefficients $c_{\mathbf{k}}$ are given by the inner-products

$$\begin{aligned} c_{\mathbf{k}} &= \langle f, \psi_{\mathbf{k}} \rangle \\ &= \int_{-\infty}^{\infty} f^*(\mathbf{x}) \psi_{\mathbf{k}}(\mathbf{x}) \, d\mathbf{x}. \end{aligned} \tag{5.8}$$

Note that we consider integer scale and shift parameters j and $\mathbf{m}$ which leads to a dyadic multiresolution structure [139]. This approach is different from the representation provided by continuous

wavelet transforms, which is highly redundant (i.e., not sparse) and does not have an underlying basis.

For any distance $d \neq 0$, an associated Fresnelet basis of $L_2(\mathbf{R}^2)$ can be constructed by taking the Fresnel transform of the above defined basis

$$\left\{\psi_{\mathbf{k}}^d(\mathbf{x})\right\}_{\mathbf{k}\in\{1,2,3\}\times\mathbb{Z}^3}, \quad \psi_{\mathbf{k}}^d(\mathbf{x}) = \mathscr{R}_d\{\psi_{\mathbf{k}}\}(\mathbf{x}). \tag{5.9}$$

The transformed basis functions $\psi_{\mathbf{k}}^d$ are shift-invariant on a level-by-level basis but their multiresolution properties are governed by the special form that the dilation operator takes in the Fresnel domain (see Chapter 2 or Ref. [127]). Such bases have many desirable properties required for the digital processing of holograms. For example, since they are based on splines, whose Fresnel transform may be computed analytically (see Subsection 2.4.4), they are well-defined in both time and frequency. Here, we will show that they become particularly useful for reconstructing propagated complex wave fields.

5.4.2 Fresnelet-based Propagation

The propagating wavefront may be computed at any depth given its wavelet coefficients at the origin by simply replacing the wavelet basis functions in the expansion (5.7) with the Fresnelets associated to a different depth

$$\begin{aligned} f_d(\mathbf{x}) &= \mathscr{R}_d\{f\}(\mathbf{x}) \\ &= \sum_{\mathbf{k}} c_{\mathbf{k}} \psi_{\mathbf{k}}^d(\mathbf{x}). \end{aligned} \tag{5.10}$$

Conversely, the *focused* wavefront $f(\mathbf{x})$ at the origin, may be reconstructed given complex measurements of the propagated field $f_{\bar{d}}(\mathbf{x})$ in a plane at distance $\bar{d}$ as follows

$$f(\mathbf{x}) = \sum_{\mathbf{k}} c_{\mathbf{k}}^d \psi_{\mathbf{k}}(\mathbf{x}). \tag{5.11}$$

where $c_{\mathbf{k}}^d = \langle f_{\bar{d}}, \psi_{\mathbf{k}}^d(\mathbf{x})\rangle$. It is only when the distance is well adjusted ($d = \bar{d}$) that we have $c_{\mathbf{k}}^d = c_{\mathbf{k}}$ and that the reconstruction leads to a focused image. The focus measure that we propose lets us determine the quality of the computed coefficients, that is, the quality of our reconstruction.

5.5 Proposed Autofocus Algorithm

5.5.1 Algorithm Description

Our starting hypothesis is that the wavelet coefficients $c_{\mathbf{k}}$ for focused images are sparse. To decide whether the computed coefficients $c_{\mathbf{k}}^d$ are satisfactory, we thus need a measure that depends on their sparsity. We define the focus measure $S(d)$ as follows. For a test depth d, we compute the Fresnelet coefficients $c_{\mathbf{k}}^d = \langle f_{\tilde{d}}, \psi_{\mathbf{k}}^d(\mathbf{x}) \rangle$. The coefficients are sorted: we define a mapping $\mathbf{k} = \mathbf{k}(l)$ such that

$$\left| c_{\mathbf{k}(l-1)}^d \right| \geq \left| c_{\mathbf{k}(l)}^d \right| \geq \left| c_{\mathbf{k}(l+1)}^d \right|, \tag{5.12}$$

with $0 < l < L$ and where L is the total number of coefficients. The sharpness metric $S(d)$ is the energy of the signal that is reconstructed with the fraction $0 < \alpha < 1$ of highest modulus coefficients, viz.

$$\begin{aligned} S(d) &= \iint \left| \sum_{l=0}^{\lfloor \alpha L \rfloor} c_{\mathbf{k}(l)}^d \psi_{\mathbf{k}(l)}(\mathbf{x}) \right|^2 d\mathbf{x} \\ &= \sum_{l=0}^{\lfloor \alpha L \rfloor} \left| c_{\mathbf{k}(l)}^d \right|^2. \end{aligned} \tag{5.13}$$

The second equality is a consequence of the basis functions $\psi_{\mathbf{k}(l)}$ being orthonormal. In practice, we typically set $\alpha \approx 1\%$. An initial depth range is defined for example by rough measurements or estimates made on the experimental setup. The typical distance range for a lensless digital holography setup is about 0.2 m. Our autofocus algorithm maximizes the $S(d)$ criterion by applying a combined golden section search and parabolic interpolation maximization algorithm [174].

The focusing problem may be summarized as follows: we aim at finding the best Fresnelet basis such that as much of the image energy is encoded with as few coefficients as possible. This idea is very similar to the following problem of linear algebra in a two-dimensional cartesian vector space. On the road map shown in Fig. 5.2, we determine the highway's direction (the reconstruction distance) by using an instrument that is initially oriented toward the North Pole and that measures a test car's two coordinates in an orthonormal basis but only displays the highest (the quality metric). The instrument, hence the basis, is rotated until the device displays the maximum value, which gives us the orientation we are after. Some *a priori* knowledge is nevertheless required for this method to be effective: the car should be driving on the highway (but not at the origin) and the initial guess should be no more that 45 degrees away from the true value. It is noteworthy that all the rotated bases—like the Fresnelet bases for different distance parameters d—are equivalent in that they all allow to express the position of any car on the map.
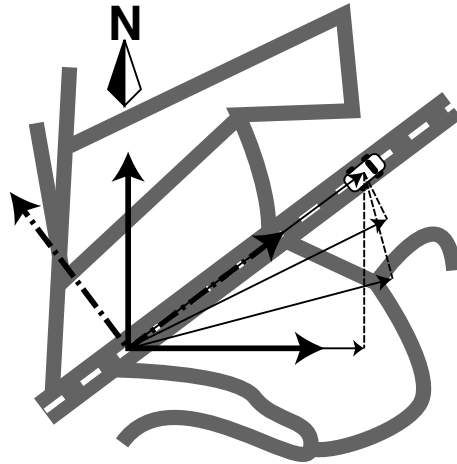
Fig. 5.2. The orientation of the highway is given by the orientation of the basis in which the representation of a car's position is sparsest.

5.5.2 Computational Complexity

The cost for sorting the L coefficients is $\mathcal{O}(L\log L)$ [186]. The cost for computing a Fresnelet transform, which relies on fast Fourier transforms (FFT), is of similar complexity, i.e. $\mathcal{O}(L\log L)$. The minimization procedure usually converges in less than 10 iterations. The whole autofocusing procedure for a 512×512 pixels images takes around 9 s on a PowerPC G5 1.8 GHz computer, but we believe that the implementation may be optimized for specific applications and allow for real-time processing.

5.6 Results and Discussion

5.6.1 Sparsity Illustration

We have simulated the propagation of a coherent monochromatic scalar complex wave. The diffracted wave was computed at a distance of $d = 0.1$ m using a procedure we described in Subsection 2.6.1 (see also [127]). Its intensity and phase is shown in Figs. 5.3(a) and (b). We then applied the Fresnelet decomposition with bases of different distance parameters d, ranging from 0.01 m to 0.19 m. In Figs. 5.3(c) and (d), the positions of the wavelet coefficients that account for 95% of the signal's energy are shown. More than one and a half times as many coefficients are required when the Fresnelet parameter $d = 0.086$ m is used than when the correct parameter $d = 0.1$ m is applied. In Fig. 5.4, we show the Fresnelet coefficient's energy packing for different distances; we have sorted the Fresnelet coefficients in decreasing order, and reported their relative cumulated energy. From the inset,
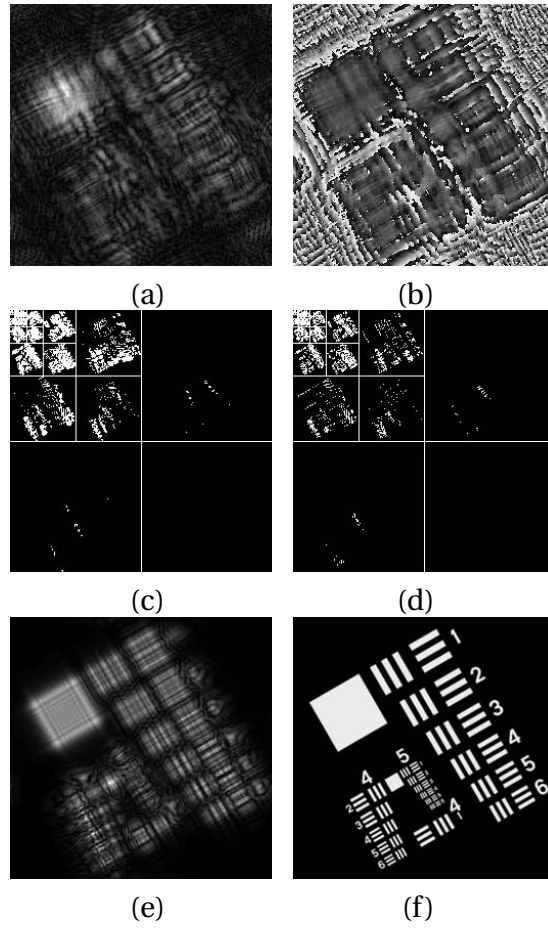
0001100000

Fig. 5.3. Sparsity of wavelet coefficients. (a) Intensity and (b) phase of measured complex field at a distance $d = 0.1$ m. (c) Positions of the 5% highest Fresnelet coefficients for parameter $d = 0.09$ m that account for 95% of the signal's energy. (d) The same energy is packed in only 3.1% of the coefficients when $d = 0.1$ m. The respective reconstructions are given in (e) and (f).

it is clearly visible that the larger the distance difference between the Fresnelet parameter and the focus distance, the weaker the energy packing. We show the sharpness metric $S(d)$ in Fig. 5.5(a) along with two other metrics, the fourth power of the wave's modulus and the squared modulus of the intensity's Laplacian computed as follows:

$$S_4(d) = \iint |\mathscr{R}_{-d}\{f_{\bar{d}}\}(\mathbf{x})|^4 d\mathbf{x}, \tag{5.14}$$

$$S_L(d) = \iint |\Delta|\mathscr{R}_{-d}\{f_{\bar{d}}\}(\mathbf{x})|^2|d\mathbf{x}. \tag{5.15}$$

The maximum is reached for the optimal distance $d = 0.1$ m for all three sharpness metrics. However, the Laplacian and squared intensity metrics exhibit local maxima, even in our ideal, noiseless situation. In Fig 5.5(b), we show the same curves in the case where 10% gaussian random noise was added to the propagated wave field before reconstruction.
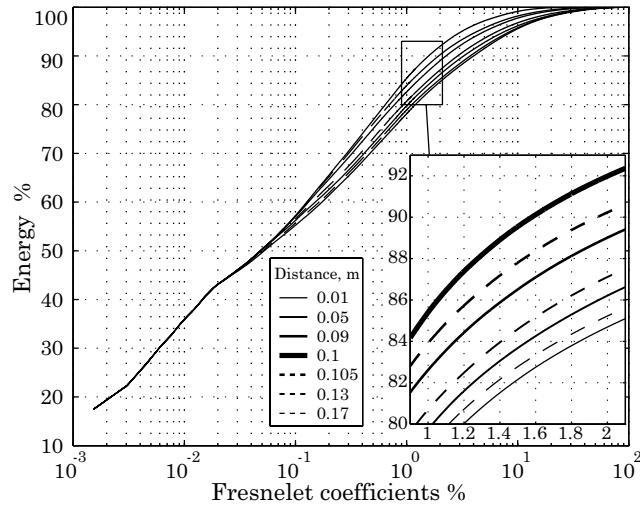
Fig. 5.4. Wavelet coefficient energy for several Fresnelet bases and detail (inset).

Since Fresnelet coefficients—like wavelet coefficients—may be assimilated to the derivatives of the two-dimensional function along the horizontal, vertical and diagonal directions [212], they are also related to quantities that appear in the computation of the Laplacian sharpness metric. For the latter, they would mostly correspond to the high-pass coefficients of the Fresnelet transform. However, these are highly sensitive to noise which make the Laplacian sharpness metric useless in noisy conditions (see Fig. 5.5(b)). Conversely, these coefficients do not contribute to our sparsity metric, since they carry little energy and are removed—similarly to wavelet-based noise reduction algorithms [45, 221]. For this reason, our method is robust to noise, i.e. suitable for experimental situations.

In this experiment, the autofocus algorithm converged to a relative precision of 10^{-3} in as few as 9 iterations.

5.6.2 Experimental Measurements

In Fig. 5.6, we show the amplitude of the unfocused and focused wave fields obtained from experimental data. The amplitude and phase was computed using the phase retrieval algorithm presented in Chapter 4 (see also [129]). The sharpness curves for the same metrics as in Subsection 5.6.1 are also given. We can see that our proposed sparsity metric behaves well, even in experimental conditions. Conversely, the two other metrics are unreliable, since at best, they only reach a local maximum for the proper distance.
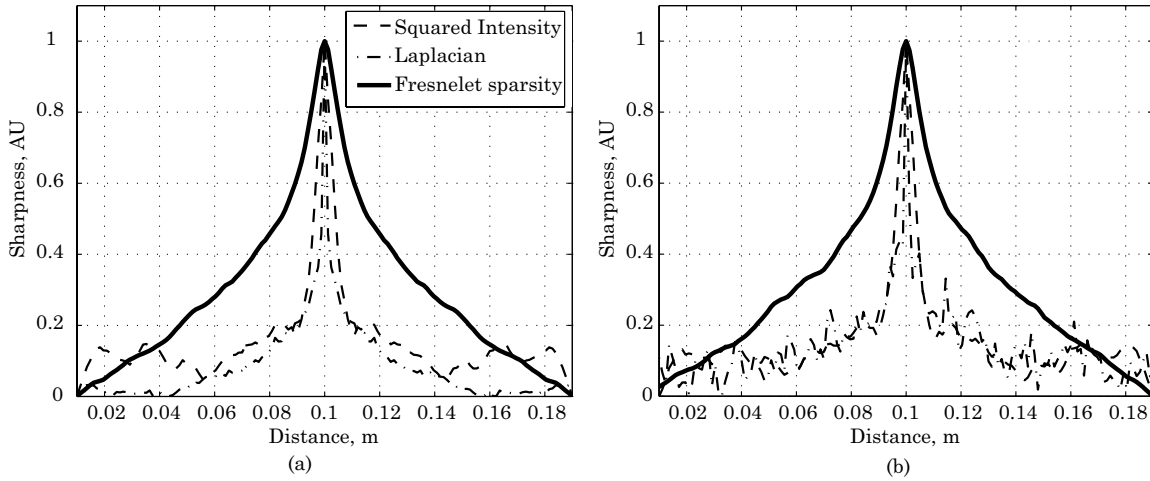
0001100010

Fig. 5.5. Sharpness metrics as a function of the distance. (a) Ideal noiseless data (b) Noise corrupted data: 10% gaussian random noise was added to the complex valued propagated wave of Fig. 5.3(a). The sparsity of the Fresnelet transform is given by the energy of $\alpha = 1\%$ Fresnelet coefficients.

5.7 Conclusion

We have proposed a novel sharpness metric for the reconstruction of digital holograms based on the computation of the sparsity of a Fresnelet decomposition. The global maximum of this functional corresponds to a sharp reconstruction. Because it is smooth and unimodal even in the presence of noise, the localization of its maximum may be carried out without an exhaustive search but only by evaluating it for a limited number of distances. This is a crucial aspect of our metric since the computational cost of computing the wavefront at many distances can become important. Other simple metrics that exhibit local maxima are useless because then, finding the global maximum requires exhaustive search. The sharpness measure has indeed all the characteristics of a good functional; in particular, it is robust and does not require a large computational overhead, since it is tightly related to our reconstruction technique. Although a wide-variety of wavelets (Daubechies, etc.) may be considered for building Fresnelets, we advise the use of cubic Battle-Lemarié wavelets, since they may be constructed using B-splines, which have closed-form expressions in both time and frequency and yield a simple implementation. It is important, however, that the wavelet basis be orthonormal to ensure the validity of Equation (5.13).

Finally, we have confronted our technique to both synthetic (simulated) and experimental data and observed that it is suitable for real applications.
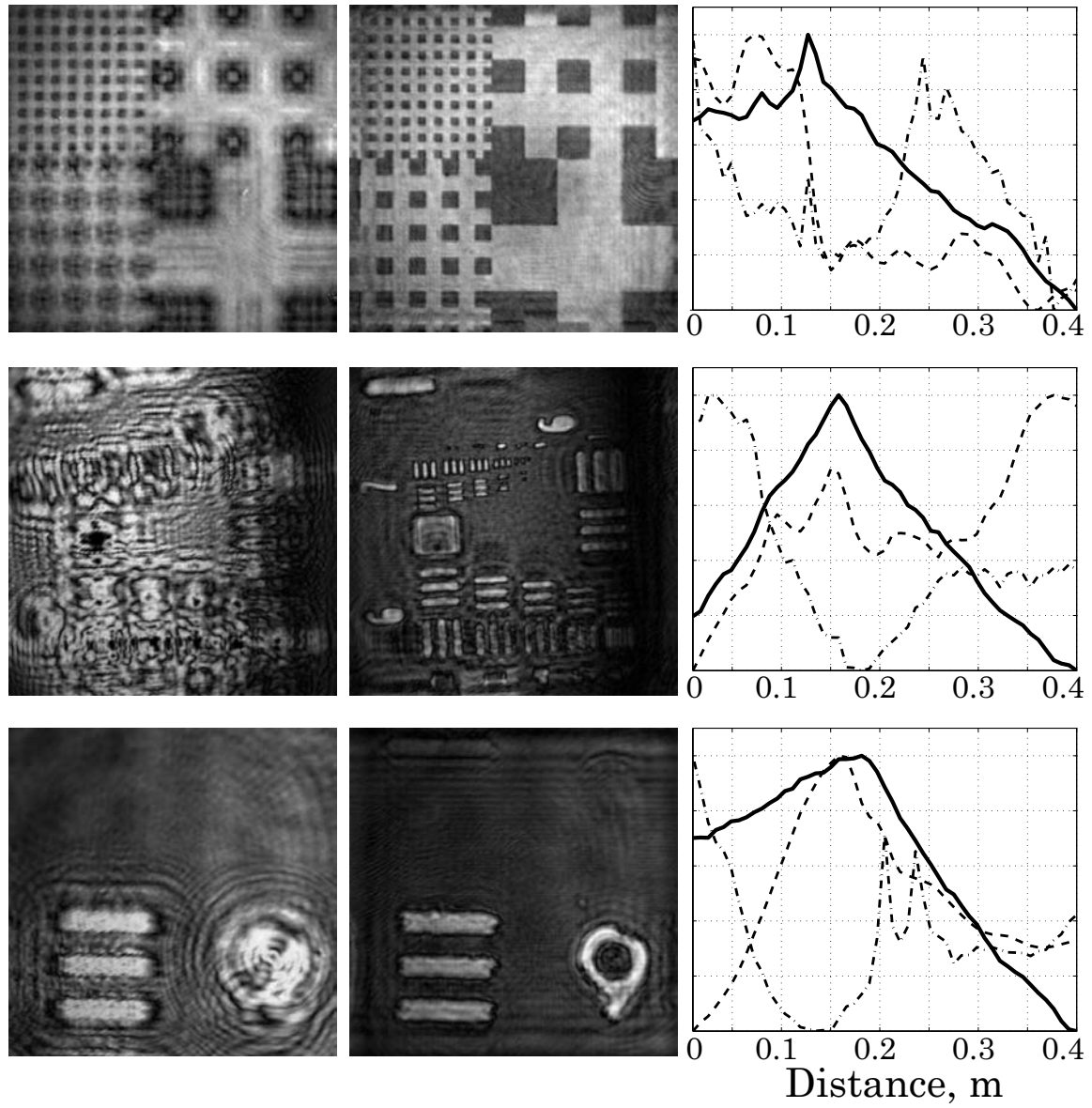
Fig. 5.6.   Out-of-focus and focused modulus of wavefront, and sharpness metrics (Laplacian of intensity (dashed), squared intensity (dashed-dotted) and wavelet sparsity (bold)). The experimental data was kindly provided by E. Cuche and Ch. Depeursinge, École Polytechnique Fédérale de Lausanne, Switzerland.

Chapter 6

Comparisons and Conclusion

Abstract—The purpose of this chapter is manifold. We aim at providing a number of guidelines for deciding which algorithm to apply to a given problem. We propose a simulation study to compare previously existing and the newly proposed reconstruction procedures. We carry out the evaluation based on various criteria: reconstruction quality, computational complexity, memory requirements, success and failure of the phase retrieval, ease of use (when setting parameters). We show that Fresnelet decompositions play an important role in the conceptual analysis of digital holography but also lead to concrete implementations. Whenever possible, we point out the relationship between the compared algorithms. Finally, this analysis will allow to point toward new directions for future research.

6.1   Introduction

Up to this point, the thesis has been mainly concerned with proposing new tools and methods for reconstructing holograms. In Chapter 2, we have used a nonlinear approximation of the hologram in the Fresnelet domain to suppress the unwanted zero and minus 1 order terms in the reconstructed hologram. In Chapter 4, we proposed to decouple the phase retrieval problem and the propagation problem and we came up with a versatile method for retrieving the amplitude and the phase from a single hologram. Here, we compare the different algorithms (newly proposed and existing ones) on a quantitative and qualitative basis using a simulation procedure, in order to draw a more complete picture of their relative performances. Although an evaluation based on synthetic data might possibly neglect some aspects that are present in true experimental conditions, it has the invaluable advantage of giving insight into the performances of the algorithms on a quantitative basis.

There is no algorithm that is superior to all others in every situation. A method that may seem optimal for a given setup may well become obsolete as soon as a new technology (camera, computer,...) becomes available or economically more attractive. The design of digital holography setups has largely been influenced by the computational limitations of early calculators. The simpler and faster algorithms would be chosen because there was not alternate way to carry out the computations within reasonable time. Such considerations

have undoubtedly led to the design of experimental setups optimized for the fastest algorithm. However, methods that were abandoned because they did not meet the speed requirements have not necessarily been reevaluated in the light of the currently available computing power. An algorithm should be adapted to the problem and not the other way around.

As a consequence, we put strong emphasis on how flexible an algorithm is. It should be ready for technological improvements of digital cameras, such as lower sampling steps, larger camera size and the increased storage capacity and clock speed to be expected from future computers.

There have been only few attempts to quantitatively compare and evaluate the performance of different digital hologram reconstruction algorithms in an extended number of situations. Most validation tests have been carried out on experimental data for which the true gold standard is difficult to access. A noteworthy exception is a validation proposed by Cuche *et al.* [36, 39], who compared the reconstructed phase (respectively, the profile) of a USAF test target to the height measured by scanning a contact-stylus probe profilometer over the same sample. Repeating such an experimental procedure in a large number of configurations would be of highest interest, mainly because it takes into account the whole optical system. However, the time required by such a study would most likely be prohibitive. What we propose here instead is to evaluate the algorithms at hand on a quantitative basis, by restricting the number of influent parameters and by using an exact gold standard. This is made possible by simulating the acquisition process. Even if this does not replace experimental validation, it gives precious insight on the respective impact of each single parameter on the overall performance of the different algorithms.

The situations we present in the following sections are not meant to constitute an exhaustive set of all possible parameter combinations. Rather, they have been carefully selected to illustrate the algorithms' strengths or possible weaknesses. For quantitative evaluation, we rely on adapted versions of the signal-to-noise ratio. Whenever visual comparison was possible we have favored this option, since signal to noise ratios do not necessarily reflect visual artifacts.

This chapter is organized as follows. In Section 6.2, we give a list of parameters that influence the acquisition and reconstruction of digital holograms. In Section 6.3, we discuss issues related to the quantitative evaluation of the algorithms and define the chosen criteria. In Sections 6.4 and 6.5, we compare the newly proposed algorithms with previous ones in a number of situations and discuss their relative advantages in the case of lensless digital holography and digital holographic microscopy. In Section 6.6, we propose a synthesis of

0001100110

the gathered findings. Finally, in Section 6.7, we have a general look back on the contributions and main results presented throughout the thesis as well as a look forward at future refinements, extensions and possible research directions.

6.2 Parameter Influence for the Reconstruction of Holograms

Once the hologram is stored in digital form (a 2D array of (quantized) numbers), we may start with the reconstruction. The simulation methodology may include various aspects of the experimental acquisition procedure. In particular, the following parameters may be taken into account.

- Light (source)
  - spatial coherence
  - temporal coherence
  - wavelength
  - intensity profile

- Optical elements and setup
  - parasitic reflections
  - nonideal system response
  - finite apertures
  - dust on optical elements
  - discrepancy from model

- Object (wave)
  - distance d from focused image
  - aberration due to lens (parabolic) D_x, D_y
  - finest details/bandwidth
  - spatial extent

- Reference wave, geometry
  - angle to object wave
  - plane/parabolic wave
  - intensity: power ratio, intensity profile

- Acquisition device
  - Sampling step T
  - Number of samples N_x, N_y
  - Nonlinear response; Gamma factor γ
  - Frequency response of acquisition device (nonideal sampling)
  - Noise sources

- Quantization
- Corrupted regions, treatment of regions of interest

In the next sections, we will investigate the reconstruction algorithms' performances by varying several of these parameters.

6.3   Quality Measures for Reconstructed Wave Fronts

In this section we propose three quality measures for comparing reconstructed wave fronts to a gold standard in a simulation procedure. We therefore consider the comparison of two 2D complex-valued, sampled functions $f(\mathbf{x})$ and $f'(\mathbf{x})$.

We first need to recall that phase retrieval algorithms that rely on a single fringe pattern and no a priori knowledge are subject to a sign ambiguity and phase offset inherent to the interference patterns: a general interference pattern given by

$$|a\exp(i\alpha) + b\exp(i\beta)|^2 = a^2 + b^2 + 2ab\cos(\alpha - \beta), \qquad (6.1)$$

may equivalently be produced by the phase couples α', β':

$$\alpha' = +\alpha + \delta \qquad \text{and} \qquad \beta' = +\beta + \delta, \qquad (6.2)$$
$$\text{or } \alpha' = -\alpha + \delta \qquad \text{and} \qquad \beta' = -\beta + \delta, \qquad (6.3)$$

with $\delta \in \mathbb{R}$. The sign ambiguity may be alleviated by using some a priori knowledge; the phase offset is arbitrarily set to zero. Furthermore, only the principal argument of the complex number $Z = a\exp(i\phi) \in \mathbb{C}$, $a \in \mathbb{R}_+$, $\phi \in \mathbb{R}$ is available and not the phase *per se*. The phase is said to be *wrapped* [70]:

$$\mathscr{W}\{\phi\} = \arg Z = \phi + 2k\pi, k \in \mathbb{Z} : -\pi < \mathscr{W}\{\phi\} \leq \pi. \qquad (6.4)$$

We make use of the following congruence property when comparing phases:

$$\mathscr{W}\left\{\mathscr{W}\{\phi_1\} - \mathscr{W}\{\phi_2\}\right\} = \mathscr{W}\{\phi_1 - \phi_2\}, \text{ if } -\pi < \phi_1 - \phi_2 < \pi. \qquad (6.5)$$

Thus, if the difference is sufficiently small, we may evaluate the reconstruction quality without having to unwrap the result.

We define three quality measures for comparing complex-valued images. The first definition of the *Signal to noise ratio* (SNR) is as follows:

$$\text{SNR} = 10\log_{10} \frac{\sum_{\mathbf{k}} |f_{\mathbf{k}}|^2}{\sum_{\mathbf{k}} |f_{\mathbf{k}} - f'_{\mathbf{k}}|^2} \qquad (6.6)$$
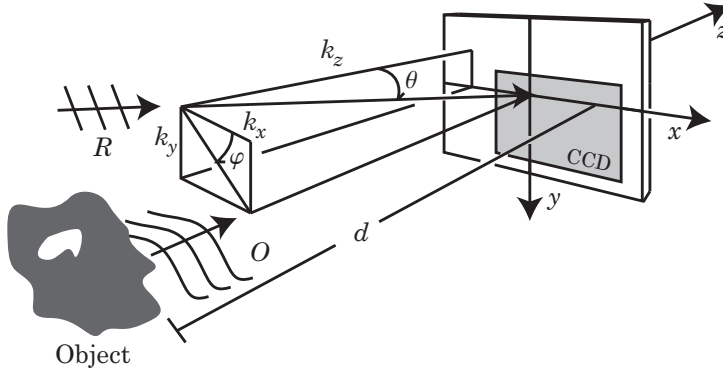
0001101000

Fig. 6.1. Setup for lensless digital Fresnel off-axis holography.

where $f_{\mathbf{k}} = a_{\mathbf{k}} e^{i\phi_{\mathbf{k}}} \in \mathbb{C}$ is the gold standard image and $f'_{\mathbf{k}} = a'_{\mathbf{k}} e^{i\phi'_{\mathbf{k}}} \in \mathbb{C}$ the reconstructed image. Since results in digital holography are usually given in terms of amplitude and phase, we also define the two following quality measures, for the amplitude and the phase, respectively:

$$\text{SNR}_{\text{amp}} = 10\log_{10} \frac{\sum_{\mathbf{k}} |f_{\mathbf{k}}|^2}{\sum_{\mathbf{k}} (|f_{\mathbf{k}}| - |f'_{\mathbf{k}}|)^2} \tag{6.7}$$

$$\text{SNR}_{\text{ph}} = 10\log_{10} \frac{\sum_{\mathbf{k}} |\phi_{\mathbf{k}}|^2}{\sum_{\mathbf{k}} (\mathcal{W}\{\mathcal{W}\{\phi_{\mathbf{k}}\} - \mathcal{W}\{\phi'_{\mathbf{k}}\}\})^2}. \tag{6.8}$$

The indices $\mathbf{k}$ are taken over a suitable portion of the image. In all subsequent experiments, it covers a centered square whose size is 60% of the total image width to factor out boundary effects.

6.4 Lensless Fresnel Off-Axis Holography: a Comparison

In this section we examine digital hologram reconstruction algorithms in the case of a lensless setup, as shown in Fig. 6.1. We set the wavelength to $\lambda = 632.8$ nm. The reference wave vector is $\mathbf{k}_\lambda = (k_x, k_y, k_z)$ and the wavenumber $k_\lambda = 2\pi/\lambda = (k_x^2 + k_y^2 + k_z^2)^{1/2}$. The camera has a sampling step $T = 10~\mu$m and $N_x \times N_y = 512 \times 512$ pixels. We simulated the propagated wave at a distance d from the object and added a complex reference wave with parameters $K_x = k_x/T$ and $K_y = k_y/T$. We then computed the squared modulus of the resulting field. We sampled the latter on the area corresponding to the
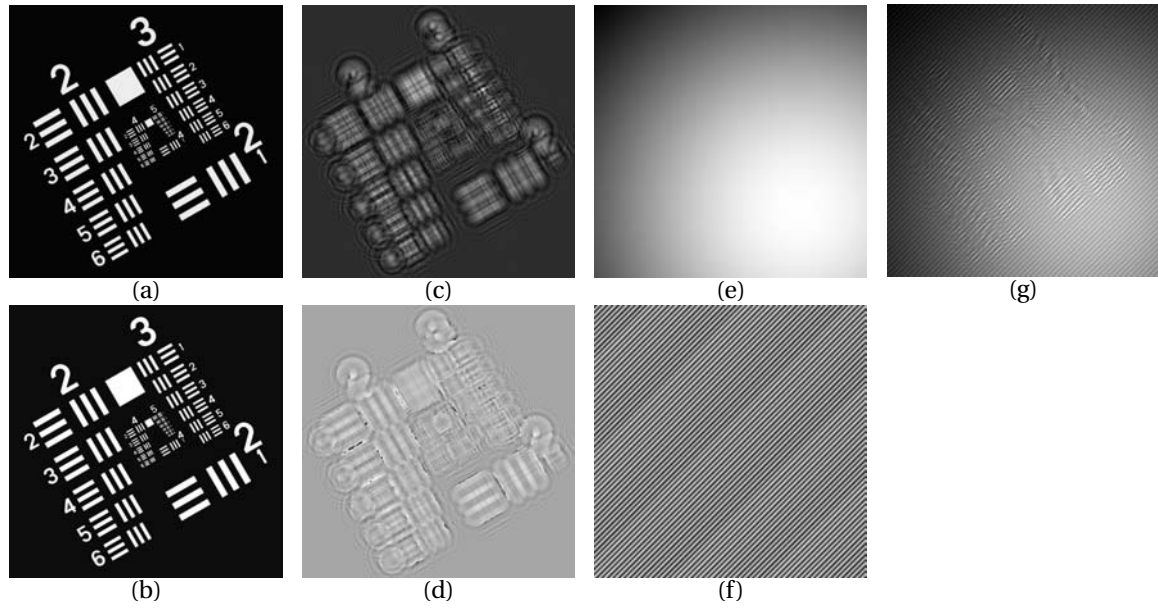
Fig. 6.2. Gold standard test target object wave. Amplitude $[0.5, 1.5]$ (a) and phase $[-0.2\pi, 0]$ (b) in the vicinity of the object. Amplitude (c) and phase (d) in the CCD plane. Reference wave amplitude (max amplitude: 10) (e) and (wrapped) phase (f). (g) Hologram. Parameters are $T = 10$ μm, $N_x = N_y = 512$, $\lambda = 632.8$ nm, $d = 0.05$ m and $K_x = K_y = -0.6$.

camera's support, again with a sampling step T. In Fig. 6.2 we show the steps that lead to the gold standard test target.

We investigate the influence of the following parameters: nonuniform amplitude, distance between the object and the CCD, angle between the object and the reference wave. We also consider situations where only a limited region of interest is reconstructed, either because only a limited region of interest is available, or, because whole areas are severely corrupted by noise.

6.4.1 Fresnelet Pyramid Versus Chirp-Fourier Fresnel Transform

The central part of every Fresnel hologram reconstruction algorithm is the computation of the Fresnel transform.

One particular algorithm, referred to as the Chirp-Fourier Fresnel transform (ChFFrT), is widely used. Its implementation corresponds to the sampling of Eq. (2.17), while assuming that the signals are bandlimited[1]. Its main advantage is that it may be implemented by computing a single FFT rather than the two required by the discretization of convolution-based approaches[2].

---

[1] Several variations of this method are described in Refs. [226, 227] in a more general context. We consider only the simplest form in this comparison.

[2] Note that the Fresnelet pyramid may be implemented directly in the space domain. We didn't follow this approach though, because it is competitive only for
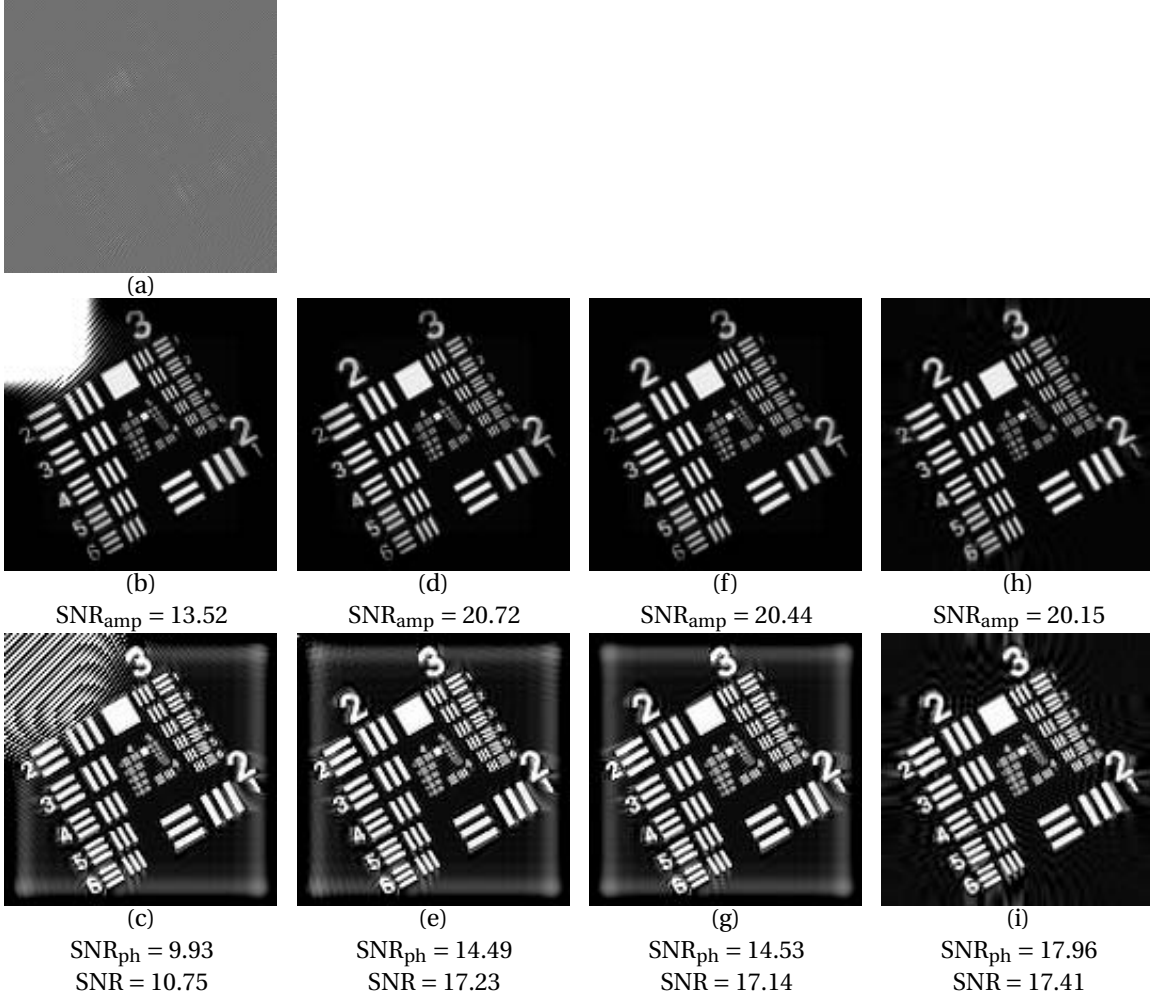
Fig. 6.3. Chirp-Fourier Fresnel transform versus Fresnelet pyramid. (a) Hologram, 512×512 pixels, $K_x = K_y = 1.1$, $d = 0.323$ m. ChFFrT reconstructed (b) amplitude (c) phase. ChFFrT reconstruction with Fourier method of zero order removal (d) amplitude and phase (e). Fresnelet pyramid reconstruction (f) amplitude, (g) phase. LSE phase retrieval and Fresnelet pyramid (h) amplitude (i) phase. All reconstructions are 128×128 pixels in size ($m = 2^2 = 4$).

We have already seen the advantages of the Fresnelet pyramid over the ChFFrT, in terms of the strong constraints that the ChFFrT puts on the sampling step (See Section 2.7). Comparisons of the relative merits and disadvantages of the convolution approach (including different convolution kernels) and the ChFFrT are also discussed in Ref. [108].

Here, we propose a further experiment. Since the Fresnelet transform is a multiresolution procedure, we can select situations where the Fresnelet pyramid at scale m (with sampling step mT) has the same sampling step as the ChFFrT (sampling step $T' = \lambda d / (NT)$). In this case, it is possible to compare the two on a pixel-per-pixel basis.

small distances and coarse resolutions.

0001101011

To get a similar sampling step for both reconstructions, we impose:

$$mT = \frac{\lambda d}{NT} \qquad (6.9)$$

which determines

$$d = mNT^2/\lambda. \qquad (6.10)$$

For example, if we set $m = 4$, $N = 512$, $T = 10\ \mu$m, and $\lambda = 632.8$ nm, then we must set $d = 323.640$ mm to achieve (6.9). We chose $K_x = K_y = 1.1$.

In Fig. 6.3 we show the inverse Fresnel transforms starting from the simulated hologram. The SNR is slightly higher for the Fresnelet pyramid approach. We can also see that the zero-order is visible in Figs. 6.3(b) and 6.3(c) and can be removed by the Fourier method (Figs. 6.3(d) and 6.3(e)). As can be seen in Figs 6.3(f) and 6.3(g), The Fresnelet pyramid does not require any further treatment for it already corresponds to a low pass filter . Since only a limited portion of the hologram is available (i.e. of the size of the CCD) we have multiplied the hologram with an apodization window prior to reconstruction to avoid artifacts introduced by the boundaries. Finally, in Figs 6.3(h) and 6.3(i), we show the reconstruction using the least-squares estimation (LSE) method followed by a Fresnelet transform, as described in Chapter 4. Since no apodization window is required, the reconstruction is free of the characteristic distortions in the phase.

One should also note that, if the ChFFrT method is at most twice as fast (for the same image size) than a convolution-based approach, which requires two instead of only one FFT, this is no longer true when the reconstruction is to be performed several times, e.g. during adjustment of the distance parameter. In the latter case, the convolution approach only requires one FFT since the hologram's FFT remains unchanged and makes the method even faster than the ChFFrT method. A simple parallelization may also allow to keep the speed of both algorithms the same.

However, the argument turns in favor of the ChFFrT when zero-padding is required to avoid the overlap of the different orders (as is the case in the convolution based reconstructions presented in Figs. 6.3(d) to 6.3(g)). But again, when the demodulation is tackled separately from the propagation, this argument is no longer relevant: neither zero-padding nor apodization is required because the zero and -1 order terms are not present, as for example in Figs 6.3(h) and 6.3(i).

Because of its speed, the ChFFrT is of high interest if the setup (reconstruction distance, angle) is tuned in consequence. The sampling constraints are, however, so strong that it is less interesting in the general case. We will use a Fresnelet (convolution) type Fresnel
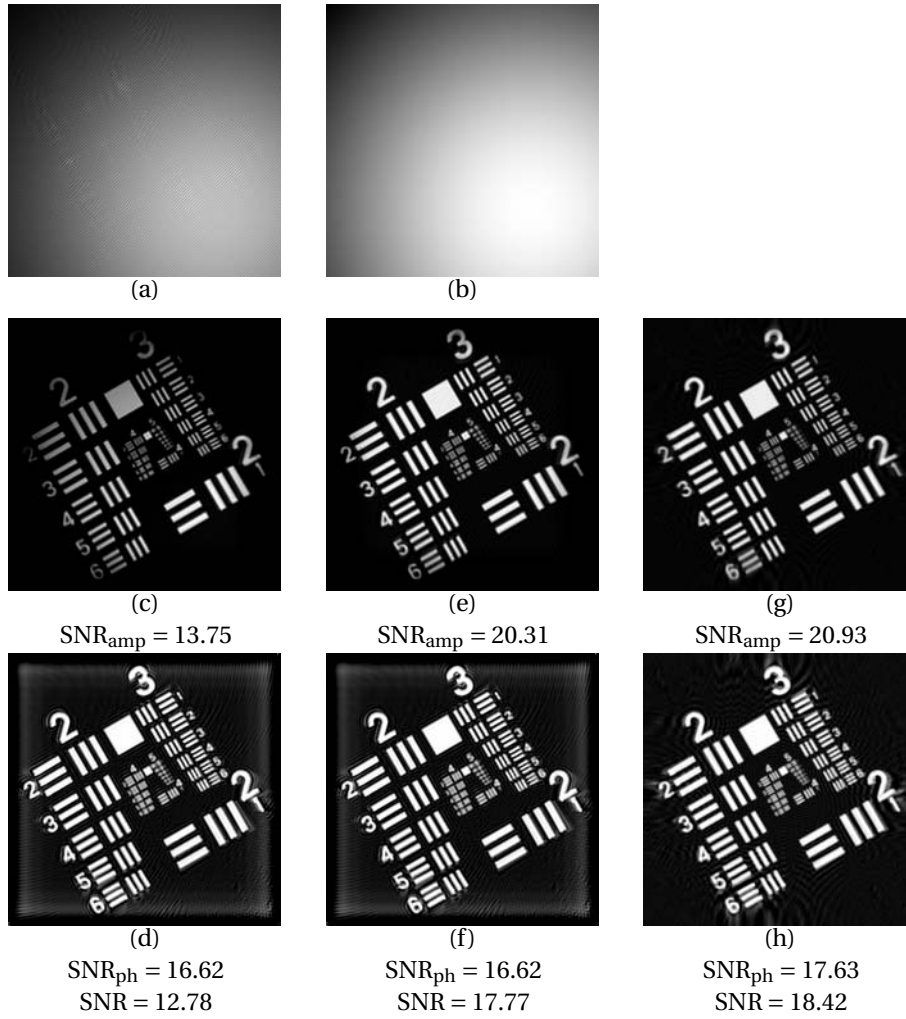
(a)   (b)

(c)   (e)   (g)

SNR$_{amp}$ = 13.75   SNR$_{amp}$ = 20.31   SNR$_{amp}$ = 20.93

(d)   (f)   (h)

SNR$_{ph}$ = 16.62   SNR$_{ph}$ = 16.62   SNR$_{ph}$ = 17.63
SNR = 12.78   SNR = 17.77   SNR = 18.42

Fig. 6.4.   Nonuniform amplitude hologram (a) obtained from a nonuniform amplitude reference wave (b), $d = 0.2$ m, $K_x = K_y = -1.0$. Fourier method reconstruction of amplitude (c) before, and (e) after division by the reference's amplitude (b). (d), (f): Corresponding phase. Reconstructed amplitude (g) and phase (h) with the least-squares procedure.

transform to compare all methods from now on, since it has the advantage of keeping a constant sampling step T.

6.4.2   Nonuniform Amplitude

Before we proceed further into the comparison of the different algorithms, we need to shed some light on an often overlooked liability of many digital holography methods. Algorithms that filter out the positive order produce an output signal that is the product of the object wave's amplitude and the reference, i.e., $|R(\mathbf{x})O(\mathbf{x})|$. If the reference wave is assumed to be constant, the result is simply a scaled version of the object wave's amplitude. Although plane waves with a constant

amplitude are conceptually convenient, they cannot be produced in practice. The output of a laser is typically a Gaussian beam, that is, the intensity has a Gaussian profile if measured in a plane perpendicular to the propagation direction[3]. A simple procedure to recover the true object wave amplitude would be to measure the reference wave amplitude separately and point-wise divide the hologram by $|R(\mathbf{x})|$ prior to reconstruction. Yet, this would require one supplementary (possibly time-consuming) measurement. The LSE algorithm, on the other hand, is able to retrieve the phase and the amplitude of the object wave from a single hologram. The only requirement is that the intensity of the object wave be lower than that of the reference. Another possible approach to overcome the amplitude indetermination is to also consider a parametric model for the amplitude.

In Figs. 6.4(c) and 6.4(e), we show the reconstructions obtained from the Fourier filtering (the phenomenon is the same for the Fresnelet approximation procedure of Chapter 3) algorithm before and after dividing the retrieved amplitude by that of the reference. We see that the amplitude of the reconstruction is influenced by the nonuniform reference wave. The LSE method yields the proper amplitude directly. The retrieval of the phase is not affected by the uncertainty on the reference's amplitude.

Since we aim at comparing the algorithms quantitatively, we will assume in further experiments that the amplitude of the reference wave is known (e.g. through a supplementary measurement), except when we use the LSE algorithm, which does not require this assumption.

6.4.3   Distance and Angle

In this subsection, we investigate the influence on the reconstruction quality of the distance parameter d and the angle between the reference and the object wave. We have considered that the distance between the object and the CCD varies between 0.01 m and 0.4 m and generated the corresponding holograms. We have reconstructed the amplitude and phase images using the following algorithms: a plain Fresnel transform, a Fourier filtering followed by Fresnel transform, the Fresnelet approximation (see Chapter 3) and the LSE followed by a Fresnel transform.

In Fig. 6.5, we show the SNR quality curves for the tested situations. In Figs. 6.6, 6.7, and 6.8 we show the reconstructed amplitudes and phases with the different algorithms for various angles between the reference and the object wave.

---

[3]In practice, the presence of a pinhole (to filter the appropriate mode(s)) further truncates the Gaussian.
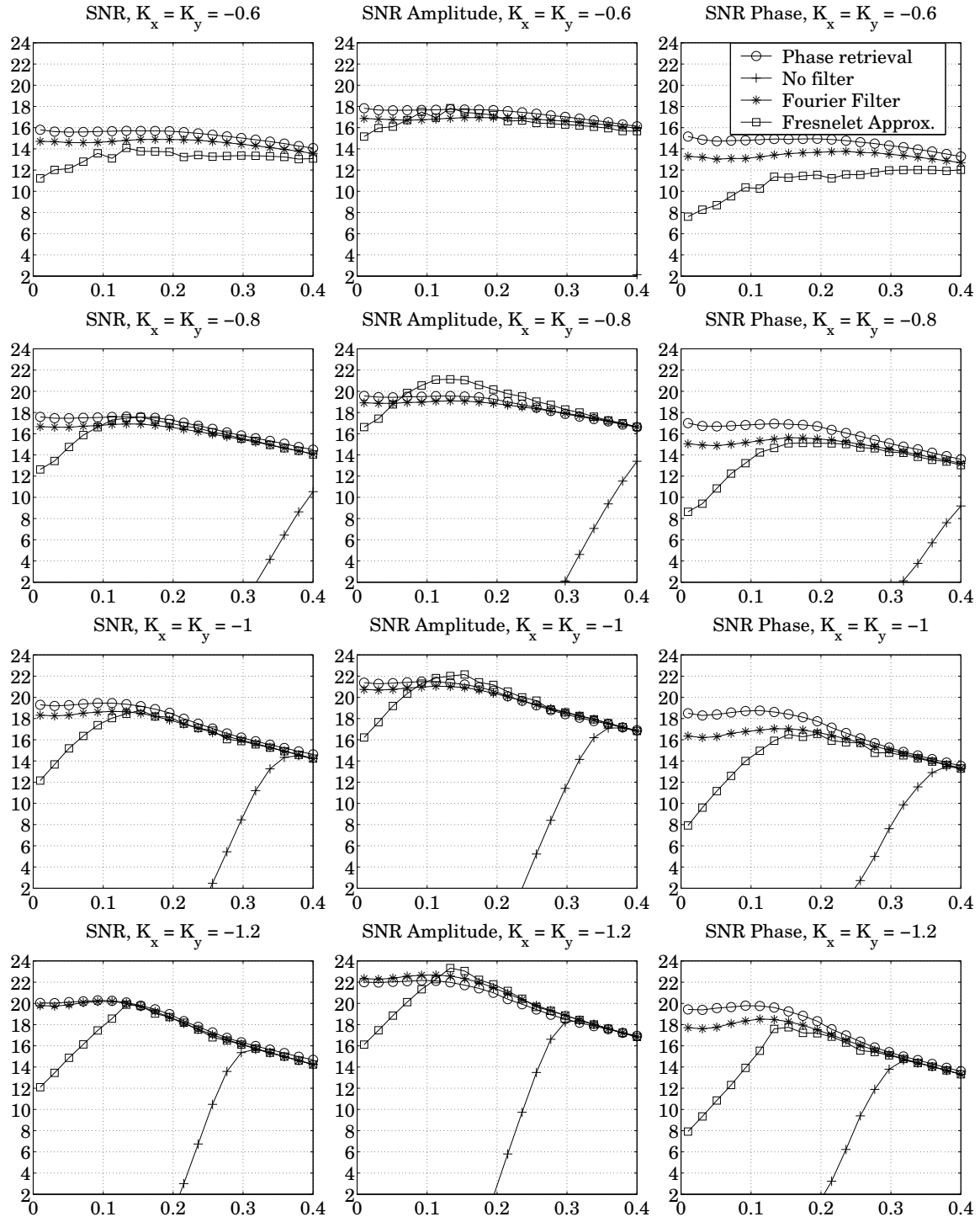
Fig. 6.5. Reconstruction quality [SNR]=dB as a function of distance [d]=m. From top to bottom $K_x = K_y = -0.6, -0.8, -1, -1.2$.
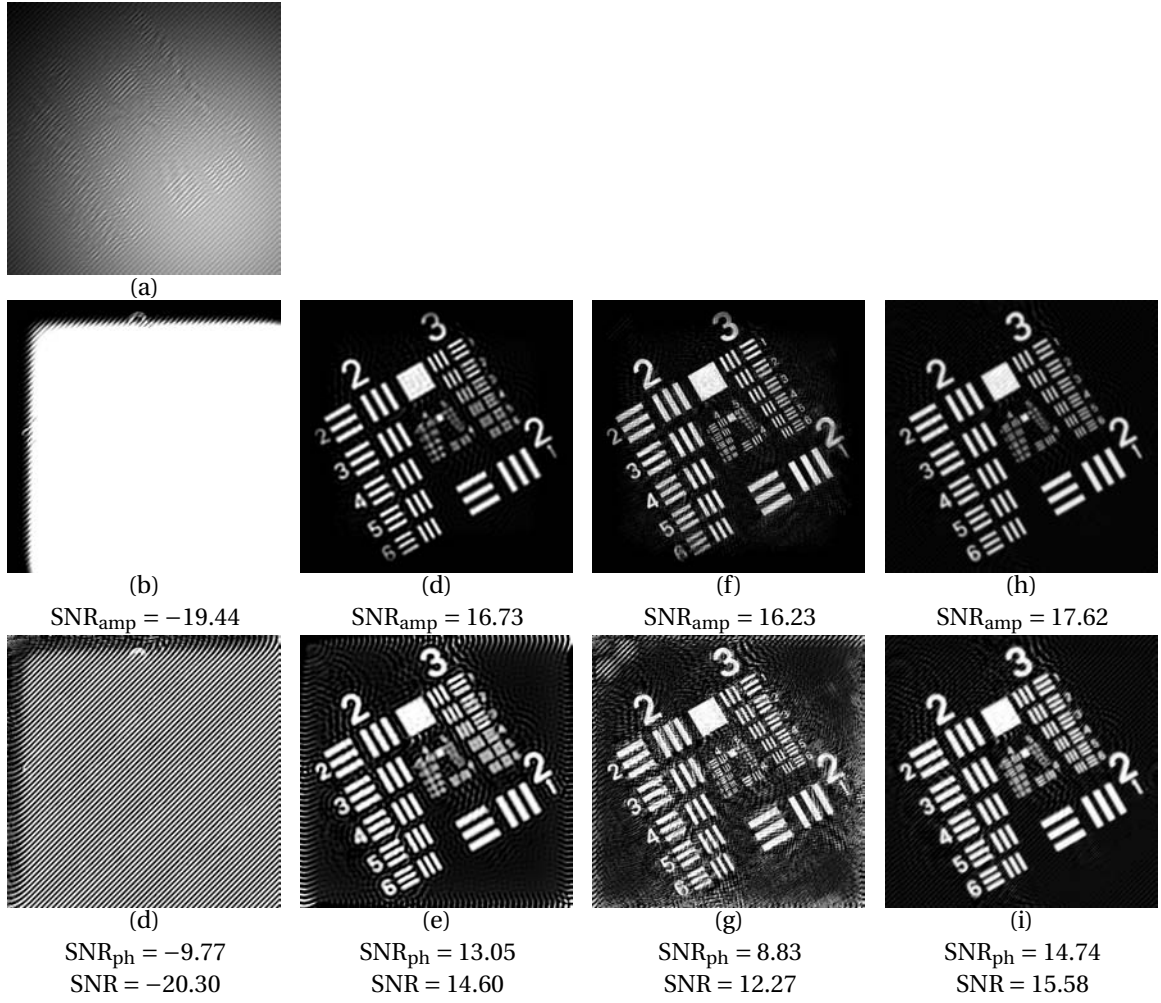
(a)

(b)
SNR$_{amp}$ = −19.44

(d)
SNR$_{amp}$ = 16.73

(f)
SNR$_{amp}$ = 16.23

(h)
SNR$_{amp}$ = 17.62

(d)
SNR$_{ph}$ = −9.77
SNR = −20.30

(e)
SNR$_{ph}$ = 13.05
SNR = 14.60

(g)
SNR$_{ph}$ = 8.83
SNR = 12.27

(i)
SNR$_{ph}$ = 14.74
SNR = 15.58

Fig. 6.6. Reconstructions (top amplitude, bottom phase) for $d = 0.05$ m and $K_x = K_y = -0.6$. Algorithms from left to right: Plain Fresnel transform, Fourier filtering and Fresnel transform, Fresnelet approximation, LSE and Fresnel transform.

We notice that the curves are similar for the overall quality and the amplitude. We see that a larger distance can compensate for a lower angle. When no filtering is used, it is the product $(k_x + k_y)^{1/2}\lambda d$ which is crucial: the reconstruction is uncorrupted by the zero-order term only if this value is well above the object's support.

One can see that the Fresnelet approximation gives better results (amplitude reconstructions) when a compromise between space and frequency filtering is achievable. This corresponds to regimes where the product $d\lambda(k_x^2 + k_y^2)^{1/2}/(2\pi)$ is larger than zero (the different orders do completely overlap) but smaller than the support of the image (the different orders are completely separated in the space domain). As soon as the different orders are well-separated in space, neither the Fourier filtering nor the Fresnelet approximation bring an advantage over the plain Fresnel transform. When the distance is zero, only the Fourier filtering and the LSE algoriths are capable of retrieving meaningful information. It is also noteworthy that the LSE method outper-
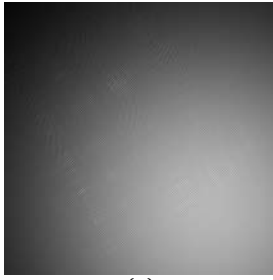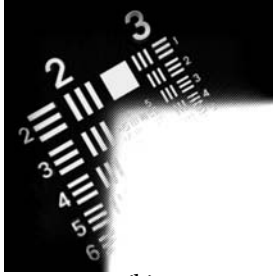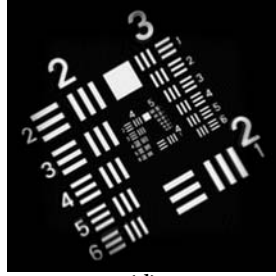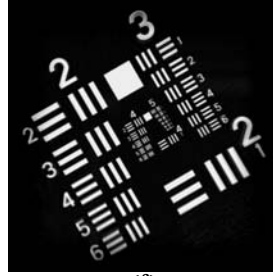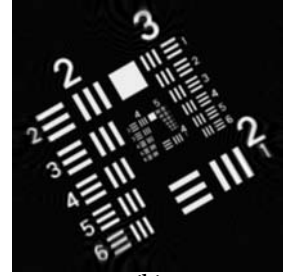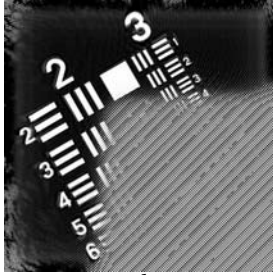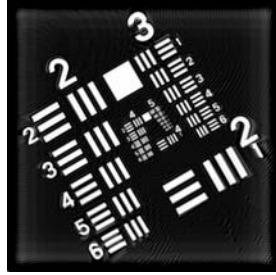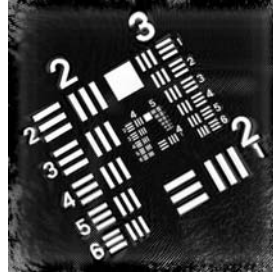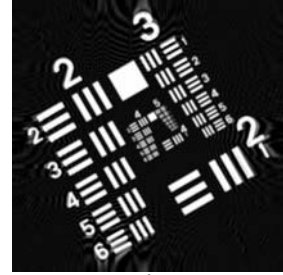
Fig. 6.7. Reconstructions (top amplitude, bottom phase) for $d = 0.15$ m and $K_x = K_y = -1.2$. Algorithms from left to right: Plain Fresnel transform, Fourier filtering and Fresnel transform, Fresnelet approximation, LSE and Fresnel transform.

forms the other approaches, especially for low $K_{x,y}$; i.e., for low angles. For the higher angles, the Fourier filtering method yields better amplitude results. The latter amplitude, however, needs to be compensated to be meaningful (see Subsection 6.4.2). Also, this is true only if we limit the part of the image that is taken into account for computing the SNR to the center rather than taking the whole field of view.

Overall, the reconstruction quality decreases as the distance increases. This is due to the fact that the CCD has a limited support; it therefore misses important information that spreads outside its boundaries. In certain cases, however, a nonzero distance is unavoidable because of space constraints dictated by the optical elements.

Generally speaking, we observe that the quality increases as the angle increases. There is of course an upper bound on the maximal angle that is dictated by the CCD's sampling step.
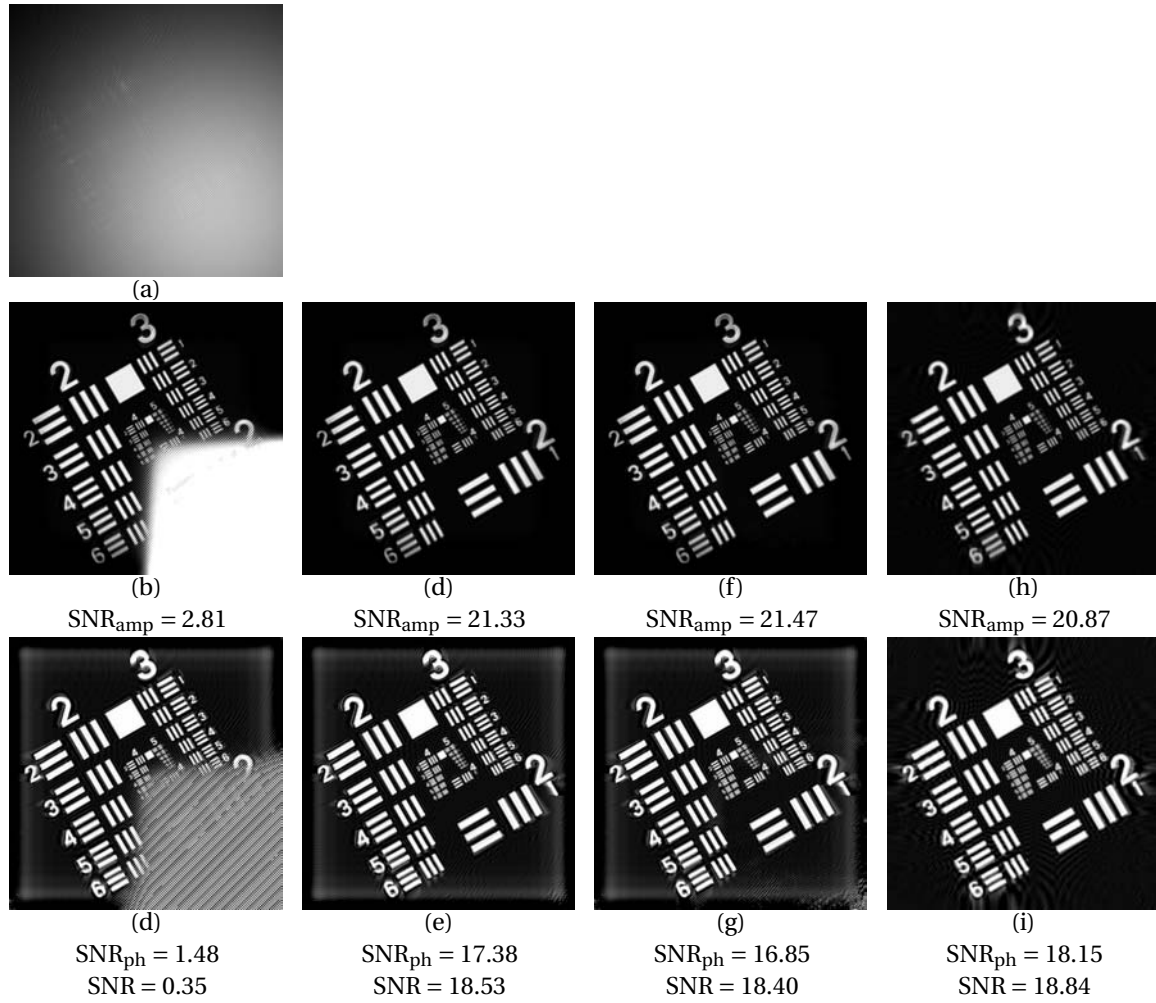
Fig. 6.8. Reconstructions (top amplitude, bottom phase) for $d = 0.2$ m and $K_x = K_y = -1.2$. Algorithms from left to right: Plain Fresnel transform, Fourier filtering and Fresnel transform, Fresnelet approximation, LSE and Fresnel transform.

6.4.4 Regions of Interest

In this experiment we investigate the performance of the different algorithms when the hologram is severely corrupted in several, well delimited regions. For convenience, we set the distance $d = 0$ m. Such a situation may be realized experimentally if the hologram is taken in the image plane of an object-lens system, and the reference wave is such as to produce parallel fringes. One could also think of a situation where several CCDs are used to record the holograms, with gaps in-between where no data is available.

In Fig. 6.9, we show the hologram thus-obtained and the respective reconstructions with the Fourier filtering, Fresnelet approximation and LSE method (the plain Fresnel transform was left out because the distance is zero). We see that the corrupted regions do not interfer with the LSE reconstruction. This is not the case for the
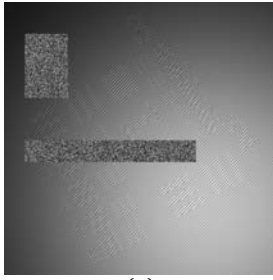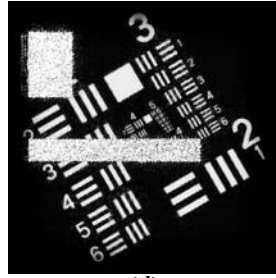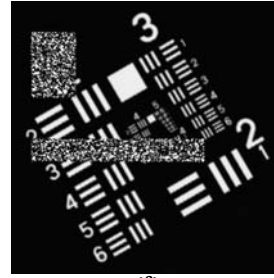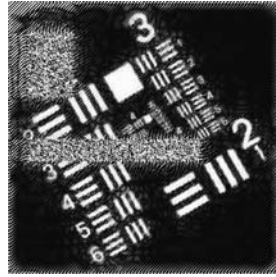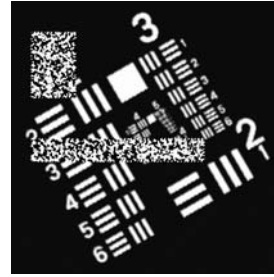
Fig. 6.9. Reconstructions from a severely corrupted hologram (top amplitude, bottom phase) for $d = 0$ m and $K_x = K_y = -1$. Algorithms from left to right: Fourier filtering and Fresnel transform, Fresnelet approximation, and LSE method.

Fourier filtering algorithm: The local defects deteriorate the reconstructed wave's quality well beyond their boundaries. The Fresnelet approximation shows slightly better visual results in several regions of the amplitude reconstruction because it allows for a better trade-off between space and frequency filtering. However, its overall quality is worse. The space selectivity is also insufficient to compete with the LSE method. The boundary conditions can be treated much more easily with the latter. The advantage of having a local procedure is striking: there are no artifacts.

It is even more interesting that the LSE procedure, since it is local, allows to reconstruct the phase only in certain regions of interest: There is no point in spending computational effort for retrieving the phase in areas where there is no hope of getting a sound result. The regions may also be user-defined and possibly tuned to the needs of
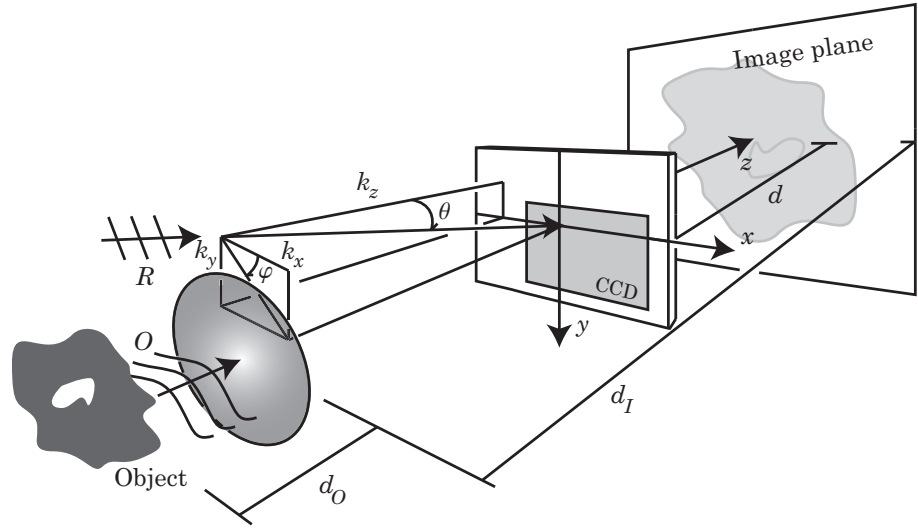
Fig. 6.10. Setup for digital holographic microscopy.

specific applications that don't require computing the amplitude and phase over the whole image. As an immediate consequence for the LSE algorithm, the computational cost drops proportionally to the surface of the region of interest.

6.5 Digital holographic Microscopy: Comparisons

In this Subsection, we investigate and compare the proposed algorithms in situations that contain a microscope objective. We consider that the object wave is magnified by a microscope objective. The model we use is as follows. We consider a general wavefront that is a function that has undergone free-space propagation (a Fresnel transform of parameter τ_1), is scaled by a factor s_1 and multiplied by a quadratic phase term of parameter $\rho_1 \in \mathbb{R}_+$:

$$g(x) = \frac{1}{\rho_1} e^{i\pi(x/\rho_1)^2} \tilde{f}_{\tau_1}\left(\frac{x}{s_1}\right).$$

(6.11)

Its Fresnel transform with parameter τ is again a function of the same form but with parameters τ_2, s_2, and ρ_2

$$\tilde{g}_\tau = \frac{1}{\rho_2} e^{i\pi(x/\rho_2)^2} \tilde{f}_{\tau_2}\left(\frac{x}{s_2}\right)$$

(6.12)

with $\rho_2^2 = \tau^2 + \rho_1^2$, $s_2 = s_1 \rho_2^2 / \rho_1^2$ and $\tau_2^2 = \left((\tau\rho_1)/(s_1\rho_2)\right)^2 + \tau_1^2$. In an ideal imaging system, the wavefront coming from the object undergoes free-space propagation over a distance d_O after which the lens introduces a quadratic phase shift (we consider an infinite aperture, thin
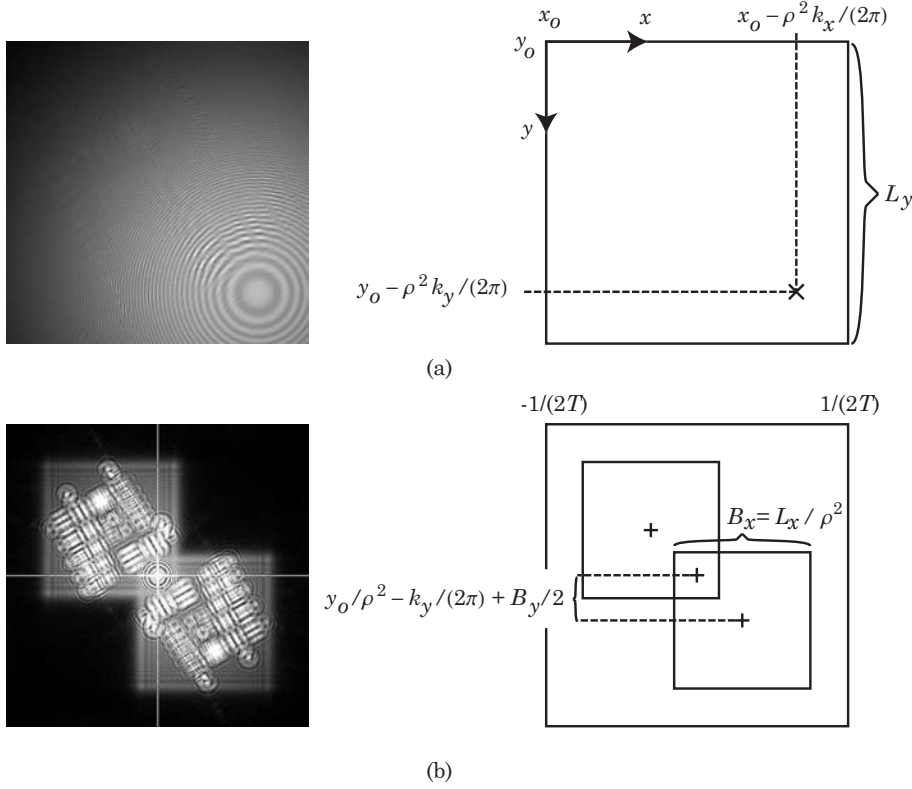
Fig. 6.11. Hologram spectrum in the presence of a lens. (a) Hologram, (b) Hologram spectrum.

lens). Just behind this ideal lens, the wavefront has the general form of Eq. (6.11) with parameters $\tau_1^2 = \lambda d_O$, $s_1 = 1$ (no scaling), $\rho_1 = -\lambda f$. It is easy to verify that the wave's three parameters at distance d_I from the lens, with the imaging condition:

$$\frac{1}{f} = \frac{1}{d_I} + \frac{1}{d_O} \tag{6.13}$$

and the definition of the magnification $\mathcal{M} = d_I/d_O > 0$ are $\tau_2 = 0$ (i.e. not defocus), $\rho_2^2 = \lambda \mathcal{M} f$ and $s_2 = -\mathcal{M}$.

If we put the camera at a distance d in front of the image plane, the wavefront is given by (using Eq. (6.11))

$$O(\mathbf{x}) = \exp\left(i\pi \frac{\|\mathbf{x}\|^2}{\rho^2}\right) \tilde{f}_{\sqrt{\lambda d'}}\left(\frac{\mathbf{x}}{-\mathcal{M}''}\right) \tag{6.14}$$

with

$$\pi D = \rho^2 = \lambda(\mathcal{M} f - d) \tag{6.15}$$

$$\mathcal{M}'' = \mathcal{M} - d/f \tag{6.16}$$

$$d' = d - \frac{d^2}{f\mathcal{M}}. \tag{6.17}$$
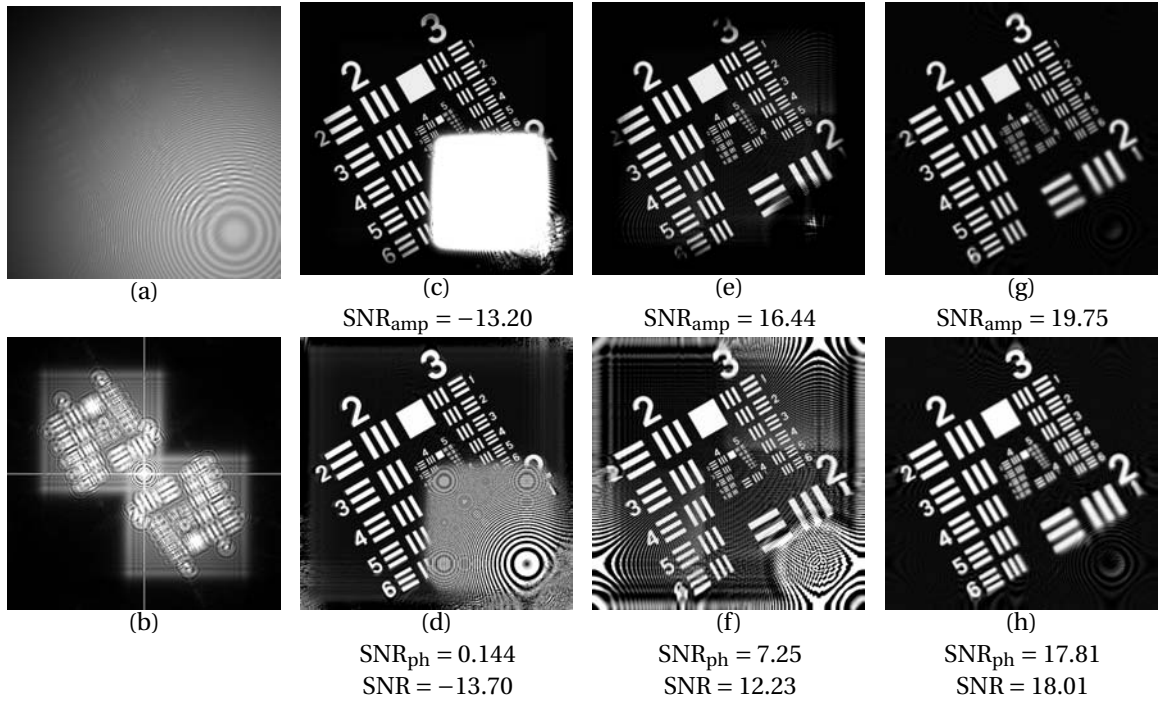
Fig. 6.12. Reconstructions from the hologram (a) with camera in front of image plane. (b) Hologram spectrum. Reconstructions with plain Fresnel transform (c) amplitude (d) phase, Fourier filtering and Fresnel transform (e), (f), LSE variable window-size least-squares method (g), (h). The following parameters were used: $d = 0.1$ m, $K_x = K_y = -1$, $D_x = D_y = \rho^2/(\pi T^2) = 350$, $X_0 = Y_0 = x_0/T = y_0/T = 250$. Maximal corresponding K-vector norm: 1.71.

If we put the camera at a distance d behind the image plane, we have

$$\pi D = \rho = \lambda(\mathcal{M}f + d) \tag{6.18}$$

$$\mathcal{M}'' = \mathcal{M} + d/f \tag{6.19}$$

$$d' = d + \frac{d^2}{f\mathcal{M}}. \tag{6.20}$$

The composition of the hologram's spectrum is radically different from the lensless case: the zero-order is localized around the frequency origin, whereas the ± 1 order terms spread across the frequency plane, which is visible in Fig. 6.11. The hologram is measured with a camera of dimensions $L_x \times L_y$. That is, we actually measure (the reasoning is done only for the x direction)

$$O'(x) = \text{rect}(x/L_x)O(x). \tag{6.21}$$

The approximate width of the spectrum (which may be calculated using the Heisenberg uncertainty relation for the Fourier, respectively Fresnel transform) is:

$$B_x = L_x/\rho^2. \tag{6.22}$$

If we consider the hologram obtained with a reference wave $R(\mathbf{x}) = \exp[i(k_x x + k_y y)]$ with the upper right corner positioned at location

0001110110

(a)   (c)   (e)   (g)

SNR_amp = −20.59   SNR_amp = 19.62   SNR_amp = 19.83

(b)   (d)   (f)   (h)

$\text{SNR}_{\text{ph}} = -10.14$ $\text{SNR}_{\text{ph}} = 12.15$ $\text{SNR}_{\text{ph}} = 18.19$

$\text{SNR} = -21.38$ $\text{SNR} = 16.51$ $\text{SNR} = 18.19$
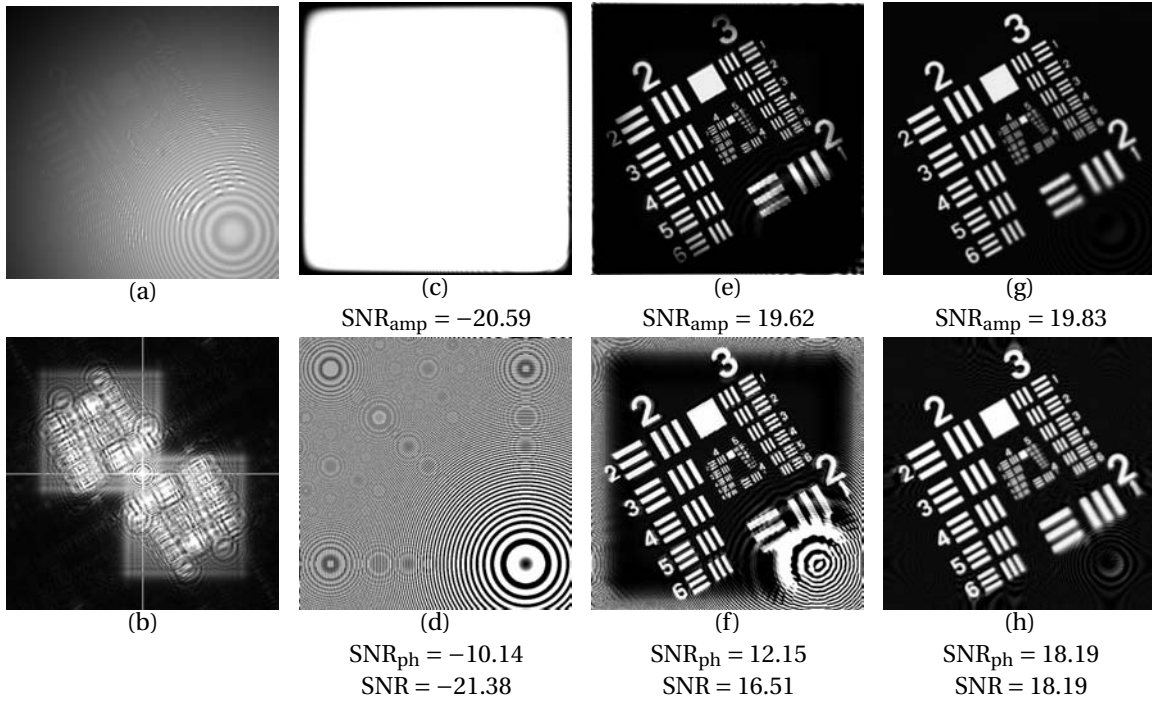
Fig. 6.13. Reconstructions from the hologram (a) with camera in the image plane. (b) Hologram spectrum. Reconstructions with plain Fresnel transform (c) amplitude (d) phase, Fourier filtering and Fresnel transform (e), (f), LSE variable window-size least-squares method (g), (h). The following parameters were used: $d = 0$ m, $K_x = K_y = -1$, $D_x = D_y = \rho^2/(\pi T^2) = 350$, $X_0 = Y_0 = x_0/T = y_0/T = 250$. Maximal corresponding K-vector norm: 1.71.

(x_0, y_0), the positions of the centers of the ± 1 order terms in the Fourier domain are

$$\pm\left(\frac{x_0 + L_x/2}{\rho^2} - \frac{k_x}{2\pi}\right). \tag{6.23}$$

This means that the use of the Fresnelet approximation procedure is no longer justified and we will therefore not include it in the forthcoming experiments.

For our next simulation, we consider a microscope objective, with a magnification $\mathcal{M} = 40\times$ and, assuming a normalized tube length $L_{\text{tube}} = 160$ mm, a focal length $f = L_{\text{tube}}/\mathcal{M} = 4$ mm.

We compare the plain Fresnel transform, the Fourier filtering and Fresnel transform, and the LSE phase estimation algorithms in two situations. In Fig. 6.12 the camera was placed at a distance $d = 0.1$ m in front of the image plane. The reconstruction is possible with the plain Fresnel transform. The zero-order term limits the field of view. The Fourier filtering method allows for the suppression of the zero-order term as well as of the twin image up to a certain point. In Fig. 6.13, the camera was placed in the image plane. The plain Fresnel transform cannot be used in this configuration. In both experiments, the LSE phase retrieval method gives much better results, both in terms of field of view as in terms of SNR.

Method	ChFFrT	Convolution	Fresnelet pyramid
Sampling step	$\lambda d/(NT)$	T	mT
Complexity	$L\log L$	$L\log L$	$L\log L$
Computation time 1	+++	+	++
Computation time 2 and more	++	+	+++
Space-frequency compromise	no	no	yes

TABLE 6.I

FRESNEL TRANSFORM IMPLEMENTATIONS COMPARISON. THE MORE +, THE BETTER.

6.6   Synthesis

In this Section, we synthesize the results and observations that we gathered in the previous section.

6.6.1   Fresnel Transforms

We have compared the ChFFrT and the Fresnelet pyramid approach to computing the Fresnel transform. While comparing the two methods in particular situations (i.e. the sampling step is the same) shows that they perform similarly, the Fresnelet pyramid approach is more flexible. In particular, the sampling step does not depend on the wavelength, the reconstruction distance or the number of samples. This is important for applications that reconstruct holograms of the same object obtained with different wavelengths since the reconstruction sampling step does not depend on the wavelength. The Fresnelet approach offers the advantage that it is a multiresolution procedure, therefore, it is particularly useful for removing the zero-order and twin image terms in certain situations. Table 6.I shows the principal characteristics of the different algorithms.

6.6.2   Digital Holography Methods

We have compared four digital hologram reconstruction methods in various situations. Table 6.II should allow help selecting the appropriate algorithm for a particular setup at hand.

0001111000

Method	Plain Fresnel transform	Fourier Method & Fresnel Transform	Fresnelet Approximation	Weighted window LSE & Fresnel Transform
Number of holograms	$1\ (2)^a$	1 (2)	1 (2)	1
Handles $d = 0$	no	yes	yes	yes
$k_{x,y}/(2\pi)\lambda d <$ support	no	yes	yes	yes
$k_x = k_y = 0$	no	no	no	no
Lens	yes	yes	no	yes
General reference	no	no	no	yes
Minimal Complexity $\mathcal{O}$	$L\log L$	$L\log L$	$L\log L$	$L\tilde{M}$
Processing time	+++	++	+	+ (+++ if $d = 0$)
Requ. params set before	no	no	no	yes
Get amplitude	$(\text{yes})^b$	(yes)	(yes)	yes
Suppresses Reflections	no	yes	yes	no
Nonlinear camera (harmonics)	no	yes	yes	yes
Local defects	+	+	+	+++
Regions of Interest	+	+	+	+++
Border Conditions	+	+	+	+++
Field of view	+	++	++	+++

TABLE 6.II

COMPARISON OF HOLOGRAM RECONSTRUCTION ALGORITHMS. THE MORE +, THE BETTER.

---

[a]To compensate amplitude.

[b]Requires a supplementary measurement.

6.7 Conclusion and Outlook

6.7.1 General Conclusion

In this thesis, we have explored the interplay between image processing, fringe analysis, and digital holography.

We have developed mathematical tools to carry the benefits of multiresolution image processing over to digital holography. We have proposed two applications that are based on Fresnelets. The non-linear space-frequency approximation procedure is able, for certain experimental configurations, to take advantage of the particular na-

0001111001

ture of holograms. The autofocus algorithm is based on the property that Fresnel holograms have a sparse representation in distance-dependent Fresnelet bases; it was shown to be effective on experimental data.

The least-square method (LSE) for the estimation of amplitude and phase has proved to be most flexible and reliable. Its results are highly satisfying, in particular regarding the field of view and the overall quality. However, such high quality reconstructions are only possible if an accurate a priori model of the reference wave is available before reconstruction. For lensless digital holography off-axis holography, the LSE method is of particular interest when the product between the distance and the fringes K-vector in the hologram plane is small or when the reference wave model is complicated.

6.7.2   Outlook for Future Research

The research presented here opens several interesting avenues for further investigations that we are now starting to explore. Some of them are listed below.

Fresnelet frames   The Fresnelet decomposition allows for the selective suppression of terms with good localization in both time and frequency. Using redundant decompositions into Fresnelet-frames (an over-complete family of functions) might allow to get a finer resolution in frequency. This is motivated by the fact that, in lensless holography, the frequencies are possibly well separated and the compromise between space and frequency may be tuned more selectively.

Automatic 3D particle localization   The autofocus method gives a means of deciding whether an image is well-focused. This principle might also be adapted to localize particles in 3D scenes with multiple focus planes.

Parameter estimation and compensation   Estimating the parameters remains the most delicate aspect of digital holography. This aspect should be further studied to allow for minimal user interaction during setup.

Phase unwrapping   The reconstructed phase may possibly exceed the domain $[-\pi, \pi)$ and therefore require 2D phase unwrapping. General algorithms [70] may be simplified if they included the a priori knowledge that parametric models carries. The same holds true for aberration compensation algorithms.

Fast implementations of the variable window size LSE algorithm
The variable window size least-squares algorithm requires the computation of weighted averages at every location where the complex wave is to be retrieved. If the window size is constant, this operation corresponds to a convolution. For certain weighting functions (i.e. B-splines), there exist fast methods for computing these convolutions [210]. This would allow for a faster implementation of the weighted (constant window size) least-squares algorithm.

Although this approach is only usable for fixed window sizes, we may still make use of it in the case of the variable window size algorithm. We compute the weighted averages at several resolutions (say over a couple of dyadic scales). When actually implementing the complex-wave retrieval at a particular point, we may either choose one of the weighted averages that corresponds to the right size, or we may combine the averages from two resolutions to yield an intermediary one, in a way similar to mipmaps in texture analysis.

Higher order models for the phase retrieval algorithm   One of the complex-wave retrieval algorithm's hypotheses is that the quantities to retrieve are constant over the neighborhood of the pixel of interest. Higher-order models could be considered.

Alternate norm minimization   The minimization in Eq. (4.4) is a least-squares minimization, which corresponds to a L_2 norm. We are working on methods to retrieve solutions that minimize generalized L_p-norms, in particular for $p = 1$. This should allow to overcome a typical drawback of least-squares fits, namely that a single outlier may completely corrupt the result.

Comparison with other phase retrieval algorithms   There exist a wide range of phase retrieval algorithms that are able to demodulate interferograms with closed fringes [114, 115, 188]. It would be instructive to compare these algorithms with the approach we propose in Chapter 4.

Extend the experiments   It is only recently that phase retrieval techniques have been generalized to be applied in conjunction with white light microscopy [6, 29, 115]. These methods aim at using white light illumination to retrieve phase information using specific assumptions and techniques (phase gradient, transport of energy equation).

The phase retrieval algorithm we have presented may be generalized to higher dimensions (e.g. several holograms). This supplementary information may be used to solve interferometry problems in more general situations, e.g. white light, low coherence.

Furthermore, the algorithm is suitable for even more general setups than those containing lenses. More general reference waves, for example, generated by the light's diffraction by a single point or slit, may be considered. This may possibly permit to relax the requirements on the light source's (temporal) coherence. In particular, a configuration for three-dimensional holographic micro-imaging at visible, ultraviolet and X-ray wavelength that would fit into this model is that proposed by Boyer *et al.* [22].

0001111100

Acknowledgments

The work presented in this thesis could not have been completed without the help of many others.

First of all, I would like to thank my thesis advisor, Prof. Michael Unser, for having proposed this subject to me and for his constant encouragement and support. His constructive criticism was always highly motivating.

My deep gratitude and appreciation goes to Prof. René Salathé, Dr. Christian Depeursinge, Prof. René Dändliker, Prof. Thierry Fournel, and Prof. Martin Vetterli who kindly accepted to be on my thesis committee and have given me feedback both in optics and signal processing during the past years.

I was very fortunate to work with Thierry Blu who provided crucial insights and with whom I greatly appreciated to interact.

I would like to thank Etienne Cuche, Pierre Marquet, Tristan Colomb, and Frédéric Montfort with whom I had the privilege to collaborate and who provided all the experimental hologram data.

I gratefully acknowledge inspiring conversations with Professors Jean-Marc Fournier, Theo Lasser, and Giorgio Margaritondo.

Thanks are due to present and former BIG members, Daniel, Philippe, Mathews, Brigitte, Dimitri, Muthuvel, Ildar, Rajesh, Michael Sühling, Shai, Manuela, Stefan, Slavica, Jan, Arrate, Nadja, Julien, Emilio, Carlos Óscar, Koichi, Jean-Martial, Maria, Gloria, Erik, and secretaries, Martine Peter, Manuelle Borruat and Yvette Bernhard.

Last, but certainly not least, I would like to thank my family, my wife Maeva, my mother, my father, my sister Carolina, for everything.

0001111110

Bibliography

[1] M. Afifi, A. Fassi-Fihri, M. Marjane, K. Nassim, M. Sidki, and S. Rachafi, "Paul wavelet-based algorithm for optical phase distribution evaluation," *Opt. Commun.*, vol. 211, pp. 47–51, Oct. 2002.

[2] E. Allaria, S. Brugioni, S. De Nicola, P. Ferraro, S. Grilli, and R. Meucci, "Digital holography at 10.6 μm," *Opt. Commun.*, vol. 215, no. 4–6, pp. 257–262, Jan. 2003.

[3] J. P. Allebach, N. C. Gallagher, and B. Liu, "Aliasing error in digital holography," *Appl. Opt.*, vol. 15, no. 9, pp. 2183–2188, Sept. 1976.

[4] J. P. Allebach and B. Liu, "Minimax spectrum shaping with a bandwidth constraint," *Appl. Opt.*, vol. 14, no. 12, pp. 3062–3072, Dec. 1975.

[5] R. G. Baraniuk and D. L. Jones, "Unitary equivalence—a new twist on signal-processing," *IEEE Trans. Signal Process.*, vol. 43, no. 10, pp. 2269–2282, Oct. 1995.

[6] A. Barty, K. A. Nugent, D. Paganin, and A. Roberts, "Quantitative optical phase microscopy," *Opt. Lett.*, vol. 23, no. 11, pp. 817–819, June 1998.

[7] M. J. Bastiaans, "Gabor expansion of a signal into Gaussian elementary signals," *Proc. IEEE*, vol. 68, no. 4, pp. 538–539, 1980.

[8] G. Battle, "A block spin construction of ondelettes. 1. Lemarié functions," *Comm. Math. Phys.*, vol. 110, no. 4, pp. 601–615, 1987.

[9] ——, "Spherically harmonic Huygen wavelets," *Appl. Comput. Harmon. Anal.*, vol. 2, no. 2, pp. 154–159, Apr. 1995.

[10] S. A. Benton, "Hologram reconstructions with extended incoherent sources," *J. Opt. Soc. Amer.*, vol. 59, no. 11, pp. 1545–1546, 1969.

[11] S. A. Benton and M. Halle, "Computational holography for biomedical imaging," in *Technology Requirements for Biomedical Imaging. Proceedings.* IEEE, May 21–22, 1991.

[12] M. Bhatia, W. C. Karl, and A. S. Willsky, "A wavelet-based method for multiscale tomographic reconstruction," *IEEE Trans. Med. Imag.*, vol. 15, no. 1, pp. 92–101, Feb. 1996.

[13] Th. Blu and M. Unser, "Quantitative Fourier analysis of approximation techniques: Part II—Wavelets," *IEEE Trans. Signal Process.*, vol. 47, no. 10, pp. 2796–2806, Oct. 1999.

[14] ——, "The fractional spline wavelet transform: Definition and implementation," in *Proceedings of the Twenty-Fifth IEEE International Conference on Acoustics, Speech, and Signal Processing (ICASSP'00)*, vol. I, Istanbul, Turkey, June 5–9 2000, pp. 512–515.

[15] A. M. S. Boethius, *Fundamentals of Music*, C. V. Palisca, Ed. New Haven: Yale Univ. Press, 1989, translated by C. M. Bower.

0001111111

[16] A. M. T. S. Boetii, *De institutione musica*, ser. Bibliotheca scriptorum Græcorum et Romanorum Teubneriana, G. Friedlein, Ed. Hildesheim, Germany: Teubner, 1867.

[17] A. M. S. Boetius, *Fünf Bücher über die Musik*. Hildesheim, Germany: Georg Olms Verlag, 1985, German translation.

[18] D. J. Bone, H.-A. Bachor, and R. J. Sandeman, "Fringe-pattern analysis using a 2-D Fourier transform," *Appl. Opt.*, vol. 25, no. 10, pp. 1653–1660, May 1986.

[19] S. Bonnet, F. Peyrin, F. Turjman, and R. Prost, "Multiresolution reconstruction in fan-beam tomography," *IEEE Trans. Image Process.*, vol. 11, no. 3, pp. 169–176, Mar. 2002.

[20] M. Born and E. Wolf, *Principles of Optics, 7th (expanded) edition.* Cambridge University Press, 1999.

[21] T. Bothe, J. Burke, and H. Helmers, "Spatial phase shifting in electronic speckle pattern interferometry: minimization of phase reconstruction errors," *Appl. Opt.*, vol. 36, no. 22, pp. 5310–5316, Aug. 1997.

[22] K. Boyer, J. C. Solem, J. W. Longworth, A. B. Borisov, and C. K. Rhodes, "Biomedical three-dimensional holographic microimaging at visible, ultraviolet and x-ray wavelengths," *Nat. Med.*, vol. 2, no. 8, pp. 939–941, 1996.

[23] R. T. Brigantic, M. C. Roggemann, K. W. Bauer, and B. M. Welsh, "Image-quality metrics for characterizing adaptive optics system performance," *Appl. Opt.*, vol. 36, no. 26, pp. 6583–6593, Sept. 1997.

[24] C. Buraga-Lefebvre, S. Coetmellec, D. Lebrun, and C. Ozkul, "Application of wavelet transform to hologram analysis: three- dimensional location of particles," *Opt. Lasers Eng.*, vol. 33, no. 6, pp. 409–421, 2000.

[25] P. H. Chan, P. J. Bryanston-Cross, and S. C. Parker, "Fringe-pattern analysis using a spatial phase-stepping method with automatic phase unwrapping," *Meas. Sci. Technol.*, vol. 6, no. 9, pp. 1250–1259, Sept. 1995.

[26] M. Cherbuliez, "Wavelet analysis of interference patterns and signals: development of fast and efficient processing techniques," Ph.D. dissertation, no. 2377, École Polytechnique Fédérale de Lausanne, 2001.

[27] M. Cherbuliez, P. Jacquot, and X. C. de Lega, "Wavelet processing of interferometric signals and fringe patterns," in *Wavelet Applications in Signal and Image Processing VII*, M. A. Unser, A. Aldroubi, and A. F. Laine, Eds., vol. 3813. Proc. SPIE, 1999, pp. 692–702.

[28] F. N. Chukhovskii, D. V. Novikov, T. Hiort, and G. Materlik, "Electron charge density imaging with X-ray holography," *Opt. Commun.*, vol. 209, no. 4–6, pp. 273–277, Aug. 2002.

[29] C.J. Cogswell, N. I. Smith, K. G. Larkin, and Hariharan P., "Quantitative DIC microscopy using a geometric phase shifter," in *Three-dimensional Microscopy: Image Acquisition and Processing IV*, C. J. Cogswell, J.-A. Conchello, and T. Wilson, Eds., vol. 2984. Proc. SPIE, 1997, pp. 72–81.

[30] R. R. Coifman and Y. Meyer, "Gaussian bases," *Appl. Comput. Harmon. Anal.*, vol. 2, no. 3, pp. 299–302, July 1995.

0010000000

[31] T. Colomb, E. Cuche, P. Dahgren, A. M. Marian, F. Montfort, Ch. D. Depeursinge, P. Marquet, and P. J. Magistretti, "3D imaging of surfaces and cells by numerical reconstruction of wavefronts in digital holography applied to transmission and reflection microscopy," in *Proceedings of the First 2002 IEEE International Symposium on Biomedical Imaging: Macro to Nano (ISBI'02)*, Washington DC, USA, July 7–10 2002, pp. 773–776.

[32] T. Colomb, P. Dahlgren, D. Beghuin, E. Cuche, P. Marquet, and Ch. Depeursinge, "Polarization imaging by use of digital holography," *Appl. Opt.*, vol. 41, no. 1, pp. 27–37, Jan. 2002.

[33] J. W. Cooley and J. W. Tukey, "An algorithm for machine calculation of complex fourier series," *Math. Comput.*, vol. 19, pp. 297–301, 1965.

[34] O. Coquoz, R. Conde, F. Taleblou, and Ch. Depeursinge, "Performances of endoscopic holography with a multicore opticalfiber," *Appl. Opt.*, vol. 34, no. 31, pp. 7186–7193, Nov. 1995.

[35] K. Creath and J. Schmit, "N-point spatial phase-measurement techniques for non-destructive testing," *Opt. Lasers Eng.*, vol. 24, no. 5–6, pp. 365–379, 1996.

[36] E. Cuche, F. Bevilacqua, and Ch. Depeursinge, "Digital holography for quantitative phase-contrast imaging," *Opt. Lett.*, vol. 24, no. 5, pp. 291–293, Mar. 1999.

[37] E. Cuche, P. Marquet, and Ch. Depeursinge, "Simultaneous amplitude-contrast and quantitative phase-contrast microscopy by numerical reconstruction of Fresnel off-axis holograms," *Appl. Opt.*, vol. 38, no. 34, pp. 6994–7001, Dec. 1999.

[38] ——, "Spatial filtering for zero-order and twin-image elimination in digital off-axis holography," *Appl. Opt.*, vol. 39, no. 23, pp. 4070–4075, Aug. 2000.

[39] Etienne Cuche, "Numerical reconstruction of digital holograms : application to phase-contrast imaging and microscopy," Ph.D. dissertation, no. 2182, École Polytechnique Fédérale de Lausanne, Lausanne, 2000.

[40] L. De Broglie, *Optique électronique et corpusculaire.* Paris: Hermann, 1950.

[41] S. De Nicola, P. Ferraro, A. Finizio, and G. Pierattini, "Wave front reconstruction of Fresnel off-axis holograms with compensation of aberrations by means of phase-shifting digital holography," *Opt. Lasers Eng.*, vol. 37, no. 4, pp. 331–340, Dec. 2002.

[42] N. Delprat, B. Escudié, P. Guillemain, R. Kronland-Martinet, P. Tchamitchian, and B. Torrésani, "Asymptotic wavelet and Gabor analysis—Extraction of instantaneous frequencies," *IEEE Trans. Inf. Theory*, vol. 38, no. 2, pp. 644–664, Mar. 1992.

[43] N. Demoli, J. Meštrović, and I. Sović, "Subtraction digital holography," *Appl. Opt.*, vol. 42, no. 5, pp. 798–804, Feb. 2003.

[44] D. L. Donoho, "Superresolution via sparsity constraints," *SIAM J. Math Analysis*, vol. 23, no. 5, pp. 1309–1331, Sept. 1992.

[45] D. L. Donoho and I. M. Johnstone, "Ideal spatial adaptation by wavelet shrinkage," *Biometrika*, vol. 81, no. 3, pp. 425–455, Sept. 1994.

[46] D. L. Donoho, M. Vetterli, R. A. DeVore, and I. Daubechies, "Data compression and harmonic analysis," *IEEE Trans. Inf. Theory*, vol. 44, no. 6, pp. 2435–2476, 1998.

[47] S. J. Erasmus and K. C. A. Smith, "An automatic focusing and astigmatism correction system for the SEM and CTEM," *J. Microscopy*, vol. 127, pp. 185–199, Aug. 1982.

[48] A. Erteza, "Sharpness index and its application to focus control," *Appl. Opt.*, vol. 15, pp. 877–881, 1976.

[49] A. K. Evans, "Resolution limits and noise reduction in digital holographic microscopy," in *Practical Holography XVI And Holographic Materials VIII*, vol. 4659.   Proc. SPIE, 2002, pp. 35–43.

[50] A. Federico and G. H. Kaufmann, "Comparative study of wavelet thresholding methods for denoising electronic speckle pattern interferometry fringes," *Opt. Eng.*, vol. 40, no. 11, pp. 2598–2604, Nov. 2001.

[51] ——, "Evaluation of the continuous wavelet transform method for the phase measurement of electronic speckle pattern interferometry fringes," *Opt. Eng.*, vol. 41, no. 12, pp. 3209–3216, Dec. 2002.

[52] P. Ferraro, G. Coppola, S. De Nicola, A. Finizio, and G. Pierattini, "Digital holographic microscope with automatic focus tracking by detecting sample displacement in real time," *Opt. Lett.*, vol. 28, no. 14, pp. 1257–1259, July 2003.

[53] P. Ferraro, S. De Nicola, A. Finizio, G. Coppola, S. Grilli, C. Magro, and G. Pierattini, "Compensation of the inherent wave front curvature in digital holographic coherent microscopy for quantitative phase-contrast imaging," *Appl. Opt.*, vol. 42, no. 11, pp. 1938–1946, Apr. 2003.

[54] D. J. Field, "Relations between the statistics of natural images and the response properties of cortical cells," *J. Opt. Soc. Am. A*, vol. 4, no. 12, pp. 2379–2394, 1987.

[55] J. R. Fienup, "Invariant error metrics for image reconstruction," *Appl. Opt.*, vol. 36, no. 32, pp. 8352–8357, Nov. 1997.

[56] ——, "Synthetic-aperture radar autofocus by maximizing shapness," *Opt. Lett.*, vol. 25, no. 4, pp. 221–223, Feb. 2000.

[57] J. R. Fienup and J. J. Miller, "Aberration correction by maximizing generalized sharpness metrics," *J. Opt. Soc. Am. A*, vol. 20, no. 4, pp. 609–620, Apr. 2003.

[58] A. Fresnel, *Œuvres complètes d'Augustin Fresnel*, H. De Sernamont, É. Verdet, and L. Fresnel, Eds.   Paris: Imprimerie Impériale, 1866.

[59] E. Freysz, B. Pouligny, F. Argoul, and A. Arneodo, "Optical wavelet transform of fractal aggregates," *Phys. Rev. Lett.*, vol. 64, no. 7, pp. 745–748, Feb. 1990.

[60] L. Froehly, S. Nieto Martin, Th. Lasser, Ch. Depeursinge, and F. Lang, "Multiplexed 3D imaging using wavelength encoded spectral interferometry: a proof of principle," *Opt. Commun.*, vol. 222, no. 1–3, pp. 127–136, Aug. 2003.

[61] D. Gabor, "Theory of communication," *J. Inst. Elect. Eng. (London)*, vol. 93, pp. 429–457, 1946.

[62] ——, "A new microscopic principle," *Nature*, vol. 161, no. 4098, pp. 777–778, May 1948.

0010000010

[63] ——, "Microscopy by reconstructed wave-fronts," *Proc. R. Soc. London A*, vol. 197, no. 1051, pp. 454–487, 1949.

[64] ——, "Microscopy by reconstructed wave fronts: II," *Proc. Phys. Soc. London B*, vol. 64, no. 378, pp. 449–469, 1951.

[65] F. Gaffiot, *Dictionnaire latin-français: Le grand Gaffiot.* Paris: Hachette, 2000.

[66] L. Gagnon, "Wavelet filtering of speckle noise—some numerical results," in *Proceedings of the Conference Vision Interface*, Trois-Rivières, Canada, 1999, pp. 80–91.

[67] L. Gagnon and A. Jouan, "Speckle filtering of SAR images—a comparative study between complex-wavelet-based and standard filters," in *Wavelet Applications in Signal and Image Processing V*, A. Aldroubi, Laine A. F., and Unser M. A., Eds., vol. 3169, 1997, pp. 80–91.

[68] J. Gass, A. Dakoff, and M. K. Kim, "Phase imaging without 2π ambiguity by multiwavelength digital holography," *Opt. Lett.*, vol. 28, no. 13, pp. 1141–1143, July 2003.

[69] C. F. Gauss, "Theoria combinationis observationum erroribus minimis obnoxiæ," *Royal Society of Göttingen*, 1821(1995), Reprinted by SIAM Classics in Applied Mathematics, English translation by G. W. Stewart.

[70] D. C. Ghiglia and M. D. Pritt, *Two-dimensional phase unwrapping.* New York: Wiley, 1998.

[71] J. Gillespie and R. A. King, "The use of self-entropy as a focus measure in digital holography," *Pattern Recognition Lett.*, vol. 9, no. 1, pp. 19–25, Jan. 1989.

[72] J. W. Goodman, *Introduction to Fourier Optics*, 2nd ed. New York: McGraw-Hill, 1996.

[73] J. W. Goodman and R. W. Lawrence, "Digital image formation from electronically detected holograms," *Appl. Phys. Lett.*, vol. 11, no. 3, pp. 77–79, Aug. 1967.

[74] J. E. Greivenkamp and J. H. Bruning, "Phase shifting interferometry," in *Optical Shop Testing, 2nd ed.*, D. Malacara, Ed. Wiley, 1992, pp. 501–598.

[75] F. C. A. Groen, I. T. Young, and G. Ligthart, "A comparison of different focus functions for use in autofocus algorithms," *Cytometry*, vol. 6, no. 2, pp. 81–91, 1985.

[76] P. Grossman, "Depth from focus," *Pattern Recognition Lett.*, vol. 5, pp. 63–69, Jan. 1987.

[77] M. Hájek, "Conservative iterative Fourier transform algorithms in digital holography," in *Workshop on Digital Holography*, F. Wyrowski, Ed., vol. 1718. Proc. SPIE, 1993, pp. 63–68.

[78] H. Hamam, "Simplified linear formulation of Fresnel diffraction," *Opt. Commun.*, vol. 144, pp. 89–98, Dec. 1997.

[79] H. Hamam and J.L de Bougrenet de la Tocnaye, "Efficient Fresnel-transform algorithm based on fractional Fresnel diffraction," *J. Opt. Soc. Am. A*, vol. 12, no. 9, pp. 1920–1931, Sept. 1995.

[80] E. Heindl and R. Meyer, "Optimized reconstruction of electron holograms using the simplex algorithmus," in *European Conference on Microscopy, EUREM96 CD:/T/T14/Rec_op.pdf*, 1996.

[81] W. Heisenberg, "Über den anschaulichen inhalt der quantentheoretischen kinematik und mechanik," *Zeitschrift f. Physik*, vol. 43, pp. 172–198, 1927.

[82] K. Hibino, B. F. Oreb, D. I. Farrant, and K. G. Larkin, "Phase-shifting algorithms for nonlinear and spatially nonuniform phase shifts," *J. Opt. Soc. Am. A*, vol. 14, no. 4, pp. 918–930, Apr. 1997.

[83] P. R. Hobson and J. Watson, "The principles and practice of holographic recording of plankton," *J. Opt. A: Pure Appl. Opt.*, vol. 4, pp. 34–49, July 2002.

[84] G. M. Hoover, "Acoustical holography using digital processing," *Geophysics*, vol. 37, no. 1, pp. 1–19, Feb. 1972.

[85] S. Horbelt, M. Liebling, and M. Unser, "Discretization of the Radon transform and of its inverse by spline convolutions," *IEEE Trans. Med. Imag.*, vol. 21, no. 4, pp. 363–376, Apr. 2002.

[86] B. Horn, "Project MAC: Focusing," Massachusetts Institute of Technology, Mass., USA, MIT Artificial Intelligence Memo 160, 1968. [Online]. Available: ftp://publications.ai.mit.edu/ai-publications/pdf/AIM-160.pdf

[87] Ch. H. D. Z Huygens, *Traité de la lumière, où sont expliquées les causes de ce qui luy arrive dans la réflexion, & dans la réfraction, et particulièrement dans l'étrange réfraction du cristal d'Islande.* Bruxelles: Culture et Civilisation, 1967(1690), the ideas had been communicated to the Académie des Sciences in 1678.

[88] Y. Ichioka and M. Inuiya, "Direct phase detecting system," *Appl. Opt.*, vol. 11, no. 7, pp. 1507–1514, July 1972.

[89] G. Indebetouw and P. Klysubun, "Spatiotemporal digital microholography," *J. Opt. Soc. Am. A*, vol. 18, no. 2, pp. 319–325, Feb. 2001.

[90] *JPEG2000 Image Coding System, ITU-T Recommend. T.800-ISO/IEC FCD15444-1, ISO/IEC JTC1 SC29/WG1*, International Organization for Standardization, 2000.

[91] K. Ishizuka, "Optimized sampling schemes for off-axis holography," *Ultramicroscopy*, vol. 52, no. 1, pp. 1–5, Sept. 1993.

[92] ——, "Number of sampling points required for aberration correction using off-axis electron holography," *Ultramicroscopy*, vol. 53, no. 3, pp. 297–303, Mar. 1994.

[93] M. Jacquot, P. Sandoz, and G. Tribillon, "High resolution digital holography," *Opt. Commun.*, vol. 190, no. 1–6, pp. 87–94, Apr. 2001.

[94] A. J. E. M. Janssen, "Gabor representation of generalized functions," *J. Math. Anal. Appl.*, vol. 83, pp. 377–394, Oct. 1981.

[95] R. A. Jarvis, "Focus optimization criteria for computer image-processing," *Microscope*, vol. 24, no. 2, pp. 163–180, 1976.

[96] E. W. Justh, M. A. Vorontsov, G. W. Carhart, L. A. Beresnev, and P. S. Krishnaprasad, "Adaptive optics with advanced phase-contrast techniques. II. high-resolution wave-front control," *J. Opt. Soc. Am. A*, vol. 18, no. 6, pp. 1300–1311, June 2001.

[97] G. Kaiser, "Wavelet electrodynamics," *Phys. Lett. A*, vol. 168, no. 1, pp. 28–34, Aug. 1992.

0010000100

[98] G. H. Kaufmann and G. E. Galizzi, "Speckle noise reduction in television holography fringes using wavelet thresholding," *Opt. Eng.*, vol. 35, no. 1, pp. 9–14, Jan. 1996.

[99] K. Khare and N. George, "Direct coarse sampling of electronic holograms," *Opt. Lett.*, vol. 28, no. 12, pp. 1004–1006, June 2003.

[100] M. K. Kim, "Tomographic three-dimensional imaging of a biological specimen using wavelength-scanning digital interference holography," *Opt. Express*, vol. 7, no. 9, pp. 305–310, Oct. 2000.

[101] G. Kirchhoff, *Gesammelte Abhandlungen, Nachtrag*. Leipzig: Johann Ambrosius Barth, 1891.

[102] I. Kodama, M. Yamaguchi, N. Ohyama, T. Honda, K. Shinohara, A. Ito, T. Matsumura, K. Kinoshita, and K. Yada, "Image reconstruction from an in-line X-ray hologram with intensity distribution constraint," *Opt. Commun.*, vol. 125, no. 1–3, pp. 36–42, Apr. 1996.

[103] Th. Kreis, "Digital holographic interference-phase measurement using the Fourier-transform method," *J. Opt. Soc. Am. A*, vol. 3, no. 6, pp. 847–855, June 1986.

[104] ——, "Computer-aided evaluation of holographic interferograms," in *Holographic Interferometry, Principles and Methods*, P. K. Rastogi, Ed. Heidelberg, Germany: Springer, 1994, pp. 151–212.

[105] ——, *Holographic Interferometry*, ser. Series in optical metrology. Berlin: Akademie Verlag, 1996, vol. 1.

[106] Th. Kreis and W. P. O. Jüptner, "Suppression of the dc term in digital holography," *Opt. Eng.*, vol. 36, no. 8, pp. 2357–2360, Aug. 1997.

[107] Th. M. Kreis, "Frequency analysis of digital holography," *Opt. Eng.*, vol. 41, no. 4, pp. 771–778, Apr. 2002.

[108] Th. M. Kreis, M. Adams, and W. P. O. Jüptner, "Methods of digital holography: A comparison," in *Optical Inspection and Micromeasurements II*, C. Gorecki, Ed., vol. 3098. Proc. SPIE, 1997, pp. 224–233.

[109] M. A. Kronrod, N. S. Merzlyakov, and L.P. Yaroslavskii, "Reconstruction of a hologram with a computer," *Sov. Phys. Tech. Phys.*, vol. 17, no. 2, pp. 333–334, Aug. 1972.

[110] M. Kujawinska, "Spatial phase measurement methods," in *Interferogram analysis: digital fringe pattern measurement techniques*, D. W. Robinson and G. T. Reid, Eds. Bristol: Bristol Institute of Physics Publishing, 1993, pp. 141–193.

[111] M. Kujawińska and J. Wójciak, "Spatial phase-shifting techniques of fringe pattern analysis in photomechanics," in *Moiré Techniques, Holographic Interferometry, Optical NDT, and Applications to Fluid Mechanics, Parts 1 and 2*, F. P. Chiang, Ed., vol. 1554B. Proc. SPIE, 1991, pp. 503–513.

[112] R. Kumar, S. K. Singh, and C. Shakher, "Wavelet filtering applied to time-average digital speckle pattern interferometry fringes," *Opt. Laser Technol.*, vol. 33, pp. 557–571, 2001.

[113] G. Lai and T. Yatagai, "Generalized phase-shifting interferometry," *J. Opt. Soc. Am. A*, vol. 8, no. 5, pp. 822–827, May 1991.

[114] K. G. Larkin, "Natural demodulation of two-dimensional fringe patterns. II. Stationary phase analysis of the spiral phase quadrature transform," *J. Opt. Soc. Am. A*, vol. 18, no. 8, pp. 1871–1881, Aug. 2001.

[115] K. G. Larkin, D. J. Bone, and M. A. Oldfield, "Natural demodulation of two-dimensional fringe patterns. I. General background of the spiral phase quadrature transform," *J. Opt. Soc. Am. A*, vol. 18, no. 8, pp. 1862–1870, Aug. 2001.

[116] F. Le Clerc, L. Collot, and M. Gross, "Numerical heterodyne holography with two-dimensional photodetector arrays," *Opt. Lett.*, vol. 25, no. 10, pp. 716–718, May 2000.

[117] D. Lebrun, S. Belaïd, and C. Özkul, "Hologram reconstruction by use of optical wavelet transform," *Appl. Opt.*, vol. 38, no. 17, pp. 3730–3734, June 1999.

[118] H. Lee and G. Wade, "Sampling in digital holographic reconstruction," *J. Acoust. Soc. Amer.*, vol. 75, no. 4, pp. 1291–1293, Apr. 1984.

[119] M. Lehmann, "Determination and correction of the coherent wave aberration from a single off-axis electron hologram by means of a genetic algorithm," *Ultramicroscopy*, vol. 85, no. 3, pp. 165–182, Nov. 2000.

[120] M. Lehmann and H. Lichte, "Tutorial on off-axis electron holography," *Microsc. microanal.*, vol. 8, pp. 447–466, 2002.

[121] E. N. Leith, K. D. Mills, L. Deslaurier, S. Grannell, B. G. Hoover, D. S. Dilworth, H. Chen, M. Shih, J. Lopez, and B. D. Athey, "Information optics concepts applied to image formation in highly scattering media," in *Optical Processing and Computing: A tribute to Adolf Lohmann*, D. P. Casasent, H. J. Caulfield, W. J. Dallas, and H. H. Szu, Eds., vol. 4392. Proc. SPIE, 2001, pp. 1–8.

[122] E. N. Leith, J. Upatniek, and A. V. Lugt, "Hologram microscopy and lens aberration compensation by use of holograms," *J. Opt. Soc. Amer.*, vol. 55, no. 5, pp. 595–&, 1965.

[123] E. N. Leith and J. Upatnieks, "Reconstructed wavefronts and communication theory," *J. Opt. Soc. Amer.*, vol. 52, no. 10, pp. 1123–1130, Oct. 1962.

[124] P. G. Lemarié-Rieusset, "Ondelettes à localisation exponentielle," *J. Math. Pures Appl. (9)*, vol. 67, no. 3, pp. 227–236, 1988.

[125] Y. Li, H. H. Szu, Y. L. Sheng, and H. J. Caulfield, "Wavelet processing and optics," *Proc. IEEE*, vol. 84, pp. 720–732, 1996.

[126] H. Lichte, "Optimum focus for taking electron holograms," *Ultramicroscopy*, vol. 38, pp. 13–22, 1991.

[127] M. Liebling, Th. Blu, and M. Unser, "Fresnelets: new multiresolution wavelet bases for digital holography," *IEEE Trans. Image Process.*, vol. 12, no. 1, pp. 29–43, Jan. 2003.

[128] ——, "Non-linear Fresnelet approximation for interference term suppression in digital holography," in *Wavelets: Applications in Signal and Image Processing X*, M. A. Unser, A. Aldroubi, and A. F. Laine, Eds., vol. 5207. San Diego CA, USA: Proc. SPIE, August 3–8, 2003, pp. 553–559.

[129] ——, "Complex-wave retrieval from a single off-axis hologram," *J. Opt. Soc. Am. A*, vol. 21, no. 3, pp. 367–377, Mar. 2004.

[130] M. Liebling and M. Unser, "Autofocus for digital Fresnel holograms by use of a Fresnelet-sparsity criterion," *submitted to J. Opt. Soc. Am. A*, 2004.

[131] J. A. Lin and J. M. Cowley, "Reconstruction from in-line electron holograms by digital processing," *Ultramicroscopy*, vol. 19, no. 2, pp. 179–190, 1986.

[132] E. H. Linfoot, "Transmission factors and optical design," *J. Opt. Soc. Amer.*, vol. 46, no. 9, pp. 740–752, 1956.

[133] C. Liu, Y. Li, X. Cheng, Z. Liu, F. Bo, and J Zhu, "Elimination of zero-order diffraction in digital holography," *Opt. Eng.*, vol. 41, no. 10, pp. 2434–2437, Oct. 2002.

[134] C. Liu, Z. G. Liu, F. Bo, Y. Wang, and J. Q. Zhu, "Digital holographic aberration compensation in electron holography," *Opt. Eng.*, vol. 42, no. 3, pp. 651–655, Mar. 2003.

[135] A. W. Lohmann, D. Mendlovic, and Z. Zalevsky, "Digital method for measuring the focus error," *Appl. Opt.*, vol. 36, no. 28, pp. 7204–7209, Oct. 1997.

[136] C. López-Martínez and Fàbregas, "Modeling and reduction of SAR interferometric phase noise in the wavelet domain," *IEEE Trans. Geosci. Rem. Sens.*, vol. 40, no. 12, pp. 2553–2566, Dec. 2002.

[137] W. W. Macy, Jr., "Two-dimensional fringe-pattern analysis," *Appl. Opt.*, vol. 22, no. 23, pp. 3898–3901, Dec. 1983.

[138] T. H. Maiman, "Stimulated optical radiation in ruby," *Nature*, vol. 187, no. 4736, pp. 493–494, 1960.

[139] S. G. Mallat, "A theory for multiresolution signal decomposition—the wavelet representation," *IEEE Trans. Pattern Anal. Mach. Intell.*, vol. 11, no. 7, pp. 674–693, July 1989.

[140] A. Marian, E. Cuche, and Ch. Depeursinge, "Point spread function model for microscopic image deconvolution in digital holographic microscopy," in *Novel Optical Instrumentation for Biomedical Applications*, A.-C. Boccara, Ed., vol. 5143. Proc. SPIE, 2003, pp. 202–209.

[141] J. L. Marroquin, R. Rodriguez-Vera, and M. Servin, "Local phase from local orientation by solution of a sequence of linear systems," *J. Opt. Soc. Am. A*, vol. 15, no. 6, pp. 1536–1544, June 1998.

[142] J. L. Marroquin, M. Servin, and R. Rodriguez-Vera, "Adaptive quadrature filters and the recovery of phase from fringe pattern images," *J. Opt. Soc. Am. A*, vol. 14, no. 8, pp. 1742–1753, Aug. 1997.

[143] P. Massatsch, "Low coherence digital holographic microscopy: applications to vision in turbid media and biomedical imaging," Ph.D. dissertation, no. 2797, École Polytechnique Fédérale de Lausanne, Lausanne, 2003.

[144] A. C. McBride and F. H. Kerr, "On Namias's fractional Fourier transforms," *IMA J. Appl. Math.*, vol. 39, no. 2, pp. 159–175, 1987.

[145] I. McNulty, J. Kirz, C. Jacobsen, E. H. Anderson, M. R. Howells, and D. P. Kern, "High-resolution imaging by Fourier-transform X-ray holography," *Science*, vol. 256, no. 5059, pp. 1009–1012, May 1992.

[146] D. Mendlovic, Z. Zalevsky, D. Mas, J. Garcia, and C. Ferreira, "Fractional wavelet transform," *Appl. Opt.*, vol. 36, no. 20, pp. 4801–4806, July 1997.

[147] L. Mertz, "Real-time fringe-pattern analysis," *Appl. Opt.*, vol. 22, no. 10, pp. 1535–1539, May 1983.

[148] Ch. F. Meyer, *The diffraction of light, X-rays and material particles.* Chicago, IL, USA: University of Chicago Press, 1934.

[149] R. R. Meyer and E. Heindl, "Reconstruction of off-axis electron holograms using a neural net," *J. Microsc.-Oxf.*, vol. 191, pp. 52–59, July 1998.

[150] Y. Meyer, *Les ondelettes. Algorithmes et applications.* Paris: Armand Colin, 1992.

[151] P. A. Midgley, "An introduction to off-axis electron holography," *Micron*, vol. 32, no. 2, pp. 167–184, 2001.

[152] J. H. Milgram, "Computational holographic image reconstruction," in *Practical Holography XVI And Holographic Materials VIII*, vol. 4659. Proc. SPIE, 2002, pp. 12–29.

[153] A. J. Moore and F. Mendoza-Santoyo, "Phase demodulation in the space domain without a fringe carrier," *Opt. Lasers Eng.*, vol. 23, no. 5, pp. 319–330, Sept. 1995.

[154] P. Morin, "Computer simulation and object reconstruction in low-energy off-axis electron holography," *Ultramicroscopy*, vol. 76, no. 1-2, pp. 1–12, Feb. 1999.

[155] R. A. Muller and A. Buffington, "Real-time correction of atmospherically degraded telescope images through image sharpening," *J. Opt. Soc. Amer.*, vol. 64, no. 9, pp. 1200–1210, Sept. 1974.

[156] S. Murata and N. Yasuda, "Potential of digital holography in particle measurement," *Opt. Laser Technol.*, vol. 32, no. 7–8, pp. 567–574, 2000.

[157] V. Namias, "The fractional order Fourier transform and its application to quantum mechanics," *J. Inst. Math. Appl.*, vol. 25, no. 3, pp. 241–265, 1980.

[158] K. A. Nugent, "Interferogram analysis using an accurate fully automatic algorithm," *Appl. Opt.*, vol. 24, no. 18, pp. 3101–3105, Sept. 1985.

[159] B. A. Olshausen and D. J. Field, "Emergence of simple-cell receptive field properties by learning a sparse code for natural images," *Nature*, vol. 381, pp. 607–609, 1996.

[160] L. Onural, "Diffraction from a wavelet point of view," *Opt. Lett.*, vol. 18, no. 11, pp. 846–848, June 1993.

[161] ——, "Sampling of the diffraction field," *Appl. Opt.*, vol. 39, no. 32, pp. 5929–5935, Nov. 2000.

[162] L. Onural and M. Kocatepe, "Family of scaling chirp functions, diffraction, and holography," *IEEE Trans. Signal Process.*, vol. 43, pp. 1568–1578, 1995.

[163] L. Onural and M. T. Özgen, "Extraction of 3-D object-location information directly from in-line holograms using Wigner analysis," *J. Opt. Soc. Am. A*, vol. 9, no. 2, pp. 252–260, 1992.

[164] *Oxford English Dictionary.* Oxford University Press, Accessed online, Feb. 2004 at http://dictionary.oed.com/entrance.dtl.

[165] H. M. Ozaktas, Z. Zalevsky, and M. A. Kutay, *The Fractional Fourier Transform with Applications in Optics and Signal Processing*, ser. Series in Pure and Applied Optics. Wiley, 2001, vol. xviii.

[166] G. Paez and M. Strojnik, "Phase reconstruction from undersampled intensity patterns," *J. Opt. Soc. Am. A*, vol. 17, no. 1, pp. 46–52, Jan. 2000.

0010001000

[167] G. Pan and H. Meng, "Digital holography of particle fields: reconstruction by use of complex amplitude," *Appl. Opt.*, vol. 42, no. 5, pp. 827–833, Feb. 2003.

[168] G. Pedrini, S. Schedin, and H. J. Tiziani, "Aberration compensation in digital holographic reconstruction of microscopic objects," *J. Mod. Opt.*, vol. 48, no. 6, pp. 1035–1041, 2001.

[169] P. Pellat-Finet, "Fresnel diffraction and the fractional-order Fourier transform," *Opt. Lett.*, vol. 19, no. 18, pp. 1388–1390, Sept. 1994.

[170] P. Picart, E. Moisson, and D. Mounier, "Twin-sensitivity measurement by spatial multiplexing of digitally recorded holograms," *Appl. Opt.*, vol. 42, no. 11, pp. 1947–1957, Apr. 2003.

[171] M. Pirga and M. Kujawińska, "Two directional spatial-carrier phase-shifting method for analysis of crossed closed fringe patterns," *Opt. Eng.*, vol. 34, no. 8, pp. 2459–2466, Aug. 1995.

[172] H. Poincaré, *Leçons sur la Théorie mathématique de la lumière*. Paris: George Carré, 1889.

[173] R. M. Potvliege, "Waveletlike basis function approach to the propagation of paraxial beams," *J. Opt. Soc. Am. A*, vol. 17, no. 6, pp. 1043–1047, June 2000.

[174] W. H. Press, S. A. Teukolsky, W. T. Vetterling, and B. P. Flannery, *Numerical Recipes in C*, 2nd ed. Cambridge, U.K.: Cambridge Univ. Press, 1992.

[175] P. L. Ransom and J. Kokal, "Interferogram analysis by a modified sinusoid fitting technique," *Appl. Opt.*, vol. 25, no. 22, pp. 4199–4204, Nov. 1986.

[176] C. Rathjen, "Statistical properties of phase-shift algorithms," *J. Opt. Soc. Am. A*, vol. 12, no. 9, pp. 1997–2008, Sept. 1995.

[177] J. W. S. Rayleigh, *The theory of sound*, second (1896) ed. New York: Dover Publications, 1945, vol. II.

[178] R.-J. Recknagel and G. Notni, "Analysis of white light interferograms using wavelet methods," *Opt. Commun.*, vol. 148, pp. 122–128, 1998.

[179] I. Richards and Youn H., *Theory of Distributions: a non-technical introduction*. Cambridge, Mass.: Cambridge University Press, 1990.

[180] C. Roddier and F. Roddier, "Interferogram analysis using Fourier transform techniques," *Appl. Opt.*, vol. 26, no. 9, pp. 1668–1673, May 1987.

[181] F. Rooms, A. Pizurica, and W. Philips, "Estimating image blur in the wavelet domain," in *Proceedings of the Fifth Asian Conference on Computer Vision (ACCV)*, 2002, pp. 210–215.

[182] A. I. Sabra, *Theories of light, from Descartes to Newton*. Cambridge, Mass.: Cambridge University Press, 1981.

[183] P. Sandoz, "Wavelet transform as a processing tool in white-light interferometry," *Opt. Lett.*, vol. 22, no. 14, pp. 1065–1067, July 1997.

[184] J. Schmit and K. Creath, "Window function influence on phase error in phase-shifting algorithms," *Appl. Opt.*, vol. 35, no. 28, pp. 5642–5649, Oct. 1996.

[185] U. Schnars and W. Jüptner, "Direct recording of holograms by a CCD target and numerical reconstruction," *Appl. Opt.*, vol. 33, no. 2, pp. 179–181, Jan. 1994.

0010001001

[186] R. Sedgewick, *Algorithms,* 2nd ed.   Reading, Mass.: Addison-Wesley, 1988.

[187] M. Servin and F. J. Cuevas, "A novel technique for spatial phase-shifting interferometry," *J. Mod. Opt.*, vol. 42, no. 9, pp. 1853–1862, Sept. 1995.

[188] M. Servin, J. L. Marroquin, and F. J. Cuevas, "Demodulation of a single interferogram by use of a two-dimensional regularized phase-tracking technique," *Appl. Opt.*, vol. 36, no. 19, pp. 4540–4548, July 1997.

[189] P. B. Shelley, *Queen Mab: A Philosophical Poem. With Notes.*   Published by the author, 1813, available online http://www.bartleby.com/139/shel111.html.

[190] Y. L. Sheng, S. Deschênes, and H. J. Caulfield, "Monochromatic electromagnetic wavelets and the Huygens principle," *Appl. Opt.*, vol. 37, pp. 828–833, 1998.

[191] Y. L. Sheng, D. Roberge, and H. H. Szu, "Optical wavelet transform," *Opt. Eng.*, vol. 31, no. 9, pp. 1840–1845, Sept. 1992.

[192] L. Sica, "Image-sharpness criterion for space-variant imaging," *J. Opt. Soc. Amer.*, vol. 71, pp. 1172–1175, 1981.

[193] *Signal Processing Toolbox User's Guide for use with Matlab*, The Math-Works, Inc., Natick, Mass., USA, 2002.

[194] A. Sommerfeld, "Mathematische Theorie der Diffraction." *Math. Ann. 47*, pp. 317–374, 1896.

[195] ——, *Optics*, ser. Lectures on theoretical physics.   New York: Academic Press, 1967, vol. IV, fourth printing.

[196] S. Sotthivirat and J. A. Fessler, "Relaxed ordered subsets algorithm for image restoration of confocal microscopy," in *Proceedings of the First 2002 IEEE International Symposium on Biomedical Imaging: Macro to Nano (ISBI'02)*, vol. 3, Washington DC, USA, July 7–10, 2002, pp. 1051–1054.

[197] ——, "Penalized-likelihood image reconstruction for digital holography," *J. Opt. Soc. Am. A*, pp. —to be published, 2004.

[198] A. Stadelmaier and J. H. Massig, "Compensation of lens aberrations in digital holography," *Opt. Lett.*, vol. 25, no. 22, pp. 1630–1632, Nov. 2000.

[199] G. Strang and T. Q. Nguyen, *Wavelets and Filter Banks.*   Cambridge Mass.: Wellesley-Cambridge Press, 1996.

[200] J. W. Strutt, "On the maintenance of vibrations by forces of double frequency, and on the propagation of waves through a medium endowed with a periodic structure," *Philosophical Magazine*, vol. 24, pp. 145–159, 1887, Reprinted in [177, pp. 395].

[201] Y. Surrel, "Design of algorithms for phase measurements by the use of phase stepping," *Appl. Opt*, vol. 35, no. 1, pp. 51–60, Jan. 1996.

[202] M. Takeda, H. Ina, and S. Kobayashi, "Fourier-transform method of fringe-pattern analysis for computer-based topography and interferometry," *J. Opt. Soc. Amer.*, vol. 72, no. 1, pp. 156–160, Jan. 1982.

[203] Ph. Thévenaz and M. Unser, "Optimization of mutual information for multiresolution image registration," *IEEE Trans. Image Process.*, vol. 9, no. 12, pp. 2083–2099, Dec. 2000.

0010001010

[204] P. Tomassini, A. Giulietti, L. A. Gizzi, M. Galimberti, D. Giulietti, M. Borghesi, and O. Willi, "Analyzing laser plasma interferograms with a continuous wavelet transform ridge extraction technique: the method," *Appl. Opt.*, vol. 40, no. 35, pp. 6561–6568, Dec. 2001.

[205] A. Tonomura, *Electron holography*, ser. Springer series in optical sciences.   Berlin, Germany: Springer, 1999, vol. 70.

[206] M. Unser, "Sampling—50 Years after Shannon," *Proc. IEEE*, vol. 88, no. 4, pp. 569–587, Apr. 2000.

[207] M. Unser, A. Aldroubi, and M. Eden, "On the asymptotic convergence of B-spline wavelets to Gabor functions," *IEEE Trans. Inf. Theory*, vol. 38, no. 2, pp. 864–872, 1992.

[208] ——, "A family of polynomial spline wavelet transforms," *Signal Processing*, vol. 30, no. 2, pp. 141–162, Jan. 1993.

[209] ——, "The L_2-polynomial spline pyramid," *IEEE Trans. Pattern Anal. Mach. Intell.*, vol. 15, no. 4, pp. 364–379, Apr. 1993.

[210] M. Unser, A. Aldroubi, and S. J. Schiff, "Fast implementation of the continuous wavelet transform with integer scales," *IEEE Trans. Signal Process.*, vol. 42, no. 12, pp. 3519–3523, Dec. 1994.

[211] M. Unser and Th. Blu, "Fractional splines and wavelets," *SIAM Review*, vol. 42, no. 1, Mar. 2000.

[212] ——, "Wavelet theory demystified," *IEEE Trans. Signal Process.*, vol. 51, no. 2, pp. 470–483, Feb. 2003.

[213] Michael Unser, "Splines: a perfect fit for signal processing and image processing," *IEEE Signal Process. Magazine*, vol. 16, no. 6, pp. 22–38, Nov. 1999.

[214] K. Urata, K. Ishizuka, T. Tanji, and A. Tonomura, "An application of digital filtering in electron holography at atomic-resolution," *J. Electron Microsc.*, vol. 42, no. 2, pp. 88–93, Apr. 1993.

[215] É. Verdet, *Leçons d'optique physique*.   Paris: Imprimerie Impériale, 1869.

[216] V. I. Vlad and D. Malacara, "Direct spatial reconstruction of optical phase from phase modulated images," in *Progress in Optics, Vol. XXXIII*, E. Wolf, Ed.   Amsterdam: Elsevier, 1994, pp. 261–317.

[217] E. Völkl, L. F. Allard, A. Datye, and B. Frost, "Advanced electron holography—a new algorithm for image processing and a standardized quality test for the FEG electron-microscope," *Ultramicroscopy*, vol. 58, no. 1, Apr. 1995.

[218] E. Völkl, L. F. Allard, and B. Frost, "A software package for the processing and reconstruction of electron holograms," *J. Microsc.-Oxf.*, vol. 180, pp. 39–50, Oct. 1995.

[219] E. Wallon, *Leçons d'optique à l'usage des élèves de mathématiques spéciales*.   Paris: Gauthier-Villars, 1900.

[220] L. R. Watkins, S. M. Tan, and T. H. Barnes, "Determination of interferometer phase distributions by use of wavelets," *Opt. Lett.*, vol. 24, no. 13, pp. 905–907, July 1999.

[221] J. B. Weaver, X. Yansun, D. M. Healy, Jr., and L. D. Cromwell, "Filtering noise from images with wavelet transforms," *Magnetic Resonance in Medicine*, vol. 21, no. 2, pp. 288–295, Oct. 1991.

0010001011

[222] J. Widjaja and S. Jutamulia, "Use of wavelet analysis for improving autofocusing capability," *Opt. Commun.*, vol. 151, no. 1–3, pp. 12–14, May 1998.

[223] R. Windecker and Tiziani H. J., "Semispatial, robust, and accurate phase evaluation algorithm," *Appl. Opt.*, vol. 34, no. 31, pp. 7321–7326, Nov. 1995.

[224] K. H. Womack, "Interferometric phase measurement using spatial synchronous detection," *Opt. Eng.*, vol. 23, no. 4, pp. 391–395, July-August 1984.

[225] L. P. Yaroslavskii and N. S. Merzlyakov, *Methods of Digital Holography*. New York: Consultants Bureau, 1980.

[226] L. Yaroslavsky, *Digital Holography and Digital Image Processing: Principles, Methods, Algorithm*. Kluwer, 2003.

[227] L. Yaroslavsky and N. Ben-David, "Focal plane invariant algorithm for digital reconstruction of holograms recorded in the near diffraction zone," in *Optical Measurement Systems For Industrial Inspection III*, W. Osten, K. Creath, and M. Kujawinska, Eds., vol. 5144, Munich, Germany, June 22–25, 2003, pp. 142–149.

[228] R. Yin, P. J. Flynn, and S. L. Broschat, "Position-dependent defocus processing for acoustic holography images," *Int. J. Imag. Syst. Tech.*, vol. 12, no. 3, pp. 101–111, 2002.

[229] E. Yu and S. S. Cha, "Two-dimensional regression for interferometric phase extraction," *Appl. Opt.*, vol. 37, no. 8, pp. 1370–1376, Mar. 1998.

[230] P. Zhang, "Inherent relation between the real part and the imaginary part of a complex holographic function in acoustic holographic imaging—digital reconstruction method without conjugate image by using only the real part (or imaginary part) of a complex holographic function," *J. Acoust. Soc. Amer.*, vol. 72, no. 5, pp. 1492–1497, 1982.

[231] M. Zibulevsky and Y. Y. Zeevi, "Extraction of a source from multichannel data using sparse decomposition," *Neurocomputing*, vol. 49, pp. 163–173, 2002.

0010001100

Appendix A

Fourier Transform Properties

Definitions
Fourier transform:

$$\hat{f}(\nu) = \int_{-\infty}^{+\infty} f(t)\exp(-2\pi i t\nu)\mathrm{d}t, \quad f \in L_1(\mathbb{R}) \tag{A.1}$$

Inverse Fourier Transform:

$$f(t) = \int_{-\infty}^{+\infty} \hat{f}(\nu)\exp(2\pi i t\nu)\mathrm{d}\nu \quad \text{a. e.} \tag{A.2}$$

Properties
In the sense of distributions [179], we have:

$$\forall \phi \in S, \quad \langle \hat{f}, \phi \rangle = \langle f, \hat{\phi} \rangle. \tag{A.3}$$

Parseval and Plancherel Formulas:

$$\langle f, g \rangle = \langle \hat{f}, \hat{g} \rangle \tag{A.4}$$

$$\|f\|^2 = \|\hat{f}\|^2. \tag{A.5}$$

Heisenberg uncertainty relation Let $f \in L_2(\mathbb{R})$. We have following inequality:

$$\sigma_f^2 \sigma_{\hat{f}}^2 \geq \frac{1}{16\pi^2}. \tag{A.6}$$

This inequality is an equality if and only if there exist t_0, ω_0, b real and a complex amplitude a such that:

$$f(t) = a\,\mathrm{e}^{i\omega_0 t}\,\mathrm{e}^{-b(t-t_0)^2}. \tag{A.7}$$

Other properties are summarized in Table A.I. In Table A.II we have gathered some useful Fourier transform pairs.

Property	Function	Fourier Transform	
	$f(t)$	$\hat{f}(v)$	
Inverse	$\hat{f}(t)$	$f(-v)$	(A.8)
Convolution	$f_1 * f_2(t)$	$\hat{f}_1(v)\hat{f}_2(v)$	(A.9)
Multiplication	$f_1(t)f_2(t)$	$\hat{f}_1 * \hat{f}_2(v)$	(A.10)
Translation	$f(t-t_0)$	$\exp(-2i\pi t_0 v)\hat{f}(v)$	(A.11)
Modulation	$\exp(2i\pi v_0 t)f(t)$	$\hat{f}(v-v_0)$	(A.12)
Scaling	$f\left(\dfrac{t}{s}\right)$	$\|s\|\hat{f}(sv)$	(A.13)
Time derivatives	$f^{(p)}(t)$	$(2i\pi v)^p \hat{f}(v)$	(A.14)
Frequency derivatives	$(-2i\pi t)^p f(t)$	$\hat{f}^{(p)}(v)$	(A.15)
Complex conjugate	$f^*(t)$	$\hat{f}^*(-v)$	(A.16)
Hermitian symmetry	$f(t) \in \mathbb{R}$	$\hat{f}(-v) = \hat{f}^*(v)$	(A.17)

TABLE A.I

FOURIER TRANSFORM PROPERTIES

Function	Fourier transform	
$\delta(x)$	1	(A.18)
$\delta(x-a)$	$\exp(-2\pi i a v)$	(A.19)
$\exp(2\pi i a x)$	$\delta(v-a)$	(A.20)
$\mathrm{rect}(x) = \begin{cases} 1 & \text{if } \|x\| < 1/2, \\ 1/2 & \text{if } \|x\| = 1/2, \\ 0 & \text{if } \|x\| > 1/2 \end{cases}$	$\mathrm{sinc}(v) = \dfrac{\sin(\pi v)}{\pi v}$	(A.21)
$\mathrm{sinc}(x) = \dfrac{\sin(\pi x)}{\pi x}$	$\mathrm{rect}(v)$	(A.22)
$\sum_k \delta(x-k)$	$\sum_k \delta(v-k)$	(A.23)

TABLE A.II

FOURIER TRANSFORM PAIRS

0010001110

Poisson Summation Formula

Eq. (A.3) and Eq. (A.23) imply the Poisson summation formula:

$$\sum_n f(n) = \sum_n \hat{f}(n). \tag{A.24}$$

A direct consequence is that

$$\sum_{n=-\infty}^{\infty} \delta(x-n) = \sum_{n=-\infty}^{\infty} \exp(-2\pi i n x). \tag{A.25}$$

If we convolve both sides with $\hat{f}(x)$, we obtain:

$$\sum_{n=-\infty}^{\infty} f(n) \exp(-2\pi i n v) = \sum_{n=-\infty}^{\infty} \hat{f}(v-n). \tag{A.26}$$

An usefull Dirac delta property is:

$$\delta(sx) = (1/s)\delta(x). \tag{A.27}$$

Compatible Software-Conventions

MATHEMATICA:

```
fhat[v_]=FourierTransform[f[t],t,v,
                FourierParameters → {0, -2 π}]
f[t_]=InverseFourierTransform[fhat[v],v,t,
                FourierParameters → {0,-2 π}]
```

MATLAB Fast Fourier Transform [33]:

```
fhat=fft(f);
f=ifft(fhat);
```

where f and fhat are vectors of length N (indexed from 1 to N) constructed as follows:

$$\text{fhat}(n) = \sum_{k=0}^{N-1} \text{f}(k) \exp(-2i\pi(n-1)k/N) \tag{A.28}$$

$$\text{f}(n) = \frac{1}{N} \sum_{k=0}^{N-1} \text{fhat}(k) \exp(2i\pi(n-1)k/N). \tag{A.29}$$

Appendix B

Fresnel Transform Properties

Important properties of the Fresnel transform are summarized in Table B.I.

Property	Function	Transformed Function	
	$f(x)$	$\widetilde{f}_\tau(x)$	
Duality	$(\tilde{f}_\tau)^*(x)$	$f^*(x)$	(B.1)
Additivity	$\widetilde{f}_\sigma(x)$	$\widetilde{f}_{(\sigma^2+\tau^2)^{1/2}}(x)$	(B.2)
Translation	$f(x-x_0)$	$\widetilde{f}_\tau(x-x_0)$	(B.3)
Scaling	$f\left(\dfrac{x}{s}\right)$	$\widetilde{f}_{\tau/s}\left(\dfrac{x}{s}\right)$	(B.4)
Modulation	$e^{i2\pi v_0 x} f(x)$	$e^{i2\pi v_0 x}\, e^{-i\pi v_0^2 \tau^2}\, \widetilde{f}_\tau(x-v_0\tau^2)$	(B.5)
Differentiation (1)	$f'(x)$	$(\widetilde{f}_\tau)'(x)$	(B.6)
Differentiation (2)	$f'(x)$	$\dfrac{2i\pi}{\tau^2}\left(x\widetilde{f}_\tau(x)-(xf)\widetilde{}_\tau(x)\right)$	(B.7)
Convolution	$(f*g)(x)$	$e^{-i\pi/4}(\widetilde{f}_{\tau_1} * \widetilde{g}_{\tau_2})(x),\ \tau_1^2+\tau_2^2=\tau^2$	(B.8)
Chirp	$\dfrac{1}{\rho}\, e^{i\pi(x/\rho)^2} f(x)$	$\dfrac{1}{\sqrt{\rho^2+\tau^2}}\, e^{i\pi\frac{x^2}{\rho^2+\tau^2}}\, \widetilde{f}_{\frac{\tau\rho}{\sqrt{\rho^2+\tau^2}}}\left(\dfrac{\rho^2}{\rho^2+\tau^2}\,x\right)$	(B.9)
General	$\dfrac{1}{\rho_1}\, e^{i\pi(x/\rho_1)^2}\, \widetilde{f}_{\tau_1}\left(\dfrac{x}{s_1}\right)$	$\dfrac{1}{\rho_2}\, e^{i\pi(x/\rho_2)^2}\, \widetilde{f}_{\tau_2}\left(\dfrac{x}{s_2}\right)$	
		$\rho_2^2=\tau^2+\rho_1^2$	
		$s_2=s_1\rho_2^2/\rho_1^2$	
		$\tau_2^2=\left(\dfrac{\tau\rho_1}{s_1\rho_2}\right)^2+\tau_1^2$	(B.10)

<div align="center">

TABLE B.I

FRESNEL TRANSFORM PROPERTIES.

</div>

0010010001

Appendix C

Michael Liebling (-Glardon)

Biomedical Imaging Group
EPFL-LIB, Bât. BM 4.141
CH-1015 Lausanne, Switzerland
Tel.: +41 21 693 51 43
michael.liebling@a3.epfl.ch
http://bigwww.epfl.ch/liebling/

Age: 27
Swiss
Married

Objectives

Develop algorithms and mathematical tools for the advanced processing of biomedical images and for solving inverse problems raised by novel imaging modalities. Work on application-oriented projects in tight collaboration with researchers in medicine or biology as well as engineers.

Education

2000–2004 PhD in Image Processing and Digital Holography
Biomedical Imaging Group, Swiss Federal Institute of Technology Lausanne (EPFL)
PhD dissertation: "On Fresnelets, Interference Fringes, and Digital Holography"
Thesis advisor: Prof. M. Unser
Research interests: inverse problems, optics, image processing and wavelets

1995–2000 MSc in Physics
Swiss Federal Institute of Technology Lausanne (EPFL)
Diploma thesis at the Biomedical Imaging Group: "Image reconstruction from projections by filtered backprojection"
Other projects completed: Development of an automated light polarization imaging method at the Applied Optics Institute (IOA), Compression of dermatoscopic images using wavelets, Signal Processing Laboratory (LTS)

1992–1995 Baccalauréat ès sciences, maturité type C (awarded the class prize)
Gymnase cantonal du Bugnon, Lausanne

Experience

Research assistant at the Biomedical Imaging Group, EPFL
Teaching assistant for image processing (including Java labs), applied optics and classical mechanics courses
Supervision of several student semester and diploma projects in image processing
Moderator of the EPFL wavelet interest group (organized 7 seminars in 2003)
Reviewer for IEEE Trans. on Medical Imaging, IEEE Trans. on Image Processing, IEEE Signal Processing Letters
Expert for Signal and Systems, and Optics exams

Languages

Bilingual French-German, fluent in English

Computer skills

Operating systems: Mac OS, Linux, Windows
Programming: Matlab, IDL, C, Java, Labview, Fortran90
Publishing: TEX, HTML, Photoshop, Illustrator, Acrobat, Office

Professional societies

Member of IEEE, OSA, and SPIE

Extra-curricular

Violin: member of the Orchestre Symphonique et Universitaire de Lausanne
Billiards: treasurer of the Académie Lausannoise de Billard 2001–2003
Windsurfing: J+S instructor, course organizer for over 60 participants 1994–1999
Sailing, skiing, snowboarding

Publications

Journal Papers

[1] M. Liebling, Th. Blu, and M. Unser, "Complex-wave retrieval from a single off-axis hologram," *J. Opt. Soc. Am. A*, vol. 21, no. 3, pp. 367–377, Mar. 2004.

[2] ——, "Fresnelets: new multiresolution wavelet bases for digital holography," *IEEE Trans. Image Process.*, vol. 12, no. 1, pp. 29–43, Jan. 2003.

[3] S. Horbelt, M. Liebling, and M. Unser, "Discretization of the Radon transform and of its inverse by spline convolutions," *IEEE Trans. Med. Imag.*, vol. 21, no. 4, pp. 363–376, Apr. 2002.

Submitted Paper

[1] M. Liebling and M. Unser, "Autofocus for digital Fresnel holograms by use of a Fresnelet-sparsity criterion," *submitted to J. Opt. Soc. Am. A*, 2004.

Conference Papers

[1] M. Liebling, Th. Blu, and M. Unser, "Non-linear Fresnelet approximation for interference term suppression in digital holography," in *Wavelets: Applications in Signal and Image Processing X*, M. A. Unser, A. Aldroubi, and A. F. Laine, Eds., vol. 5207. San Diego CA, USA: Proc. SPIE, August 3–8, 2003, pp. 553–559.

[2] M. Liebling, Th. Blu, E. Cuche, P. Marquet, Ch. Depeursinge, and M. Unser, "Local amplitude and phase retrieval method for digital holography applied to microscopy," in *Novel Optical Instrumentation for Biomedical Applications (ECBO'03)*, A.-C. Boccara, Ed., vol. 5143. Munich, Germany: Proc. SPIE, June 22–25, 2003, pp. 210–214.

[3] ——, "A novel non-diffractive reconstruction method for digital holographic microscopy," in *Proceedings of the First 2002 IEEE International Symposium on Biomedical Imaging: Macro to Nano (ISBI'02)*, Washington DC, USA, July 7–10, 2002, pp. 625–628.

[4] S. Horbelt, M. Liebling, and M. Unser, "Filter design for filtered back-projection guided by the interpolation model," in *International Symposium on Medical Imaging: Image Processing (MI'02)*, M. Sonka and J.M. Fitzpatrick, Eds., vol. 4684. San Diego CA, USA: Proc. SPIE, February 24–28, 2002, pp. 806–813.

[5] M. Liebling, Th. Blu, and M. Unser, "Fresnelets—A new wavelet basis for digital holography," in *Wavelet: Applications in Signal and Image Processing IX*, A.F. Laine, M.A. Unser, and A. Aldroubi, Eds., vol. 4478. San Diego CA, USA: Proc. SPIE, July 29–Aug. 1 2001, pp. 347–352.

Conference Abstracts

[1] Ch. Depeursinge, E. Cuche, T. Colomb, P. Massatch, A. Marian, F. Montfort, M. Liebling, Th. Blu, M. Unser, P. Marquet, and P.J. Magistretti, "Digital holography applied to microscopy: A new imaging modality in the sub-wavelength range," in *Hundertvierte Jahrestagung der Deutschen Gesellschaft für angewandte Optik (DGaO)*, Münster (Westfalen), Germany, June 10-14, 2003.

[2] M. Liebling, "Algorithmic aspects of tomographic reconstruction from parallel and diffracted projections," in *Second Korean-Swiss Workshop on Novel Coherence-Based Radiology Techniques*, Jeju-Do, Korea, February 19–22, 2003, invited talk.